Investigating the Impacts of Processing Uncertainty and Variability on Residual Stresses and Deformations in Aerospace Composites Manufacturing

Caleb Schoenholz

A dissertation

submitted in partial fulfillment of the

requirements for the degree of

Doctor of Philosophy

University of Washington

2024

Reading Committee:

Navid Zobeiry, Chair

Dwayne Arola

Eleftheria Roumeli

Program Authorized to Offer Degree:

Materials Science and Engineering

University of Washington

Abstract

Investigating the Impacts of Processing Uncertainty and Variability on Residual Stresses and Deformations in Aerospace Composites Manufacturing

Caleb Schoenholz

Chair of the Supervisory Committee:
Navid Zobeiry
Materials Science and Engineering Department

Despite significant advancements in materials formulation and manufacturing technologies, high levels of uncertainty persist in the raw material and production of composite-intensive aircraft. One such uncertainty source is the impact of material and processing variabilities on residual stresses and deformations in composite parts, which negatively affects the assembly process of aerostructures. This research investigates these phenomena, focusing on Toray T800S/3900-2B, an aerospace-grade material used in the production of several aircraft such as the Boeing 787. The initial research phase involves a comprehensive characterization of various material properties, manufacturing phenomena, and processing variables that may significantly impact process-induced deformations (PIDs) but are surrounded by high uncertainty. Investigations include assessing the impact of release coating on tool surface properties, examining

the influence of processing conditions on T800S/3900-2B, and evaluating the role of processing variabilities in tool-part interactions. Next, a novel machine learning (ML) method is developed for accelerated composites characterization, which demonstrates substantial time and cost savings compared to traditional methods. A parametric exploration into the effects of layup and cure cycle procedures on PIDs is conducted, and potential mitigation strategies are proposed. Next, an innovative methodology for efficiently predicting PIDs and analyzing composites using multi-fidelity simulation and theory-guided machine learning (TGML) is devised. Lastly, a novel process optimization approach for minimizing PIDs in composite parts without the use of any material characterization or process simulation is introduced. This research aims to provide a comprehensive framework for further exploration and potential mitigation of PIDs in aerospace composites manufacturing.

TABLE OF CONTENTS

LIST OF FIGURES

LIST OF TABLES

ACKNOWLEDGEMENTS

This research was conducted in the Materials Science & Engineering Department at the University of Washington and received funding support from Toray Composite Materials America, Inc. Many individuals played major roles in the success of this work, and I would like to extend my gratitude to the following people:

To Dr. Navid Zobeiry, thank you for your continuous support and guidance over the last four years. It has been a true privilege to be a part of the UW Composites Group. The technical knowledge and leadership skills I have learned from you will undoubtedly be invaluable to me throughout my career and life.

To Dr. Dwayne Arola, Dr. Eleftheria Roumeli, and Dr. Mohammed Malakooti, thank you for your valuable contributions as members of my supervisory committee. I feel incredibly fortunate to have received support from people as exceptional and genuine as yourselves.

To Dr. Ichiro Taketa, Dr. Toshiya Kamae, Dr. Don Lee, Dr. Ben Rutz, and the rest of the Toray team, thank you for providing funding and sharing your technical expertise throughout this work. Your support has given me a tremendous opportunity to learn and grow as a scientist and engineer.

To my University of Washington friends, thank you for the collaborations, laughs, and happy hours. Thank you especially to Mat Wynn, Paulina Picazo, Max Fu, Amirali Eskandariyun, Allyson Fontes, Alex Gray, and Derrick Ong for making the long days in the lab truly enjoyable.

To Dr. Marco Petrolo, Dr. Enrico Zappino, Dr. Matteo Filippi, Dr. Alfonso Pagani, Dr. Erasmo Carrera, Rebecca Masia, and all other members of the MUL2 Group, thank you for your hospitality and for the opportunity to work alongside you at Politecnico di Torino over the summer. Collaborating with you all was a once-in-a-lifetime experience that I will forever be grateful for.

To my family, thank you for always being there. Your support means very much to me.

To Rylee, thank you for your friendship and love. You have made my life better in every way.

DEDICATION

This work is dedicated to my dad,
who has been the greatest inspiration in my life.

1. INTRODUCTION

1.1 AEROSPACE COMPOSITES MANUFACTURING

For decades, carbon fiber-reinforced polymer (CFRP) composites have been extensively utilized in the construction of commercial and military aircraft. Composites possess exceptionally high specific strength and stiffness properties, making them attractive candidates for replacing legacy metals and reducing operational weights. Additionally, the ability of composites to be manufactured to net-shape potentially offers significant gains in assembly time by consolidating the number of parts and reducing the need for factory work, such as bolted bonding. The development of interlayer-toughened composite materials such as Toray's T800S/3900-2B system has allowed manufacturers to integrate composites into primary aerostructures to reduce weights further, enable longer flight ranges, improve lifecycle costs, and lower carbon emissions.[1]

Several techniques may be used for processing thermoset composite parts, all of which consist of four essential steps: combine the matrix and fibers, lay them onto a tool (i.e., mold), apply compaction pressure, and cure the polymer matrix typically at elevated temperatures. Large and complex-shaped aerospace components are typically processed using the autoclave method at temperatures and pressures of approximately 180 °C and 0.7 MPa (~7 atm), respectively, to reduce processing defects such as porosity within an acceptable threshold.[2] For most autoclave processing, unidirectional (UD) sheets of fibers that have been "pre-impregnated" with a partially cured polymer matrix (i.e., B-stage prepregs) are first shaped and stacked onto a tool. UD prepregs have highly anisotropic properties, allowing manufacturers to optimize load paths and reduce weight by stacking plies in tailored orientations and orders.

After the prepreg plies are stacked onto a tool, the layup is vacuum bagged, loaded into an autoclave, and cured using a high-temperature/pressure cycle. At high temperatures, curing

kinetics accelerate and a cross-linking reaction propagates to the material's boundaries, leading to gelation, and eventually vitrification phase transformations.[3] External pressures are applied for compaction purposes and to remove voids before gelation, which may otherwise negatively affect the end-part quality. After curing, the composite part is removed from the autoclave, demolded from the tool, and transferred to machining, finishing, and assembly steps.

1.2 PROCESS-INDUCED RESIDUAL STRESSES AND DEFORMATIONS

Although processing methods are generally well-established in the aerospace industry, several challenges remain throughout production. One major challenge is minimizing process-induced deformations (PIDs) in composite parts, without significantly affecting the final structure's performance and/or slowing down production rates. If PIDs exceed acceptable thresholds, costly and time-consuming shimming steps are required during the assembly process, resulting in slow production rates.[4]

During autoclave processing, residual stresses form due to many complex, interdependent, and multi-scale phenomena.[2,5] For example, at the micro-level, residual stresses are mainly caused by a mismatch of free strains between the fibers and matrix due to differences in thermal properties (i.e., coefficients of thermal expansion) and phase changes (i.e., cross-linking).[5] Macro-level stresses primarily arise from stress discontinuities and temperature/cure gradients between plies.[5] Residual stresses may also develop at the coupon- and component-levels due to factors such as ply drop-off, part geometry, and tool-part interaction.[5–7]

Following processing, residual stresses may be partially released from the part through bending and cause dimensional changes known as process-induced deformations (PIDs). Typically for complex-shaped parts found in composite aerostructures, such as L-shaped wing spars, two types of PIDs are observed, as illustrated in **Figure 1-1**: warpage of flat sections and spring-in,

involving the reduction or enlargement of angles at geometry transitions.[6–20] Warpage is primarily attributed to tool-part interaction effects, where elevated temperatures and pressures prompt the formation of interfacial physicochemical bonds and free strain mismatches between the tool and part due to thermal expansion differences and cure shrinkage in the composite. When combined with interfacial bonds, free strain mismatches create a shear interaction at the tool-part interface that transfers tensile stresses into the composite's tool-adjacent plies. Several processing variabilities, such as the age of release coating on the tool surface, layup techniques, and cure pressure, directly impact the efficiency of the tool-to-part residual stress transfer.[21] While some stresses are alleviated in plies furthest away from the tool surface through interlaminar shear, others remain unrelieved and become locked in as curing progresses, resulting in a through-thickness residual stress gradient in the composite part. During the demolding process following the cure cycle, the locked-in stress gradient is partially released through bending deformation and warpage.[6–9,11,13–16,22–25]

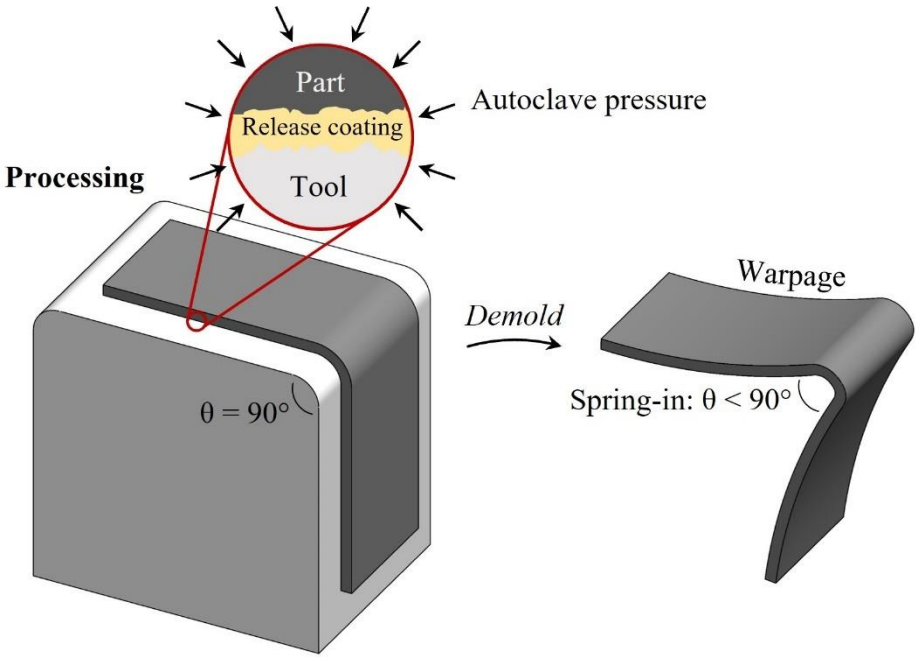

Figure 1-1. Schematic representation of autoclave processing and potential resulting PIDs in an L-shaped composite part.

Spring-in in composite parts is commonly linked with the orthotropic development of free strains, specifically through-thickness versus in-plane strains.[5,13,17–20,26–28] As an example, consider the processing of an L-shaped composite part on a tool, as schematically shown in **Figure 1-1**. Throughout the curing process, a significant through-thickness strain emerges in the composite due to a combination of cure shrinkage, thermal strains, and the Poisson effect. The Poisson effect arises because in-plane and fiber-direction strains remain negligible compared to the through-thickness changes. Additionally, in layups with minimal in-plane strain during processing due to constraints of zero-degree plies in both in-plane directions (e.g., quasi-isotropic, cross-ply), the Poisson effect also causes the transfer of in-plane strains to the through-thickness direction. This mismatch of in-plane and through-thickness free strains creates geometrical constraints on the outer layer of the L-shaped laminate as it cures. These constraints may be neutralized through shear deformation and the book-end effect when the composite's shear modulus (i.e., G_{13} and G_{23}) is minimal during early stages of the cure cycle. However, in later stages when the composite's modulus has significantly evolved, these geometrical restrictions may generate residual stresses in the composite material.[5]

During cooldown, additional strains are generated in the composite due to thermal shrinkage, while a secondary modulus evolution occurs from thermo-elastic effects. The significant mismatches of thermally-generated free strains between the fibers and matrix give rise to additional stresses in the part. Upon demolding, the locked-in residual stresses are partially released through bending deformation and spring-in at the L-shaped part's geometry transition point (i.e., corner).[5]

1.3 MITIGATING PROCESS-INDUCED DEFORMATIONS IN MANUFACTURING

While the fundamental mechanisms of residual stresses and PIDs are generally accepted, high uncertainty remains surrounding mitigation strategies. Consequently, aerospace manufacturers often rely on tacit-based approaches such as shimming to minimize the impacts of PIDs. The shimming technique involves using custom-made metal or composite inserts to fill gaps between structural components during assembly which arise from geometry mismatches.[4] Unfortunately, shimming is not only laborious and costly but also has the potential to introduce further stresses and compromise the mechanical performance of the final aerostructure.

A more fundamental approach to PID mitigation involves optimizing process parameters, such as tool geometry, layup techniques, or cure cycle, to minimize or compensate for residual stress developments.[29] At the laboratory scale, optimization efforts may be conducted using trial-and-error methods. However, as composite parts become larger, more complex, and expensive, relying on trial-and-error becomes inefficient, and other methods, such as process simulation, must be considered.

Given the multitude of complex contributing mechanisms, simulating PIDs requires extensive material characterization efforts.[30–33] For instance, a simplified workflow for a "traditional" simulation-based process optimization scheme may likely include the following steps. Initially, the cure kinetics and evolution of thermo-mechanical properties in the composite which contribute to residual stresses are experimentally characterized. As previously mentioned, the primary material-related parameters contributing to PIDs include the evolution of through-thickness and in-plane free strains, bending modulus, shear modulus, and tool-part interfacial adhesion/friction.[5] After sufficient characterization and validation of these properties, they are utilized as inputs to construct numerical models. Subsequently, many simulations may be

conducted to systematically explore design spaces, assess the interrelationships between process variabilities and material properties, and discover optimal parameters to minimize PIDs. Finally, additional experiments may be employed to calibrate the numerical models, fine-tune simulation predictions, and evaluate the overall effectiveness of the methodology.

While the previously described workflow is generally established and effective for many optimization problems, its application in minimizing PIDs for modern-era aerospace composites has encountered limited success due to several factors. As mentioned earlier, one key reason is the necessity for robust material characterization techniques, including methods to quantify all properties contributing to PIDs during composites processing cycles. Unfortunately, experimental methods for quantifying some of the necessary properties are currently absent in the literature. This shortcoming often leads to the simplification of material properties in process models, inaccurate predictions of PIDs, and ineffective optimization efforts. As the fidelities and complexities of material and process models increase (e.g., thermoviscoelastic versus pseudo-viscoelastic constitutive models), these problems are further amplified.[34]

Another factor contributing to the deficiencies of current simulation capabilities is that the vast majority of publicly available literature on PIDs is confined to the previous generation of structural material systems with accessible properties, such as Hexcel AS4/8552.[35] However, as previously mentioned, more complex materials containing interply toughers, such as the Toray T800S/3900-2B system, have become increasingly prevalent in the manufacturing of primary aerostructures.[1,36] Unfortunately, numerous properties of these interply-toughened materials have not been experimentally characterized. This lack of information further constrains process simulation capabilities and boosts uncertainty levels surrounding PIDs in aerospace composites manufacturing.

1.4 MOTIVATION, SCOPE, AND OVERVIEW OF WORK

Missing from existing literature and serving as the primary motivation of this work is an exploration of residual stresses and PIDs in the current generation of aerospace composites. As previously highlighted, much of the uncertainty surrounding PIDs stems from the high costs associated with characterization and the absence of experimental techniques capable of measuring potentially impactful properties. A lack of a reliable method to accurately quantify tool-part interaction during composites processing cycles is especially evident. Developing such a method is also vital for increasing the fidelity of numerical process simulation capabilities.

The demanding nature of experimental efforts required for "traditional" simulation-based strategies also serves as a secondary motivation of this research: to investigate alternative methods for more efficient material characterization and analysis of PIDs in composites. More broadly, there is a need for a cost-effective and widely applicable framework to understand and improve the design, development, and manufacturing of composite materials. Such a strategy would also hold significant promise for reducing labor costs currently required for problem-solving in many other fields of study.

Considering the aforementioned factors, this work aims to investigate the impacts of processing variabilities and act as a framework to potentially mitigate residual stresses and deformations in advanced aerospace composites. Specifically, this research focuses on a material currently utilized in the production of the Boeing 787, known as Toray T800S/3900-2B. To achieve this objective, several innovative methodologies are developed and compared throughout this work. One approach involves utilizing traditional deterministic strategies with robust experimental characterizations and numerical finite element (FE) simulations. Other investigative strategies presented utilize machine learning (ML) to explore the potential of probabilistic tools in

improving the efficiency of composites characterization and analysis. The fundamental understanding gained in this work will enable further innovation in the aerospace industry. Furthermore, the novel methods and results developed will contribute to the discovery of next-generation aerospace composite materials to address current demands, such as higher production rates, and facilitate the expansion of emerging markets, such as urban air mobility. The remainder of this thesis follows the subsequent workflow:

- In Chapter 2, a comprehensive characterization of several material properties and manufacturing phenomena surrounded by elevated levels of uncertainty is conducted. The chapter aims to attain a fundamental understanding of T800S/3900-2B and other potential PID sources, establishing a foundation for analyses in subsequent chapters.
- In Chapter 3, a novel method for accelerated material characterization is introduced. A generalizable strategy based on probabilistic machine learning (ML) is presented and applied to characterize thermo-mechanical properties of T800S/3900-2B. Throughout the chapter, the accuracy and speed of the ML method is compared with outcomes obtained from traditional methods.
- In Chapter 4, the impacts of layup and curing procedures on PIDs of L-shaped T800S/3900-2B parts are explored using an efficient finite element (FE) simulation code that references material property models developed earlier in this work. Throughout the investigation, optimal processing conditions and recommendations for better understanding PIDs in advanced composites are discussed.
- In Chapter 5, a novel approach for the accurate and efficient prediction of PIDs and analysis of composites is presented. The method combines theory-guided machine learning

(TGML) with data from multi-fidelity simulations and experiments to predict PIDs of L-shaped T800S/3900-2B parts using minimal experimental efforts.

- In Chapter 6, an innovative approach for discovering process parameters to minimize PIDs in composite parts is presented. The method aims to circumvent the need for material characterization and process simulation, providing a cost-efficient alternative to traditional strategies. The novel framework is applied to predict and validate optimal layups and cure cycles for minimizing deformations in L-shaped T800S/3900-2B parts.
- In Chapter 7, a comprehensive summary and conclusion of this research is provided. Novel findings and methods are revisited and recommendations for better understanding PIDs in aerospace composites parts are shared.

2. MATERIAL AND PROCESS CHARACTERIZATION

This chapter contains a characterization effort on various material properties and manufacturing phenomena that may significantly impact PIDs in aerospace composites. The chapter is divided into three subsections, each focusing on topics where literature is lacking, and uncertainty levels are high during manufacturing. The three primary points of emphasis include characterizing the physicochemical behavior of aerospace release coating, thermo-mechanical properties of T800S/3900-2B, and tool-part interaction. Each subsection commences with an overview of the phenomenon under investigation and its relevance to PIDs in composites. Subsequently, novel methods, findings, and discussions are shared.

2.1 B15/710-NC RELEASE COATING

2.1.1 Background

As discussed in the first chapter, one of the most significant factors contributing to PIDs in composites is free strain mismatches at different scales in the laminate and manufacturing

environment.[5] In addition to these mechanisms, the interfacial physicochemical bonding (i.e., adhesion) and/or friction between the tool and composite part during processing (i.e., tool-part interaction) also significantly contribute to residual stress formations.[21] Typically, production tools (i.e., molds) are treated with release coatings to reduce the tool-part interaction and resulting residual stresses and PIDs. Release coatings also facilitate the demolding of cured parts after processing.[37,38]

Aerospace manufacturers typically use a three-step process to prepare tool surfaces with release coatings.[39] First, the tool is treated with solvent-based mold cleaner to remove any residue from previous processing/handling and create a clean lay-up surface for the uncured composite material (**Figure 2-1a**). Tooling for high-performance aerostructures is typically made from a durable metallic material with a low coefficient of thermal expansion (CTE), such as Invar, to minimize thermal strains during processing. Depending on the severity of residue build-up on the tool surface from previous usages, manufacturers may also use abrasive cleaning methods (e.g., coarse pads) or non-abrasive industrial methods (e.g., dry-ice blasting) to remove residues before continuing with tool preparation. However, abrasive methods may roughen the tool surface and consequently further promote tool-part interaction in subsequent cycles.

The next step of tool preparation involves applying a mold sealer directly on the cleaned tool surface to fill micro-cavities, cover any scratches, and prevent mechanical interlocking (i.e., physical bonding) between the tool and part (**Figure 2-1b**). Afterward, several layers of release agent (RA) are applied on top of the sealed surface to form a low-energy barrier and prevent the formation of strong adhesive bonds (**Figure 2-1c**).[38] The combination of mold sealer and RA creates an abhesive (i.e., non-adhesive) and impermeable release coating between the tool and part during lay-up and processing (**Figure 2-1d**).

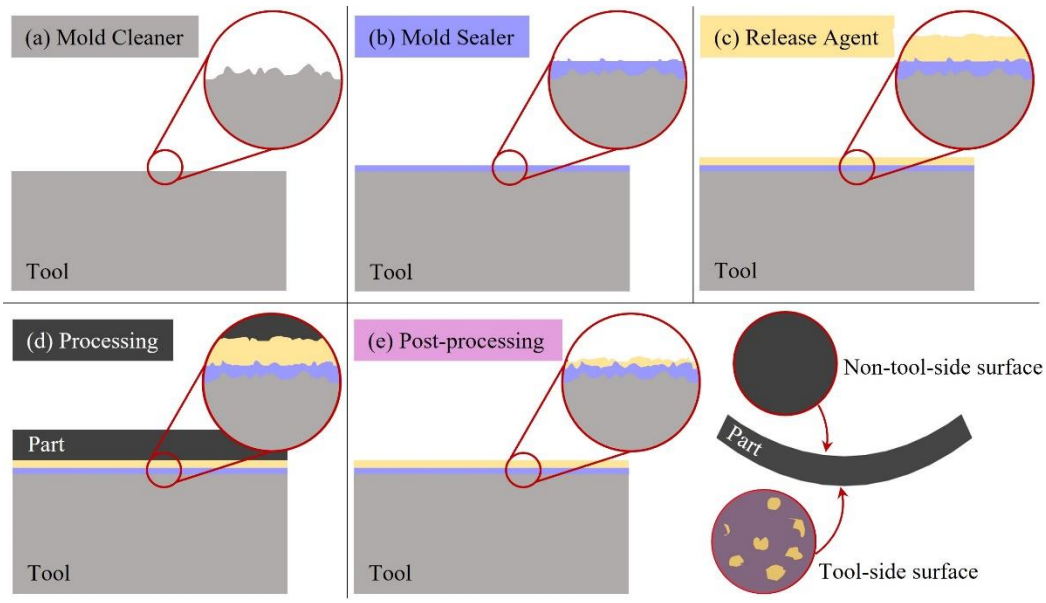

Figure 2-1. (a-d) Standard steps of tool preparation in composites manufacturing, and **(e)** potential effects on a flat composite part.

The aerospace industry generally uses semi-permanent silicone-based release coatings due to their low adhesion (i.e., high abhesion) and high thermochemical stabilities. For example, Loctite® Frekote® B-15™ mold sealer[40] and 710-NC™ release agent[41] are two popular silicone release products used by aerospace manufacturers. Polydimethylsiloxane (PDMS) acts as the functioning silicone in both Frekote components, which allows for chemical compatibility, low surface free energy, and excellent abhesive properties.[38] These products are either sprayed, wiped, rolled, or brushed onto tool surfaces as liquids and cured through an evaporation reaction to form low-energy coating layers on the tool surface.

As the thermoset composite undergoes a cross-linking reaction, some silicone molecules in the release coating transfer from the tool to the part's surface and become physically and chemically integrated into its resin network.[37,40–42] Upon demolding after the cure cycle is completed, these molecules remain on the part's surface as contaminations (**Figure 2-1e**). The

atomic concentration of silicone on cured composite parts may exist in the range of 5–20%, depending on the age and type of release coating applied to the tool before processing.[37]

In addition to the transfer of silicone molecules, while the resin is still in its viscous liquid stage during the early steps of processing, high autoclave temperatures and pressures may force the resin to bleed out from the composite onto the tool.[43–45] As curing progresses, this resin chemically and/or physically bonds to micro-cavities on the tool surface and cures as contamination. Without tool cleaning or recoating steps, each successive processing cycle thus results in a further reduction in the coating thickness and promotion of tool surface contamination. This resultant change in physical and chemical tool surface properties due to processing can be considered the "aging" of the release coating.[46]

While the aging of release coating is widely recognized, the physicochemical mechanisms involved and their impacts on PIDs are not thoroughly understood. For instance, a common industry practice involves spot cleaning contaminations and periodically reapplying fresh RA layers over an aged coating between processing cycles to maintain effective tool-part abhesion. Another approach might entail thoroughly cleaning the tool using abrasives, solvents, or dry-ice blasting (DIB), then re-treating it with fresh layers of mold sealer and RA.[39,47,48] However, these practices are largely based on "know-how" and may inadvertently have impacts on residual stresses and PIDs.[49] Therefore, this section aims to characterize the behavior of aerospace release coating to lower uncertainty levels and provide insights for more effective tool preparation and PID mitigation.

2.1.2 Materials and Methods

The release coating evaluated throughout this research comprised two aerospace-grade products: Loctite® Frekote® B-15™ mold sealer and 710-NC™ release agent. While the exact

formulations of the Frekote products are proprietary, basic information is listed on publicly accessible datasheets.[40,48] To investigate the behaviors of these products, a multi-component testing campaign was conducted, involving physicochemical assessments of release-coated tool surfaces in simulated manufacturing environments. The campaign consisted of tool preparations, autoclave processing cycles, dry-ice blasting (DIB), and physicochemical surface analyses. The methodologies for each of these experimental components are described in the following subsections.

2.1.2.1 Tool Preparations

To begin release coating investigations, a series of laboratory-scale tools was prepared similarly as in industrial settings. A batch of 26 flat coupon-sized tools was first prepared by sectioning 25 mm (w) × 25 mm (l) square portions from a 0.25 mm (t) Invar sheet. Given the selection of flat geometries for the tools, any influences from geometry transition points (e.g., sharp corners) on release coating behavior were disregarded in this investigation. The lab-scale tools exhibited ISO 1302 roughness grades of N2 with Ra values of approximately 0.08 µm, resembling surfaces of industrial tools.[50]

Following the cutting of specimens, the tools were prepared to serve as mold surfaces for autoclave composites processing cycles. Initially, all tools were cleaned with Loctite® Frekote® PMC™ mold cleaner and a lint-free wiping cloth to remove any surface residues from previous cutting or handling.[48] Then, the samples were subjected to various surface treatments, as detailed in **Table 2-1**. The release coating products were applied to the lay-up surfaces of the tools by dipping lint-free wiping cloths into cups containing liquid coating, allowing excess coating to drip back into the cups, then using the cloth to apply the coating to the tool in a circular motion. A fresh cloth was utilized for each coating application. Each coat of B-15 was left to cure in a convection

oven for 60 minutes at 95 °C, while each coat of 710-NC cured for 15 minutes at room temperature before the application of the next coat.[40,41] The two tools left untreated and covered with fluorinated ethylene propylene (FEP) release film were prepared as controlled reference samples.

Table 2-1. Specimens prepared for release coating investigations.

Tool Surface Condition	Number of Specimens
Tool (Untreated)	2
FEP	2
1 Coat 710-NC	2
2 Coats 710-NC	2
3 Coats 710-NC	2
4 Coats 710-NC	2
2 Coats B-15	2
2 Coats B-15 + 1 Coat 710-NC	4
2 Coats B-15 + 3 Coats 710-NC	4
2 Coats B-15 + 5 Coats 710-NC	4

2.1.2.2 Autoclave Processing Cycles

Once all the tools were prepared, they were utilized as mold surfaces for autoclave processing cycles of composites throughout an extensive testing campaign. Before the cycles, the coupons treated with release coating or covered with FEP were adhered to a 3 mm (t) × 300 mm (w) × 600 mm (l) Invar plate using Flashbreaker® tape for support. Subsequently, one ply of T800S/3900-2B UD prepreg with nominal dimensions of 20 mm (w) × 20 mm (l) was laid-up to cover the tool surfaces. Since single-ply composite parts were used for all the processing cycles, the impacts of part thickness were disregarded in this investigation. The Invar plate and lab-scale tools were then covered with one sheet of FEP, followed by one layer of breather cloth. The tools and lay-ups were placed and sealed in separate vacuum envelope bags produced by Torr Technologies (Auburn, WA, USA), loaded into an autoclave, and subjected to the Manufacturer's Recommended Cure Cycle (MRCC).[36] The MRCC consists of a heating ramp from room temperature to 180 °C at 2 °C/min, a temperature hold at 180 °C for 120 minutes, then a cool down

back to room temperature. A combined autoclave and vacuum pressure of approximately 0.7 MPa (~7 atm) was applied throughout processing.

After the cure cycle was completed, the envelope bags were removed from the autoclave, and all composite parts were demolded from the tools. The tools were then stored in sealed bags until the next processing cycle or surface analysis tests were conducted. The processing procedures and cycles were repeated five times for the tools treated only with 710-NC release agent and twenty times for tools treated with both B-15 mold sealer and 710-NC to investigate aging effects. Surface analysis tests, as detailed in the following subsections, were conducted after each processing cycle for the first five cycles, then every five cycles throughout the remainder of the campaign. Before each cycle, tools were wiped with a dry lint-free cloth to remove any surface residue from previous usages. Half of the B-15/710-NC tools were treated with one fresh layer of 710-NC every three cycles, while the other tools underwent twenty autoclave cures without receiving any reapplications. This approach was used to investigate the effects of release agent touch-ups on the aging process.

After the processing campaign, the surfaces of the B-15/710-NC tools were dry-ice blasted using a ColdJet® Aero$_2$ Particle Control System™ (PCS®) 60.[51] The PCS 60 propels recycled solid carbon dioxide (CO_2) pellets at supersonic speeds, causing them to sublimate upon impact with a solid surface and remove any contaminates present. Aerospace manufacturers commonly use the ColdJet system to clean various materials for tooling, maintenance, surface preparation, and other production purposes. The PCS 60 allows users to adjust blasting parameters and machine settings for each unique cleaning application.[51] In this study, a feed rate of 1.0 lb/min, blast pressure of 100 psi, and applicator size of 1” was chosen for tool cleaning based on recommendations provided by a ColdJet technician.

2.1.2.3 Surface Analysis Tests

As mentioned earlier, the surfaces of laboratory tools underwent analyses after every autoclave cycle for the initial five cycles, then every five cycles throughout the rest of the campaign. The first component of each surface analysis test involved examining the physical morphology of the coatings using laser scanning digital microscopy. For each test, an Olympus OLS4100 instrument was utilized to generate three absorbance and height micrographs of the release-coated tools with varying amounts and ages of release coating. The tool-side surface of a cured laminate fabricated on a freshly coated tool was also imaged using the OLS4100 microscope for investigative purposes.

After conducting microscopy, Fourier-transform Infrared Spectroscopy (FTIR) analyses were performed on the tools using a Bruker Vertex 70 on the basis of attenuated total reflectance (ATR). Three ATR-FTIR spectra were scanned on each tool in a spectral range of 400 – 4000 cm^{-1}. These spectra were then normalized based on each test's maximum peak height, which remained consistent throughout the campaign.

The final stage of the tool assessments was performing contact angle goniometry measurements with an AST Optima Video Contact Angle (VCA) System. Five 1-µl droplets of deionized (DI) water and diiodomethane (DIM) were dispensed on each tool using the VCA's motorized syringe. Side-view images and contact angles of each droplet were then obtained immediately after solid-liquid contact using the VCA system. The five DI water and DIM contact angles were used in conjunction to create 25 polar-dispersive contact angle pairs for each surface condition. Next, the contact angle pairs were used to calculate surface free energy (SFE) using the Owens–Wendt equation:[52]

$$(\gamma_S^d \gamma_l^d)^{0.5} + (\gamma_S^p \gamma_l^p)^{0.5} = 0.5\gamma_l(1 + cos\theta) \quad (2\text{-}1)$$

where γ_S^d is the solid surface's dispersive SFE component, γ_S^p is the solid surface's polar SFE component, γ_l^d is the dispensed liquid's dispersive tension, γ_l^p is the dispensed liquid's polar tension, γ_l is the dispensed liquid's overall tension equal to the sum of its dispersive and polar components, and θ is the dispensed liquid's contact angle immediately after solid–liquid contact with the solid surface. The dispersive and polar tensions of DI water were assumed to be 22.1 dyne/cm and 50.7 dyne/cm, respectively. The dispersive and polar tensions of DIM were assumed to be 48.5 dyne/cm and 2.3 dyne/cm, respectively.[52] From the liquid tension properties and measured contact angles of two liquids, a system of two equations was established, then γ_S^d and γ_S^p were solved for. Finally, the total SFE of the tool surface was calculated by summing γ_S^d and γ_S^p together.

2.1.3 Results and Discussions

2.1.3.1 Morphology

Figure 2-2a–c exhibits three-dimensional micrographs of pre-production Invar tools with different surface treatments: untreated (i.e., no release coating), treated with two coats of B-15 mold sealer, and treated with two coats B-15 mold sealer plus three coats of 710-NC release agent. The micrographs illustrate that upon the application of recommended amounts of mold sealer and release agent, the coating products form agglomerations (i.e., bumps) rather than smooth layers. This phenomenon occurs due to the low SFE properties of B-15 and 710-NC.[53]

Figure 2-2d portrays the fully coated B-15/710-NC tool surface after autoclave processing, revealing that the elevated pressures and temperatures (i.e., 7 atm and 180 °C) applied caused the release coating to flow and spread. This is because the processing temperatures were well above the glass transition temperature (T_g) of the coating's active silicone component (~130 °C),

polydimethylsiloxane (PDMS), causing the agglomerations to behave rubbery.[38] Consequently, this behavior created a relatively smooth barrier between the tool and the part during processing.

Finally, **Figure 2-2e** demonstrates that autoclave conditions also caused some silicone molecules in the release coating to transfer from the tool and contaminate the composite part's surface. These findings confirm additional negative impacts of release coating, such as influencing the bonding quality of composite parts, and emphasize the necessity for surface pre-treatments during the assembly process.[37,42,54,55]

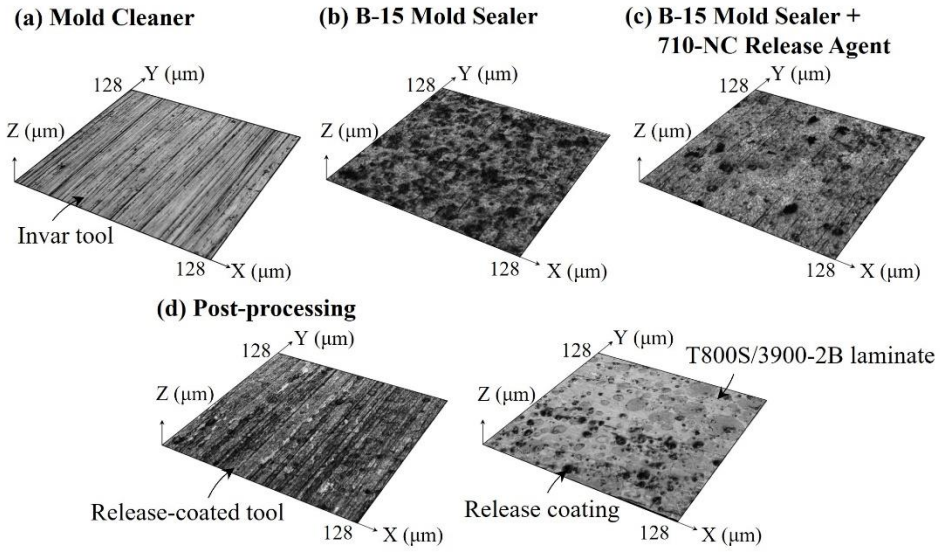

Figure 2-2. Micrographs of Frekote B-15/710-NC release coating's behavior during tool preparation and composites processing.

Figure 2-3 presents three-dimensional height maps of tools coated with one to four Frekote 710-NC layers compared with the untreated and FEP-covered tools. The figure reveals distinct surface characteristics on tools treated with different release agent quantities. For instance, the tool treated with one release coat has a similar height profile and grain visibility to the untreated tool. This suggests that a single application of 710-NC may not adequately cover significant tool surface irregularities (e.g., grains, cavities, scratches) that would otherwise promote tool-part interaction.[9]

On the other hand, the tools treated with two, three, and four release coats demonstrate a mitigation of most surface irregularities.

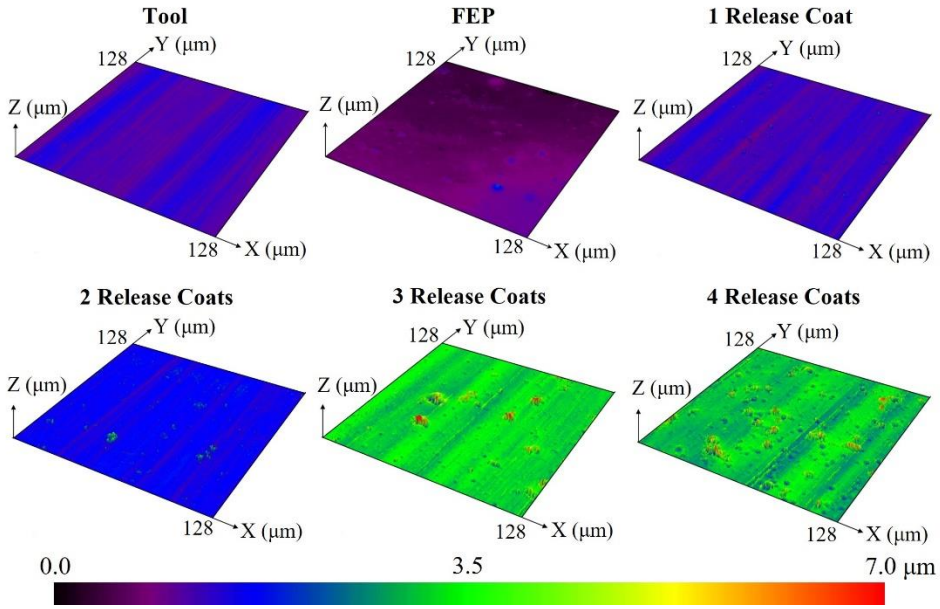

Figure 2-3. Height maps of tools treated with different numbers of Frekote 710-NC release coats compared with untreated and FEP-covered tools.

In addition to an increase in overall coating thickness, the two-, three-, and four-coat micrographs show that each additional application of release agent leads to a greater number and larger size of agglomerations (i.e., bumps) on the tool surfaces, thereby directly increasing roughness (**Figure 2-4**). As previously mentioned, these micro-agglomerations form when a fresh coat of 710-NC is applied to a surface with low SFE, such as another cured release coating layer.[53] Such variations in surface topography may significantly impact the tool's physicochemical properties, tool-part interaction, and PIDs during processing.[9,56]

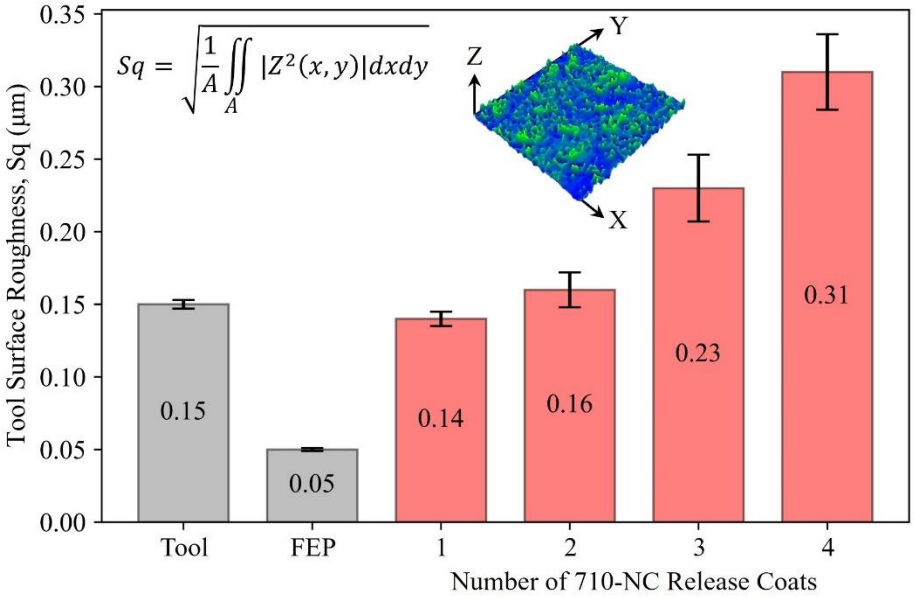

Figure 2-4. Surface roughness of tools treated with different numbers of Frekote 710-NC release coats compared with untreated and FEP-covered tools.

Figure 2-5 and **Figure 2-6** display height maps and surface roughness values of a tool treated with two coats of B-15 mold sealer and three coats of 710-NC release agent after undergoing successive composites processing cycles. A first notable observation from these figures is that applying both B-15 and 710-NC products results in a comparitively smooth barrier, in contrast to the rougher surface observed when using 710-NC (**Figure 2-3**). This suggests the advantageous use of both products together in attempting to minimize tool-part interaction and PIDs. **Figure 2-5** also demonstrates a clear reduction in B-15/710-NC coating thickness with each processing cycle, supporting the industrial basis of reapplying release agent layers between processing cycles to maintain a thick coating on the tool. Lastly, **Figure 2-6** depicts a generally increasing trend in roughness as the release-coated tool underwent processing cycles, despite some standard deviation overlaps. This trend is also evident in the micrographs, where aged tools exhibted higher levels of agglomeration compared to fresh ones.

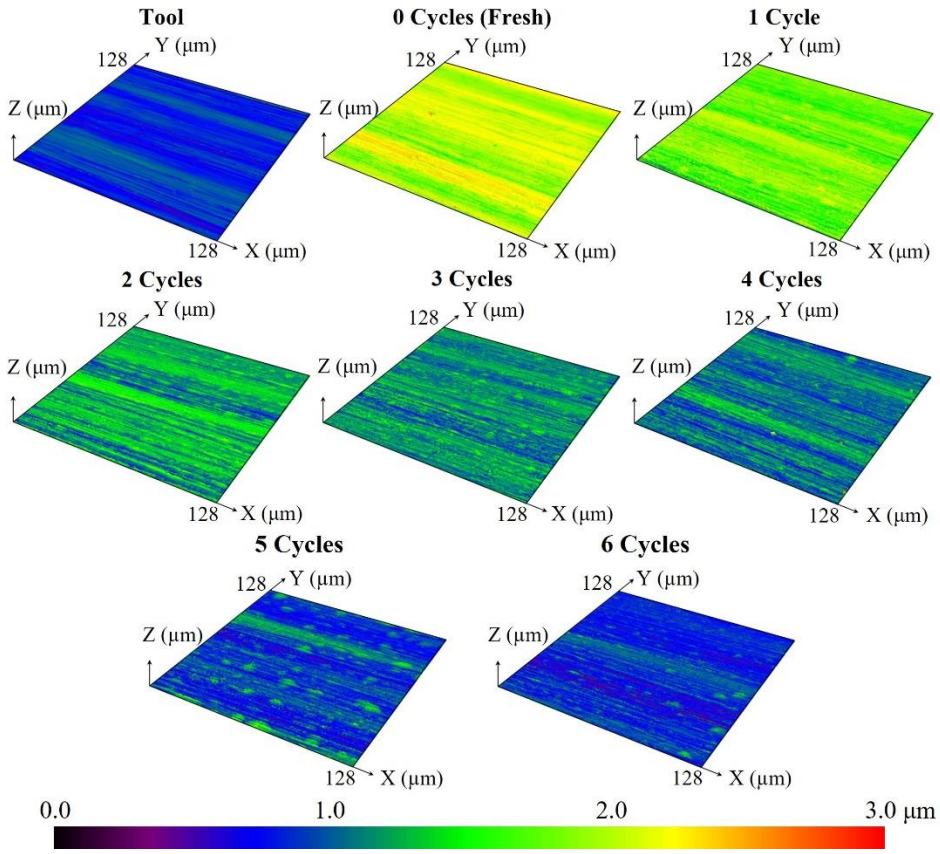

Figure 2-5. Height maps of a tool treated with B-15/710-NC release coating as it underwent six successive composites processing cycles.

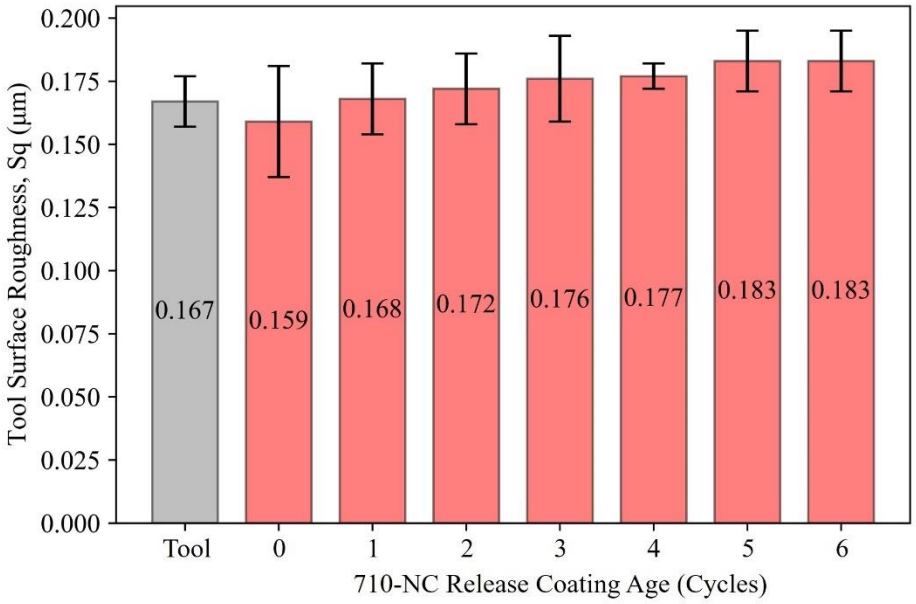

Figure 2-6. Surface roughness of a tool treated with B-15/710-NC release coating as it underwent six successive composites processing cycles.

2.1.3.2 Surface Chemistry

Figure 2-7 compares ATR-FTIR spectra for industry-recommended quantities of B-15 mold sealer (i.e., two coats), 710-NC release agent (i.e., three coats), and B-15/710-NC release coating (i.e., two coats + three coats). In the plots, darker colors represent the average of three spectra for each surface condition, while lighter colors include regions within the standard deviations. Prior to plotting, all absorbance spectra were normalized using asymmetric least squares (ALS) baseline subtraction in OriginPro analysis software.[57]

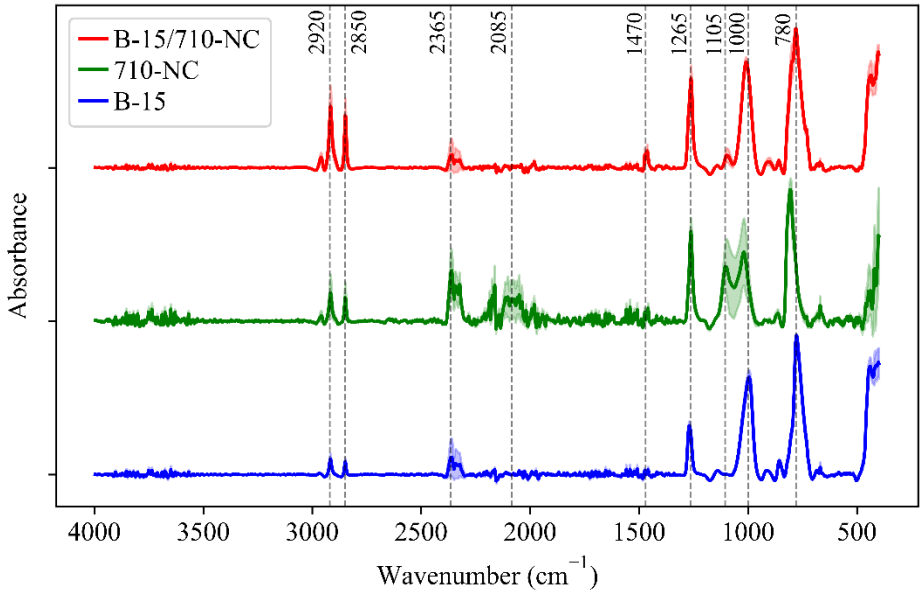

Figure 2-7. ATR-FTIR spectra of a tool treated with B-15 mold sealer, 710-NC release agent, and B-15/710-NC release coating.

All three spectra exhibit similar general peaks at wavenumbers around 2920 cm^{-1}, 2850 cm^{-1}, 2365 cm^{-1}, 2085 cm^{-1}, 1470 cm^{-1}, 1265 cm^{-1}, 1105 cm^{-1}, 1000 cm^{-1}, and 780 cm^{-1}. The four peaks at 780 cm^{-1}, 1000 cm^{-1}, 1105 cm^{-1}, and 1265 cm^{-1} are characteristic of silicone materials, specifically, a polydimethylsiloxane (PDMS) polymer network. The peak at 780 cm^{-1} represents Si-CH_3 bond stretching. The peaks at 1000 cm^{-1} and 1105 cm^{-1} represent the asymmetric stretching of Si-O-Si bonds. The peak at 1265 cm^{-1} is characteristic of the symmetrical

deformation of the C-H bond in the Si-$(CH_3)_2$ groups (i.e., Si-CH_3 bending). The weaker peaks at 1470 cm^{-1} and 2365 cm^{-1} represent C-H scissoring and O=C=O stretching, respectively. The strong cluster around 3000 cm^{-1} signifies asymmetric C-H stretching. Finally, the relatively noisy peaks around 2000 cm^{-1} suggest the presence of water molecules on the sample.[38,42,58]

Figure 2-7 reveals that B-15 mold sealer and 710-NC release agent share similar chemical characteristics with some distinctions. Most notably, the 710-NC spectrum shows split peaks at 1105 and 1000 cm^{-1}, while the B-15 tool displays a single peak at 1000 cm^{-1}, and B-15/710-NC shows a minor peak at 1105 cm^{-1}. Furthermore, the 710-NC sample presents indistinct peaks around 2085 cm^{-1}, indicative of water molecules on the tool surface. This discrepancy arises because the 710-NC coats were cured at room temperature in an ambient environment, whereas the B-15-treated samples underwent curing in a convection oven at elevated temperatures, effectively removing the water molecules. Overall, the spectra in **Figure 2-7** underscore the similar PDMS-based chemical structures of Frekote mold sealer and release agent, which forms the basis of their chemical compatibilities. It should also be noted that the same trends were observed for samples treated with all investigated amounts of B-15 and 710-NC (**Table 2-1**).

Figure 2-8 illustrates ATR-FTIR spectra for a tool treated with three coats of 710-NC release agent after undergoing varying numbers of composites processing cycles. The figure highlights significant chemical contrasts between the fresh and aged samples. Specifically, the split peaks at 1000 cm^{-1} and 1105 cm^{-1} were notably short with high deviation in the unaged sample. The fresh sample also exhibited clustered water peaks around 2000 cm^{-1}. After one cycle, the 1000 cm^{-1} and 1105 cm^{-1} peaks elongated and showed lower deviation, while the water cluster almost entirely disappeared. This chemical structure then remained relatively constant throughout the subsequent cycles.

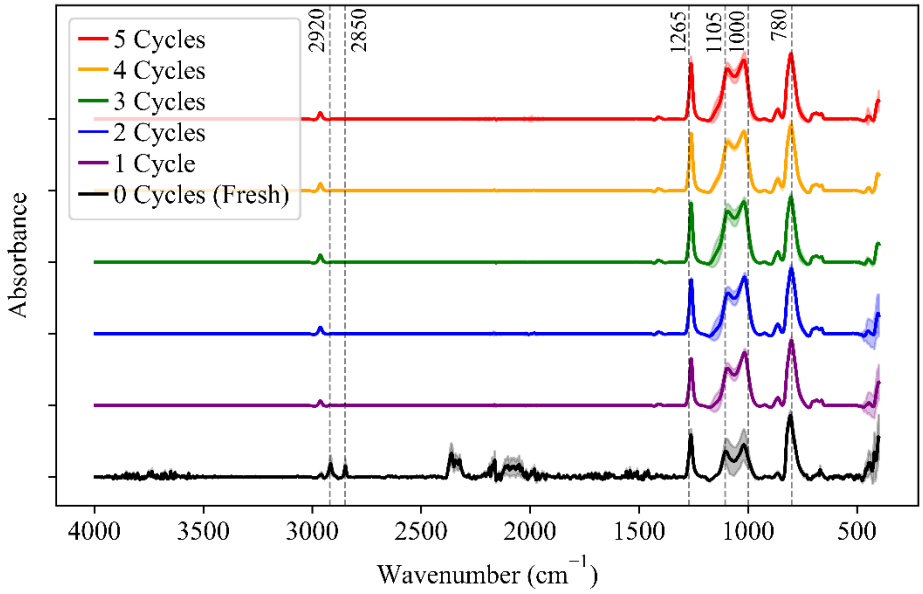

Figure 2-8. ATR-FTIR spectra of a tool treated with 710-NC release agent subjected to different numbers of composites processing cycles.

The distinctions between the fresh and aged samples can be attributed to the tool becoming "conditioned" to the release agent, a consequence of using a new and freshly coated tool. During a production tool's first few processing cycles, external temperatures and pressures cause non-silicone components, including solvent carriers, water, and other molecules, to flash off or transfer to the part, while silicone molecules are "baked" into the mold.[41] These conditioning mechanisms cause variations in the release agent's chemical composition (i.e., silicone levels), as captured in the spectra of **Figure 2-8**. Once the tool becomes conditioned, the release agent properties are considered "locked-in" and remain stable until significant aging effects may cause silicone levels and tool abhesion to decline. The absence of chemical distinctions between the one- to five-cycle samples suggests that such chemical aging effects, including transfers of resin molecules to the tool surface, do not occur in the 710-NC release coating within five cycles. Therefore, conducting more processing cycles would likely be necessary to observe such effects.

Figure 2-9 depicts chemical differences between freshly coated and aged tool surfaces treated with two coats of B-15 mold sealer and three coats of 710-NC release agent. Similar to the 710-NC findings, these spectra also reveal conditioning effects. However, these effects are demonstrated to manifest after one cycle for the B-15/710-NC, whereas differences in 710-NC were observed only for the fresh cycle. This observation may imply that more processing cycles are needed to adequately condition a tool with B-15/710-NC release coating. Furthermore, **Figure 2-9** indicates that the B-15/710-NC coating remains chemically stable through twenty processing cycles, suggesting that frequent reapplications of release agent in industrial settings are likely unnecessary to maintain chemical performance. Lastly, it should be noted that the same trends were observed for samples treated with B-15 mold sealer plus one and five layers of 710-NC release agent.

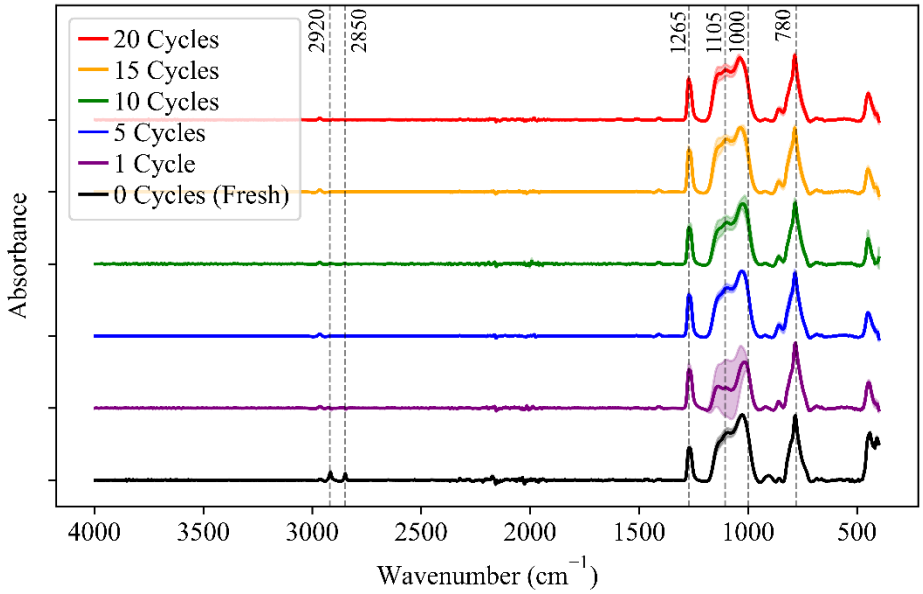

Figure 2-9. ATR-FTIR spectra of a tool treated with B-15/710-NC release coating subjected to different numbers of composites processing cycles.

Figure 2-10 presents a chemical comparison between various conditions of a B-15/710-NC-treated tool: freshly coated, aged twenty cycles with and without reapplications every three

cycles, and following dry-ice blasting (DIB). Firstly, the figure reaffirms that aged B-15/710-NC remains chemically similar to fresh release coating through twenty processing cycles. However, the figure also illustrates that the periodic reapplication of 710-NC release agent may introduce some chemical revitalizations in the coating. The addition of 710-NC causes the split peaks around 1000 cm^{-1} to merge and resemble the 710-NC release agent spectra (**Figure 2-7**). Finally, the low absorbance measurements observed on the tool after undergoing DIB cleaning indicate a lack of silicone on the tool surface, validating the ColdJet equipment as an effective method for removing release coating. It should be noted that the trends discussed were observed for samples treated with all different amounts of B-15 and 710-NC considered.

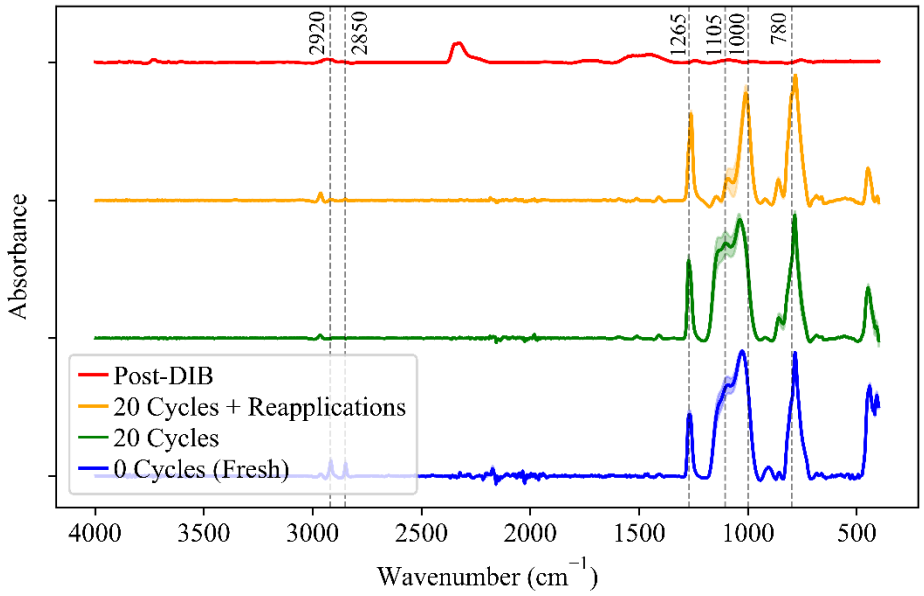

Figure 2-10. ATR-FTIR spectra of a tool treated with B-15/710-NC release coating subjected to different numbers of composites processing cycles, reapplications, and dry-ice blasting (DIB).

2.1.3.3 Surface Free Energy

Figure 2-11 displays surface free energy (SFE) values measured on tool surfaces treated with different amounts of B-15 mold sealer and 710-NC release agent. The reported SFE values represent the average of 25 measurements, while error bars include the corresponding standard

deviations within each measurement set. The plot demonstrates several distinct physicochemical variations between the surface conditions.

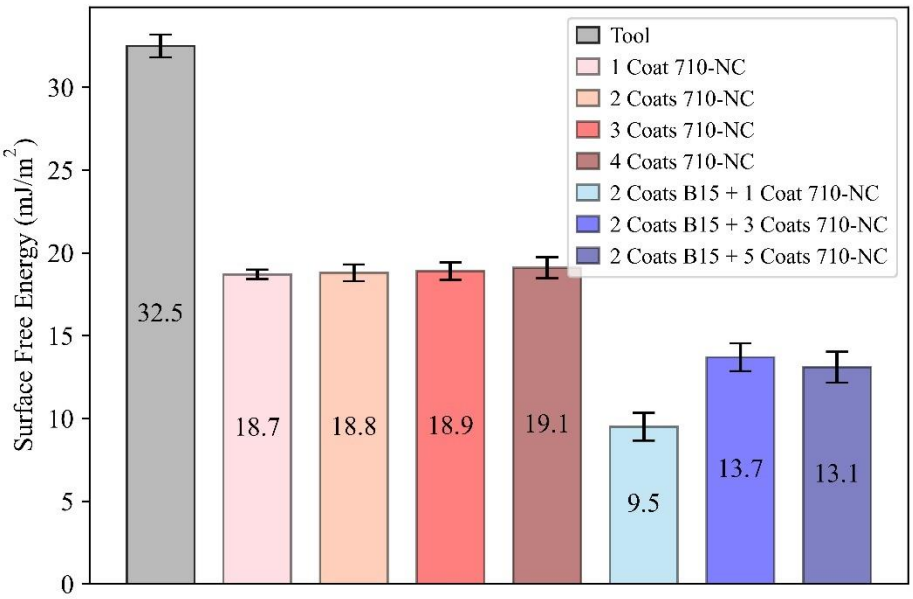

Figure 2-11. Surface free energy of a tool treated with different amounts of Frekote B15 mold sealer and 710-NC release agent.

For instance, the introduction of 710-NC release agent reduced the tool's SFE from approximately 32 to 19 mJ/m^2, while the application of both B-15 and 710-NC further lowered the SFE. The lowest SFE value was observed for a tool treated with two coats of B-15 and one coat of 710-NC, while the highest was for a tool treated with four 710-NC coats. In both cases, these exceptionally low SFE values indicate Frekote B-15 and 710-NC are highly abhesive (i.e., non-adhesive), with the most favorable configuration for reducing tool-part chemical bonding being two coats of B-15 and one coat of 710-NC.

Another noteworthy observation from **Figure 2-11** is the slight increase in average SFE values and deviations with each applied 710-NC coat. The trends observed in average measurements suggest that the degree of chemical bonding between a composite part and a tool surface treated solely with 710-NC may be slightly sensitive to the number of coats applied before

processing. The larger scatter in measurements on tools treated with higher numbers of 710-NC coats is likely attributable to a greater presence of non-uniform agglomerations (**Figure 2-3**), which affects the repeatability of tests.[53,59]

Figure 2-12 illustrates the SFE progression of a tool surface treated with two coats of B-15 mold sealer and three coats of 710-NC after twenty successive autoclave processing cycles. The measurements reveal that initially, the release-coated tool exhibited an SFE of 13.7 mJ/m^2. This value then declined to a minimum of 8.3 mJ/m^2 during the first two processing cycles, then generally increased throughout the remainder of the campaign. The initial SFE reduction during the first two cycles is likely due to conditioning effects causing non-silicone components to evaporate during the initial processing cycles. This process leaves the active low-energy silicones exposed on the tool surface, resulting in reduced SFE properties.

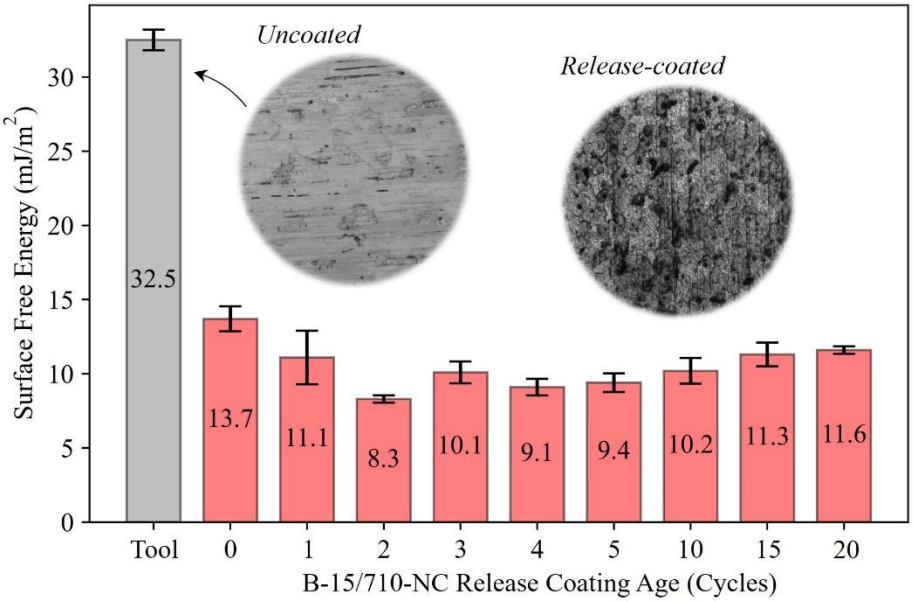

Figure 2-12. Surface free energy of a tool treated with B-15/710-NC release coating subjected to different amounts of composites processing cycles.

The subsequent general increase in SFE after the first two cycles can be attributed to the transfer of silicone molecules from the tool to the part (**Figure 2-2**), leaving spots on the tool

surface devoid of silicone and with higher SFE. These same overall trends were observed for all tools treated with B-15 and varying amounts of 710-NC. Overall, the findings in **Figure 2-12** suggest that tools treated with Frekote B-15/710-NC should undergo two processing cycles for adequate conditioning and minimizing tool-part interaction during processing.

Figure 2-13 presents a comparison in SFE between various conditions of a B-15/710-NC-coated tool: aged twenty cycles with and without reapplications every three cycles, and following dry-ice blasting (DIB). Throughout the twenty processing cycles, all tools remained highly abhesive, with SFEs of approximately 11 – 12 mJ/m^2, regardless of the initial number of 710-NC release agent layers applied. The figure also demonstrates that periodic reapplications of 710-NC have marginal effects on SFE properties, resulting in only slightly lower SFE values over the twenty-cycle campaign.

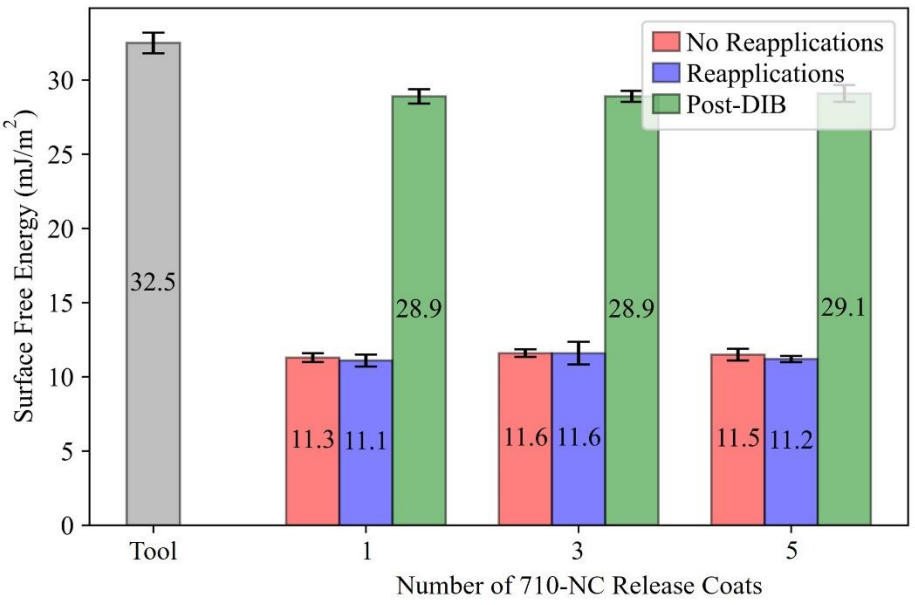

Figure 2-13. Surface free energy of a tool treated with B-15 mold sealer plus different numbers of 710-NC release coats subjected to twenty composites processing cycles, with and without reapplications, and dry-ice blasting (DIB).

After DIB cleaning, SFEs of approximately 29 mJ/m^2 were measured for all conditions with minimal variations. These intermediate values reinforce the ColdJet machine's ability to

effectively remove release coating from tool surfaces. However, the values were slightly lower than those of the untreated tool, suggesting that trace amounts of release coating molecules may persist on the tool surface after DIB cleaning. Consequently, additional methods such as solvent or abrasive cleaning may be necessary for complete removal of the coating.

2.2 T800S/3900-2B PREPREG

2.2.1 Background

Achieving high dimensional accuracy in composites manufacturing heavily relies on comprehending correlations between processing parameters and the composite's thermo-mechanical properties.[5] Since characterizing many of these relationships demands significant time, labor, and financial investments, several potentially impactful phenomena remain poorly understood, particularly for current-generation aerospace materials. This sub-chapter aims to reduce uncertainty levels by investigating and characterizing T800S/3900-2B from a physico-mechanical perspective, hoping to serve as a foundation for more effective mitigation of PIDs.

2.2.2 Materials and Methods

2.2.2.1 Morphology Tests

The initial phase of T800S/3900-2B analyses involved investigating the physical morphology of the prepreg and cured laminates in various manufacturing conditions. One primary goal was to explore the impacts of cure pressure on the physical attributes of thermoplastic tougheners, which have been largely overlooked in existing literature. To accomplish this, a laminate preparation stage was initiated to fabricate a series of laboratory-scale composite parts, reflective of those encountered in industrial settings. Initially, a batch of 24 UD prepreg plies, each with dimensions of 25 mm (w) × 25 mm (l), was sectioned using an X-ACTO knife. Subsequently, an Invar tool was covered with a single layer of FEP release film to serve as a mold surface for

autoclave composites processing cycles. Two UD laminates with two plies each were then laid up on the mold surface and cured in an autoclave under varying pressures. A total of five curing pressures were tested in separate processing rounds: 101, 222, 347, 555, and 763 kPa. During each cycle, full vacuum pressure was maintained on the laminates, while the autoclave pressure was adjusted. The final four remaining prepreg plies were stacked into two UD laminates and were left uncured in a freezer until subsequent analyses were conducted.

After each autoclave cycle, an Olympus OLS4100 microscope was utilized to capture three micrographs of the laminates' tool-side surfaces cured under different pressures. The composite parts were then embedded in EpoxiCure™ 2 mounting compound following recommended procedures, cross-sectioned using an Allied High Tech Products TechCut 4™ precision slow-speed saw, and examined under an Olympus BX-50 digital light microscope. Lastly, the uncured laminates were analyzed using a Phenom ProX scanning electron microscope (SEM) with a 10 kV beam voltage.

2.2.2.2 Viscoelasticity Tests

The second analysis phase involved investigating the viscoelastic (VE) properties of a T800S/3900-2B laminate cured according to the manufacturer's guidelines. First, twelve prepreg plies were cut into dimensions of 12.54 mm (w) × 60 mm (l) with fibers orientated transversely. These plies were then layered onto a tool covered with FEP to form a $[90]_{12}$ laminate. The laminate was then covered with another FEP layer, a caul plate, breather cloth, and vacuum sealed before undergoing autoclave curing according to MRCC procedures.[36] After curing, the laminate was demolded from the tool and cooled to room temperature.

Subsequently, the laminate underwent dynamic 3-point bend testing using a TA Instruments® Discovery Dynamic Mechanical Analyzer (DMA) 850. The experimental setup for

the DMA tests is shown in **Figure 2-14**. The testing protocol involved heating from -100 °C to 250 °C at 5 °C/min while applying a 150-µm dynamic displacement to the beam through the instrument's moveable clamp. Three tests were conducted using this procedure, with the frequency of the dynamic load set to different values: 0.1, 1, and 10 Hz. Following the tests, loss and storage moduli throughout the temperature sweeps were directly extracted from the DMA.

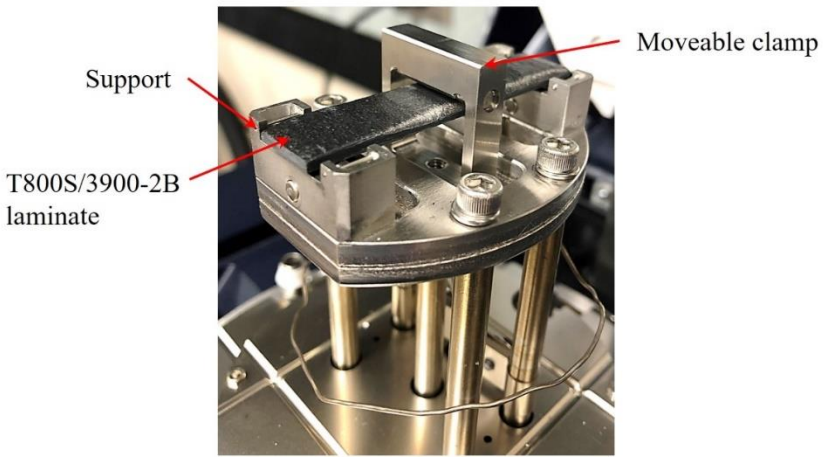

Figure 2-14. DMA 3-point bend testing setup for investigating viscoelastic behaviors of cured T800S/3900-2B laminates.

2.2.2.3 Thermo-mechanical Tests

The next phase of investigation involved characterizing the evolution of T800S/3900-2B's dynamic modulus and free strains (i.e. cure shrinkage and thermal strains) during cure. This task was achieved by slightly modifying a previously developed technique.[60] The experimental setup, shown in **Figure 2-15**, consisted of a bi-material beam (BMB) supported by a 3-point bend fixture within the DMA 850. Each BMB consisted of four layers of 90-degree prepreg bonded together on top of a steel shim. During each DMA test, the steel shim is an essential component of each sample as it supports the prepreg in early stages of a cure cycle (i.e., prior to gelation) when it has insufficient modulus to support itself.

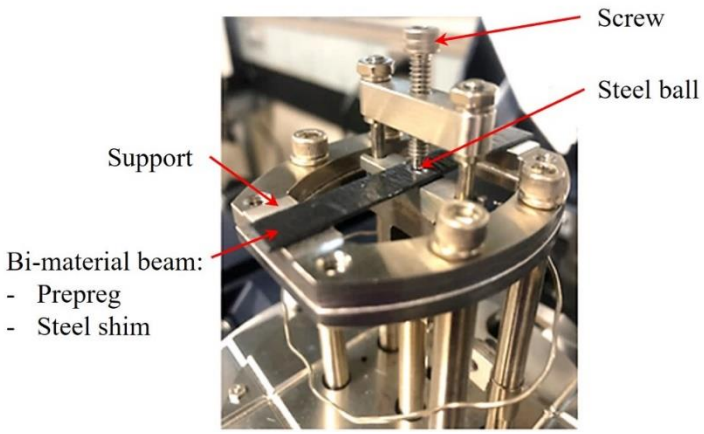

Figure 2-15. DMA bi-material beam (BMB) testing setup for characterizing modulus and free strain developments during composites processing cycles.

To prepare BMB specimens for DMA testing, first, 18 shims with nominal dimensions of 12.7 mm (w) × 60 mm (l) × 0.127 mm (t) were cut from Precision Brand® steel feeler gauge blades using a manual shear/brake machine.[61] Then, one side of each shim underwent light abrasion using 400 grit sandpaper to remove any oxidation and residue from previous cutting or handling. Sanding was conducted along each shim's longitudinal direction for 20 seconds, then transversely for another 20 seconds, with light pressure applied to ensure the thickness of each shim was not significantly altered. After cleaning the sanded shims with acetone and a lint-free cloth, the prepreg was prepared by cutting four 150 mm (w) × 300 mm (l) T800S/3900-2B plies with the fibers aligned longitudinally, stacking them to create a four-ply UD laminate, then debulking for five minutes at room temperature using a standing vacuum bagging procedure.

After completing the initial prepreg debulking, the shims were placed abraded-sides down onto the prepreg at a 90° angle with respect to the fibers, leaving several millimeters of space between each shim. The shim/prepreg configuration then underwent another round of room-temperature debulking for two hours using standard vacuum bagging procedures. Upon finishing the second debulking phase, individual BMB specimens were sectioned using an X-ACTO knife. A two-millimeter biopsy punch was then employed to create a hole through the entire four prepreg

layers in the center of each sample, leaving a small circle of shim exposed. A two-millimeter steel ball was then placed into the hole of each beam and compressed using a hand press, creating a small indentation on the shim's underside. The steel ball is essential to each BMB to prevent creep during the tests, as applying load directly on the prepreg would lead to undesired deformation of the beam. The indentation ensures that the ball remains stationary during DMA testing. Finally, each BMB sample was sealed in a bag with a moisture-absorbing desiccant pack and stored in a freezer until required for DMA testing.

Before each DMA test, one bag containing a BMB sample was retrieved from the freezer and allowed to ambiently thaw to room temperature. Subsequently, the bag was unsealed, and the BMB specimen underwent hot-debulking at 60 °C for 30 minutes using a hot plate and standard vacuum bagging procedures. This step aimed to enhance the adhesion between the steel shim and prepreg before initiating each DMA test. Following the completion of the hot debulking, the BMB sample was extracted from the vacuum bag and ambiently cooled to room temperature.

The BMB testing procedure involved loading each sample into the DMA's 3-point bend fixture and subjecting it to a temperature cycle. Nine cure cycles were used to characterize T800S/3900-2B's mechanical properties under different thermal loading conditions inducing gelation and vitrification at diverse temperatures. Each cycle was repeated to account for material and process variabilities during the subsequent analyses. The generalized profile of each cycle is schematically shown in **Figure 2-16**. Each cycle began with heating to an elevated temperature (T_1) at a rate of 2 °C/min and holding at this temperature until the material reached full vitrification ($T_g > T + 28$ °C).[62] The holding temperatures and times required for vitrification were determined using Dykeman's cure kinetics model and are listed in **Table 2-2**.[63] Following vitrification, the specimens were cooled to room temperature at 2 °C/min and held for 10 minutes,

then heated to 200 °C at 2 °C/min and held for an additional 10 minutes before undergoing a final cooldown. The final temperature ramp and hold at 200 °C were implemented to ensure the material reached a final degree of cure of approximately 90% across all cycles.

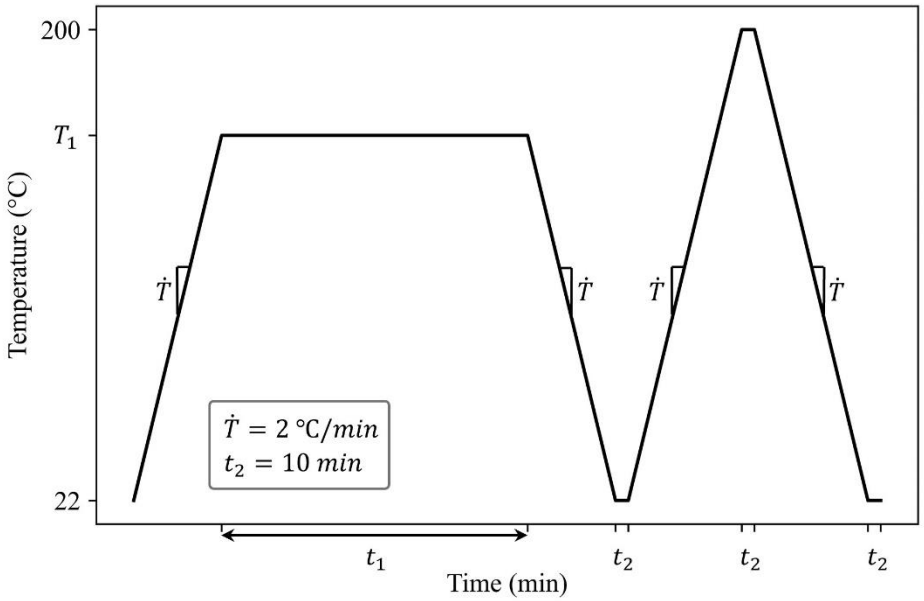

Figure 2-16. Generalized profile of temperature cycles used for bi-material beam (BMB) tests.

Table 2-2. Intermediate hold temperatures and times used throughout bi-material beam (BMB) testing campaign.

Hold Temperature, T_1 (°C)	Hold Time, t_1 (min)
120	900
130	600
140	420
150	300
160	240
170	180
180	120
190	120
200	120

Throughout each cure cycle, the BMB specimens were also subjected to a continuous sinusoidal displacement with an amplitude and frequency of 150 μm and 0.1 Hz, respectively. A static force of 0.1 N was also applied on the beam to ensure continuous contact between the screw and steel ball throughout the cycle. The dynamic amplitude of 150 μm was chosen to ensure that

modulus measurements were accurate, based on previous studies.[60] The relatively low frequency of the dynamic force was chosen such that the storage modulus measured using this method could be considered the approximate elastic modulus in the Cure Hardening Instantaneously Linear Elastic (CHILE) pseudo viscoelastic (PVE) model for calculating residual stresses.[34,64–66] The CHILE framework is well-established and widely used in the aerospace industry as a cost- and computationally-efficient alternative to full viscoelastic (VE) calculations.[64] In this approach, PVE stresses are calculated in the material as a function of storage modulus and free strains:

$$\sigma(t) = \int_0^t E'(T,\alpha)\frac{d\varepsilon - d\varepsilon_{free}}{d\tau}d\tau \tag{2-2}$$

where σ is the stress, t is the time, E' is the material's instantaneous storage modulus evaluated as a function of temperature (T) and degree of cure (α), ε is the total strain, ε_{free} is the free thermo-chemical strain, and τ is a dummy time-integration variable.

Throughout each BMB test, the DMA measured the applied force necessary to displace the beam and the load-displacement phase angle at discrete time-steps. After each cycle, the measured displacement ($\Delta_{dynamic}$), force ($F_{dynamic}$), and phase angle (δ) values were used to calculate the evolution of the beam's effective stiffness (EI_{eff}). Since the loading is dynamic during BMB testing, EI_{eff} computations are modified to account only for the storage component:

$$EI_{eff} = \frac{F_{dynamic}L^3}{48\Delta_{dynamic}}Cos\delta \tag{2-3}$$

where L is the length of the BMB specimen. Using the beam's known dimensions, the prepreg's storage modulus throughout the cure cycle was then decoupled using the following equation:[60]

$$EI_{eff} = \frac{bt_s^3 t_c E_s E_c}{12(t_s E_s + t_c E_c)}\left(4 + 6\frac{t_c}{t_s} + 4\left(\frac{t_c}{t_s}\right)^2 + \frac{E_c}{E_s}\left(\frac{t_c}{t_s}\right)^3 + \frac{E_s t_s}{E_c t_c}\right) \tag{2-4}$$

where b is the BMB's width (12.7 mm), t_s is the steel shim's thickness (0.127 mm), t_c is the prepreg's thickness (4 × 0.191 mm)[36], E_s is the steel shim's modulus extracted from DMA measurements prior to the composite's gelation point, and E_c is the prepreg's modulus (only unknown).

During BMB testing, the initially flat beam develops concave-down curvature and deflects downwards due to a mismatch of free strains from cure shrinkage and thermal effects:

$$\Delta_{cs+th} = R - RCos\left(\frac{L}{2R}\right) = \frac{1 - Cos(L\kappa/2)}{\kappa} \tag{2-5}$$

where Δ_{cs+th} is the BMB's out-of-plane deflection, R is the BMB's radius of curvature, and κ is the BMB's curvature. After obtaining κ, through-thickness free strains in the composite (ε_{free_c}) throughout the DMA cycle were computed using PVE Laminated Plate Theory (LPT), known thermal properties of steel, and the composite's modulus:[26,65,67]

$$\text{Hardening Material: } \begin{Bmatrix} E_c t_c d\varepsilon_{free_c} + E_s t_s \alpha_s dT \\ E_c t_c \overline{Z_c} d\varepsilon_{free_c} + E_s t_s \overline{Z_s} \alpha_s dT \end{Bmatrix} = \begin{bmatrix} A' & B' \\ B' & D' \end{bmatrix} \begin{Bmatrix} d\varepsilon_0 \\ d\kappa \end{Bmatrix} \tag{2-6}$$

$$\text{Softening Material: } \begin{Bmatrix} E_c t_c \varepsilon_{free_c} + E_s t_s \alpha_s dT \\ E_c t_c \overline{Z_c} \varepsilon_{free_c} + E_s t_s \overline{Z_s} \alpha_s dT \end{Bmatrix} = \begin{bmatrix} A' & B' \\ B' & D' \end{bmatrix} \begin{Bmatrix} \varepsilon_0 \\ \kappa \end{Bmatrix} \tag{2-7}$$

where α_s is the steel's coefficient of thermal expansion (1.25 × 10^{-5}/°C) and the remaining terms are calculated as follows:

$$\overline{Z_c} = -t_s/2 \tag{2-8}$$

$$\overline{Z_s} = t_c/2 \tag{2-9}$$

$$A' = E_c t_c + E_s t_s \tag{2-10}$$

$$B' = E_c t_c \overline{Z_c} + E_s t_s \overline{Z_s} \tag{2-11}$$

$$D' = E_c \frac{t_c \overline{Z_c}^2 + t_c^3}{12} + E_s \frac{t_s \overline{Z_s}^2 + t_s^3}{12} \tag{2-12}$$

During analysis, cure shrinkage and thermal expansion of the prepreg may then be decoupled from free strain values by assuming strains generated during a temperature hold are entirely attributed to cure shrinkage, while strains caused by a cooldown are a combination of thermal expansion effects and accumulated cure shrinkage from the temperature hold.

2.2.2.4 Asymmetric Beam Tests

To validate modulus and free strains obtained from BMB testing, the measured properties were shaped into numerical models, which were then used as inputs to predict experimental deflections of short asymmetric T800S/3900-2B beams. The prediction scheme followed the subsequent analytical solutions to compute the beams' out-of-plane deflections (Δ_b):[26,65,67]

$$\Delta_b = \frac{1 - Cos(L_b \kappa_b / 2)}{\kappa_b} \tag{2-13}$$

where L_b is the beam's length (101.6 mm), κ_b is the beam's curvature equal to:

$$\kappa_b = \frac{BA\varepsilon_0 - A^2\overline{Z_2}\varepsilon_0}{B^2 - AD} \tag{2-14}$$

and the remaining terms are calculated as follows:

$$\overline{Z_1} = n\, t_p/2 \tag{2-15}$$

$$\overline{Z_2} = -t_p/2 \tag{2-16}$$

$$t_2 = nt_p \tag{2-17}$$

$$A = E_1 t_p + E_c t_2 \tag{2-18}$$

$$B = E_1 t_p \overline{Z_1} + E_c t_2 \overline{Z_2} \tag{2-19}$$

$$D = E_1 \frac{t_p \overline{Z_1}^2 + t_p^3}{12} + E_c \frac{t_2 \overline{Z_2}^2 + t_2^3}{12} \tag{2-20}$$

$$d\varepsilon_0 = E_c t_2 \varepsilon_{free_c} / A \tag{2-21}$$

where n is the beam's number of ninety-degree plies, t_p is the thickness of a composite ply (0.191 mm)[36], and E_1 is the room-temperature zero-degree modulus of T800S/3900-2B cured according to manufacturer's recommended procedures (148 GPa).[36]

The setup utilized to manufacture short asymmetric T800S/3900-2B beams is shown in **Figure 2-17**. Standard prepreg lay-up and vacuum bagging procedures were used to fabricate the composite parts. The tool used for processing was a flat plate made of A2 tool steel. Before each test, the tool surface was cleaned with isopropyl alcohol (IPA) to remove residue from previous usages. Half of the tool was then treated with three coats of 710-NC using a lint-free wiping cloth, allowing fifteen minutes between coats as recommended on the product's datasheet.[41] The tool's other half was covered with one layer of fluorinated ethylene propylene (FEP) release film. Next, three laminates with ply dimensions of 25.4 mm (w) × 101.6 mm (l) were laid-up equally spaced across the width of each surface condition. Three layups were utilized for asymmetric beam fabrication: $[0/90_2]$, $[0/90_3]$, and $[0/90_4]$. The tool and composite laminates were then covered with another sheet of FEP release film and one layer of breather cloth. The system was then sealed in vacuum bagging, loaded into a convection oven, and subjected to one of the cure cycles shown in **Figure 2-18** with approximately 0.1 MPa of vacuum pressure applied throughout processing.

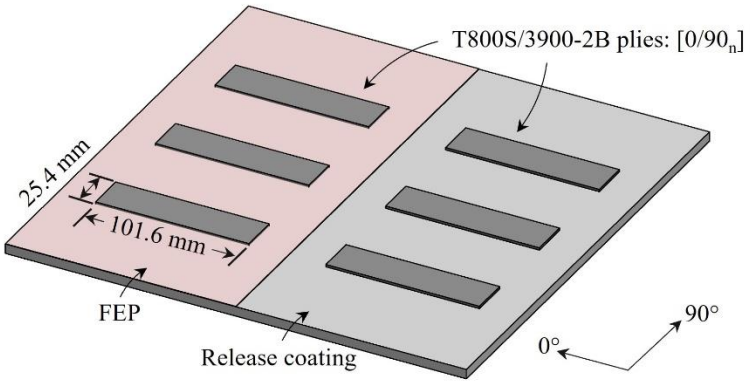

Figure 2-17. Layup configuration for asymmetric beam tests employed to validate T800S/3900-2B modulus and free strain measurements.

The 180-Hold cycle corresponded to the Manufacturer's Recommended Cure Cycle (MRCC) of heating to 180 °C at 2 °C/min, holding at 180 °C for 120 minutes, then cooling the system down. The 140/180-Hold and 160/180-Hold cycles consisted of heating to 140 °C or 160 °C at 2 °C/min, holding for 180 minutes, heating to 180 °C at 2 °C/min, holding at 180 °C for 120 minutes, then cooling the system down. The simulated degree of cure (DoC) and glass transition temperature (T_g) of the prepreg throughout these cycles are illustrated in the **Figure 2-18**.[63]

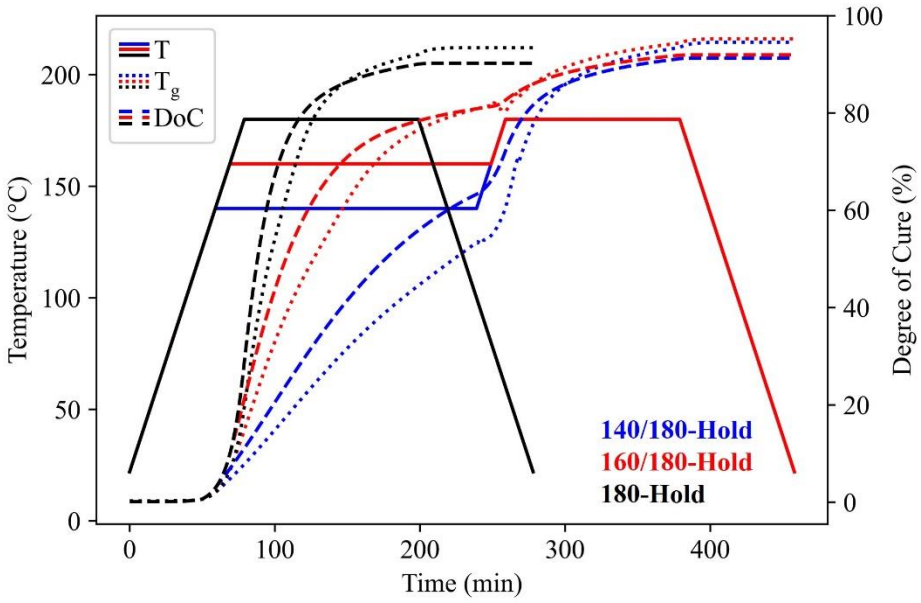

Figure 2-18. Cure cycles for asymmetric beam tests employed to validate T800S/3900-2B modulus and free strain measurements.

After a cure cycle was completed, the composite parts were demolded, placed on their longitudinal sides, and the maximum deflections were measured using a Keyence LJ-X8400 2D laser profiler. Two experiments were conducted for each layup, tool surface condition, and cure cycle to account for and evaluate the effects of material and process variabilities on beam deflections. Lastly, analytical predictions of asymmetric beam deflections were compared to experimental results to validate thermo-mechanical properties measured during the BMB testing campaign.

2.2.3 Results and Discussions

2.2.3.1 Morphology

Figure 2-19a-b display SEM micrographs of various regions within an uncured T800S/3900-2B laminate. The figures illustrate the prepreg's three primary constituents: carbon fibers, a base resin, and spherical thermoplastic particles.[1,36,68,69] The carbon fibers, commonly referred to as "T800S" throughout the aerospace industry, are comprised of polyacrylonitrile (PAN)-based filaments.[70] The uncured base resin exhibits a homogenous structure with an epoxy-derived thermoset component and a thermoplastic component that is miscible with the thermoset.[68] The thermoplastic particles could be made from amorphous polyamide.[1,63,69]

The micrographs of **Figure 2-19a-b** reveal that the majority of the base resin and thermoplastic particles are concentrated near the prepreg's surfaces, resulting in resin-poor intralayer regions in the uncured plies. Upon exposure to elevated temperatures and pressures (i.e., 180 °C and 0.7 MPa), the base resin's viscosity drops, facilitating its flow and permitting it to thoroughly wet-out the fibers.[26] Before gelation of the thermoset, the thermoplastic particles become rubbery and may deform under the applied pressure.[71] Upon gelation, polymer chains in the epoxy begin to form cross-links, unique VE changes occur, and the base resin's morphology transforms from homogeneous to phase-inverted or co-continuous.[68,72,73] This process yields a solid structure with intralayer regions containing a multi-phase base resin and carbon fibers, and interlayer regions filled with thermoplastic particles dispersed in base resin, as depicted in the micrographs of **Figure 2-19c-d**. Furthermore, **Figure 2-19c-d** reveals that after curing, the thermoplastic particles in the intralayer regions may exhibit a wide range of deformed spherical shapes, with diameters spanning from approximately 2 to 25 μm.

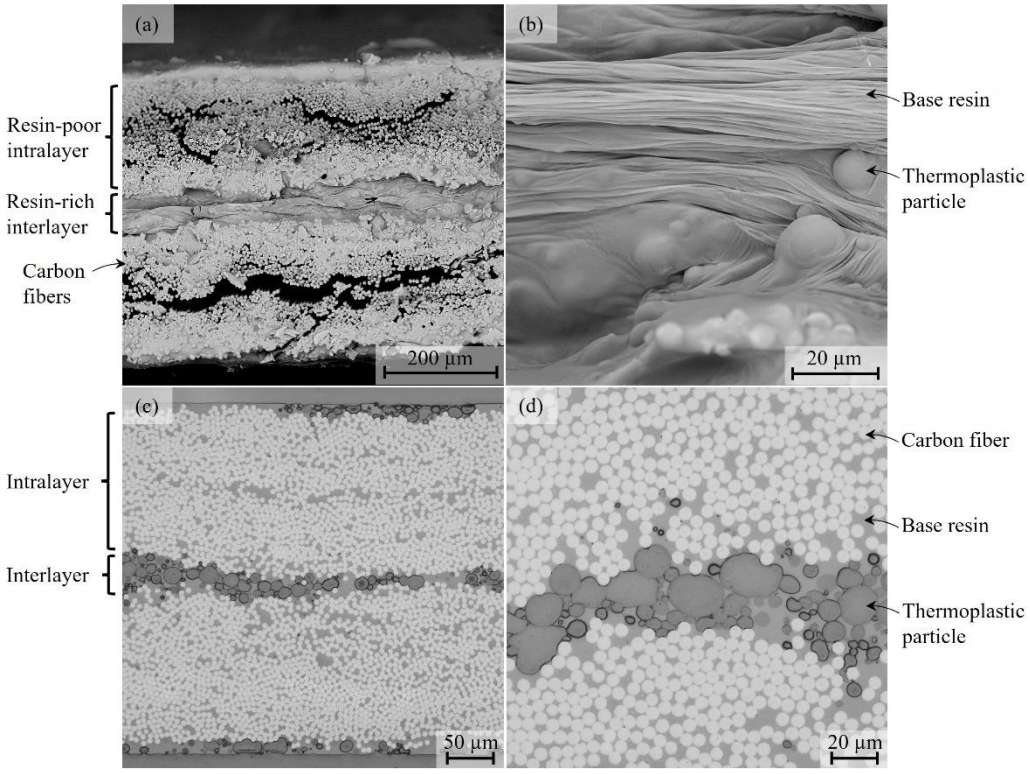

Figure 2-19. (a-b) SEM micrographs of an uncured T800S/3900-2B laminate and **(c-d)** light micrographs of a cured T800S/3900-2B laminate.

Figure 2-20 presents the tool-side surface morphology of T800S/3900-2B laminates cured according to the MRCC under five distinct autoclave pressures. Meanwhile, **Figure 2-21** provides a quantitative analysis of these surfaces, including the percentage of thermoset and thermoplastic components present and the root mean square roughness (Sq). The percent of thermoset and thermoplastic constituents on the surfaces was estimated using color segmentation in ImageJ processing software.[74] The values reported in **Figure 2-21** were obtained from an average of six laser scans for each cure pressure. The figures demonstrate that higher cure pressure applied to the laminates leads to greater particle deformation, increased thermoplastic surface fraction, and reduced base resin on the tool-side surface. Conversely, the increase in pressure can be observed to have minimal effects on the surface roughness of laminates. These phenomena may significantly impact tool-part interaction during processing and will be revisited in subsequent sections.

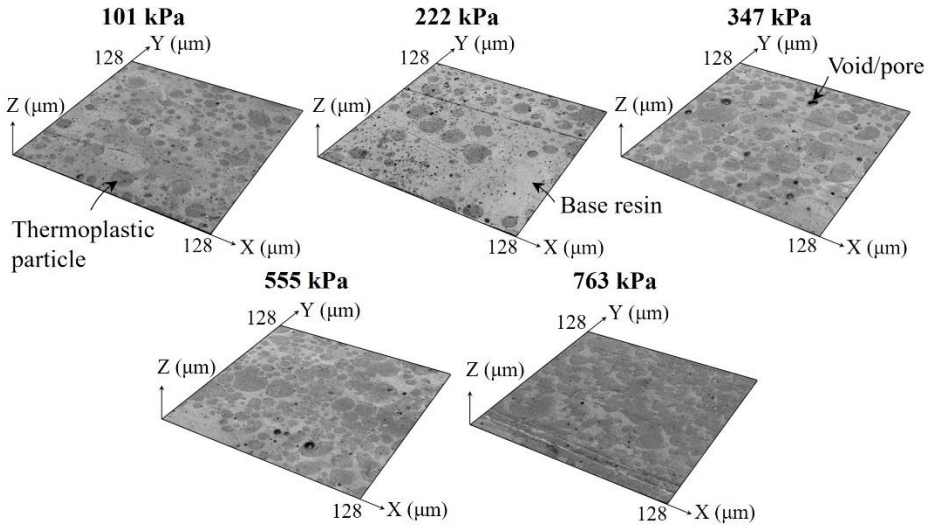

Figure 2-20. Micrographs of T800S/3900-2B laminate tool-side surfaces cured under different pressures.

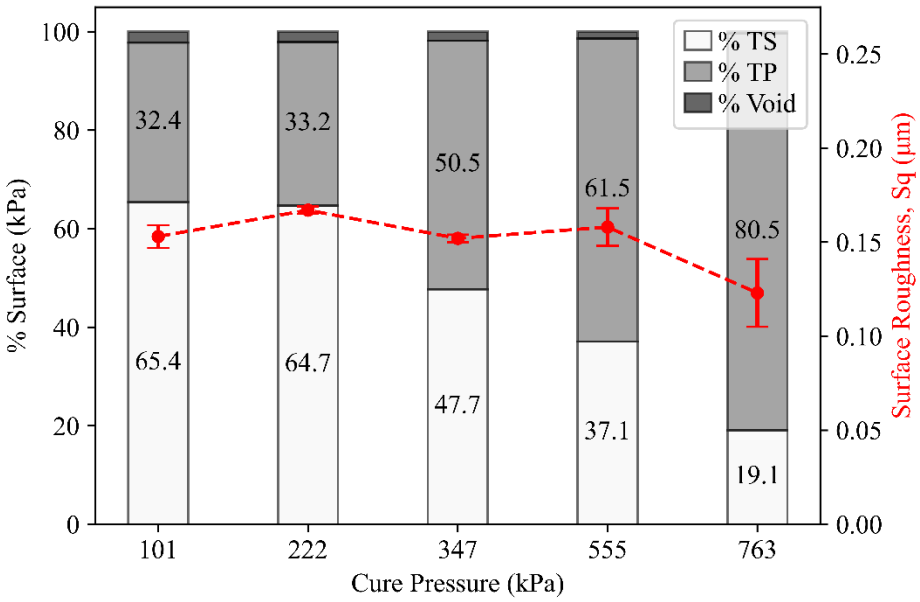

Figure 2-21. Tool-side surface morphology of T800S/3900-2B laminates cured under different autoclave pressures.

2.2.3.2 Post-processing Viscoelasticity

Figure 2-22 depicts the storage modulus, loss modulus, and tan(δ) of a 90% cured $[90]_{12}$ T800S/3900-2B beam across various temperatures and dynamic loading frequencies. At the onset of each temperature sweep (~100 °C), the storage and loss moduli measured approximately 10^4

and 10^2 MPa, respectively. As the temperature increased, storage moduli declined with similar behaviors due to thermoelastic effects, eventually reaching values of approximately 7.5×10^3 MPa at 150 °C. The increase in temperature simultaneously induced significant transitions in the loss modulus, first leading to frequency-dependent peaks in tan(δ) between -65 and -35 °C, then between 40 and 60 °C. These transitions indicate the presence of viscoelastic behaviors in cured T800S/3900-2B at low temperatures. While these effects may offer potential for mitigating residual stresses through relaxation and alleviating PIDs, further exploration of these phenomena lies beyond the scope of this study.

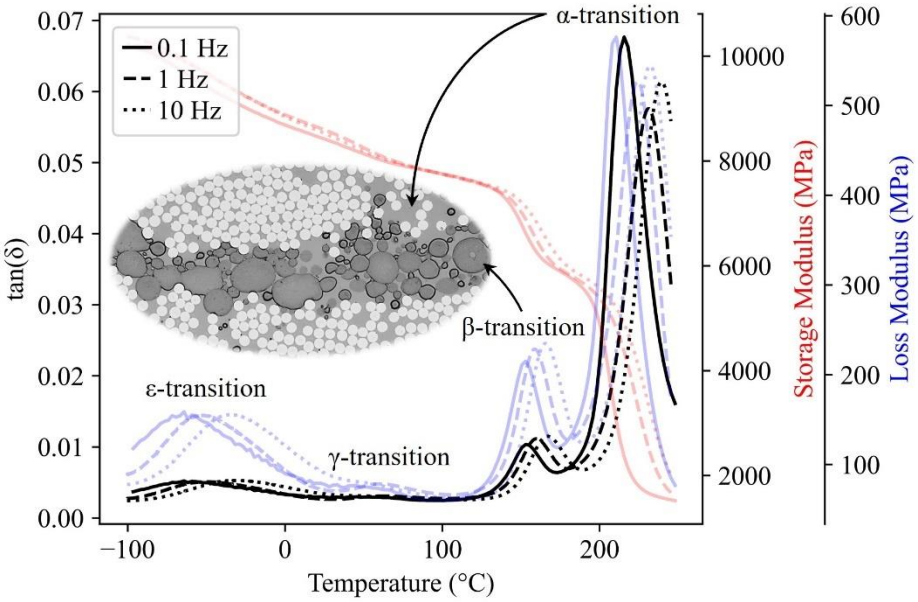

Figure 2-22. Viscoelastic behavior of 90% cured T800S/3900-2B at different temperatures and dynamic loading frequencies.

Upon reaching 150 °C, a shift in storage modulus behavior occurs, resulting in accelerated decays until approximately 6×10^3 MPa at 190 °C. Concurrently, there is a pronounced transition in loss modulus, with frequency-dependent tan(δ) peaks occurring between 150 and 165 °C. These phenomena represent the material surpassing the glass transition temperature of the thermoplastic particles, causing their transition into a rubbery state.[71] Subsequently, another transition in storage

and loss moduli initiated around 200 °C, with tan(δ) peaks occurring between 215 and 240 °C. This final conversion can be attributed to the glass transition of the base resin, signifying that all matrix constituents in the cured material have shifted into the rubbery state.

2.2.3.3 Modulus and Free Strains

Figure 2-23 – 2-31 show storage modulus and free strain evolutions in T800S/3900-2B prepreg throughout various cure cycles. Each plot presents results from two tests, with darker and lighter colors representing the first and second tests, respectively. The prepreg's simulated DoC and T_g throughout each cycle are also included in the plots.[63] Throughout all cycles, the modulus and free strain curves remain zeroed until gelation occurs, beyond which the BMB test method can measure the composite's thermo-mechanical response.[60] Following gelation in each cycle, the modulus sharply rises while free strains decrease before gradually reaching plateaus near the ends of the isothermal hold and vitrification periods. These thermo-mechanical developments indicate the composite's matrix underwent a cross-linking reaction starting at gelation. During this reaction, the formation of a cross-linked network increases the composite's bending stiffness, while a reduction in free space occupied by the polymer molecules results in chemical shrinkage and thus negative free strain.[3]

The modulus values at vitrification points, ranging from approximately 6 to 8 GPa, exhibit temperature-dependent variations, with the highest values observed at the lowest temperatures and vice versa. Free strain magnitudes at vitrification range from approximately -0.7 to -0.8% and show similar trends, with the largest absolute values occurring at lower temperatures. The greatest vitrified modulus values occur at the lowest temperatures, specifically below 140 – 150 °C, because the thermoplastic tougheners are in their glassy state (**Figure 2-22**). The composite's increased stiffness at lower temperatures also correlates to greater chemical strain. Conversely,

during isothermal periods above 140 – 150 °C, the tougheners transition to a rubbery (i.e., viscous) state, causing vitrified storage modulus and absolute free strain values to decline.

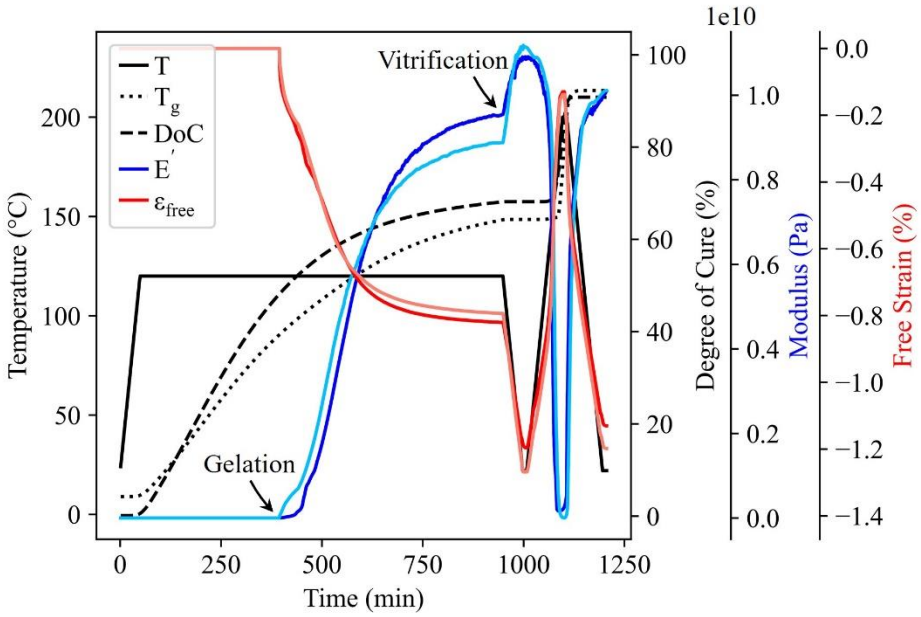

Figure 2-23. Development of dynamic storage modulus and free strains for T800S/3900-2B prepreg throughout a temperature cycle inducing gelation and vitrification at 120 °C.

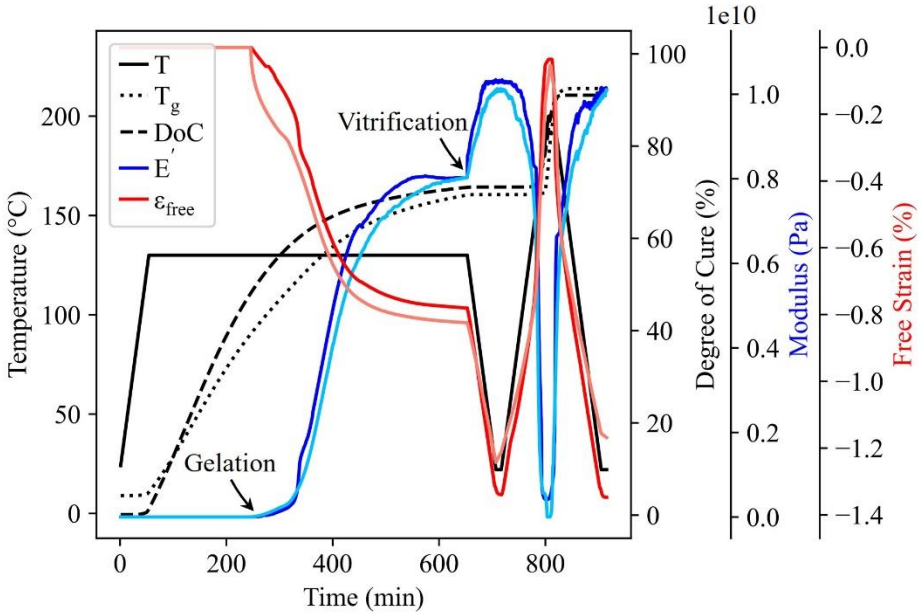

Figure 2-24. Development of dynamic storage modulus and free strains for T800S/3900-2B prepreg throughout a temperature cycle inducing gelation and vitrification at 130 °C.

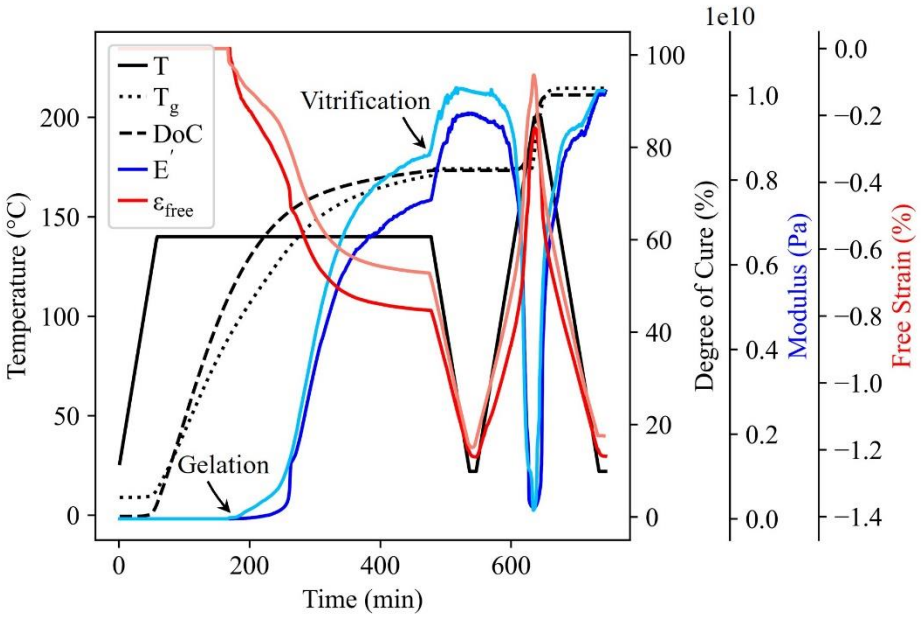

Figure 2-25. Development of dynamic storage modulus and free strains for T800S/3900-2B prepreg throughout a temperature cycle inducing gelation and vitrification at 140 °C.

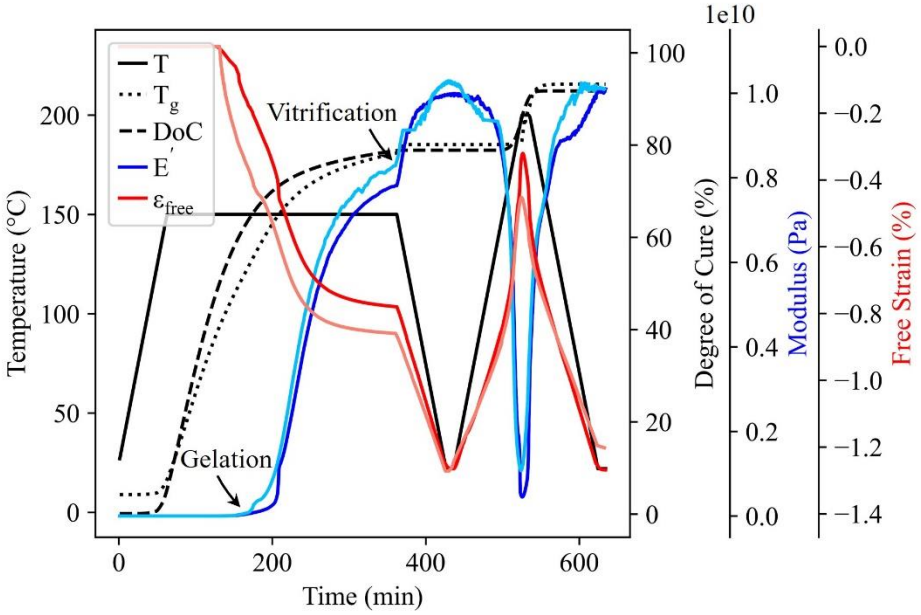

Figure 2-26. Development of dynamic storage modulus and free strains for T800S/3900-2B prepreg throughout a temperature cycle inducing gelation and vitrification at 150 °C.

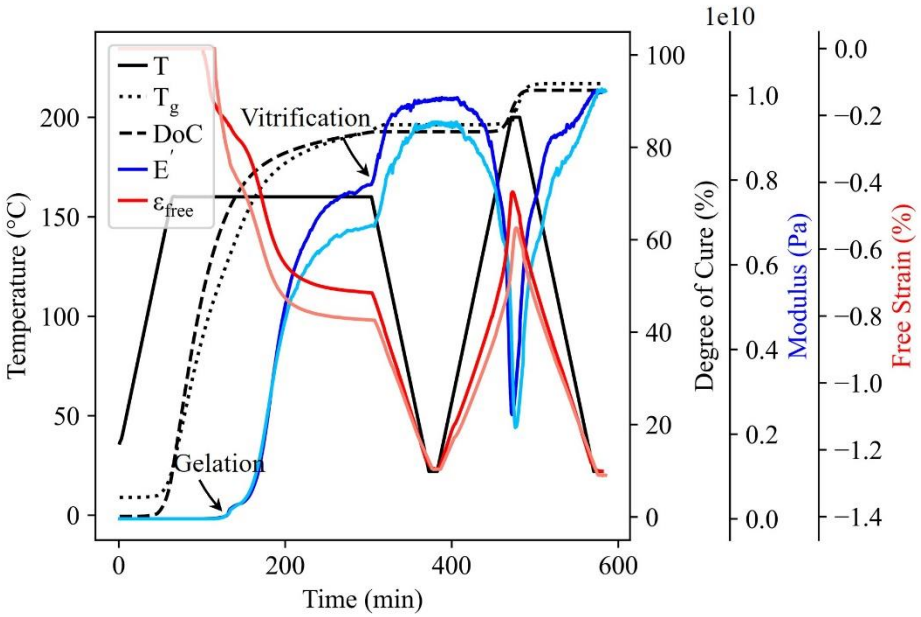

Figure 2-27. Development of dynamic storage modulus and free strains for T800S/3900-2B prepreg throughout a temperature cycle inducing gelation and vitrification at 160 °C.

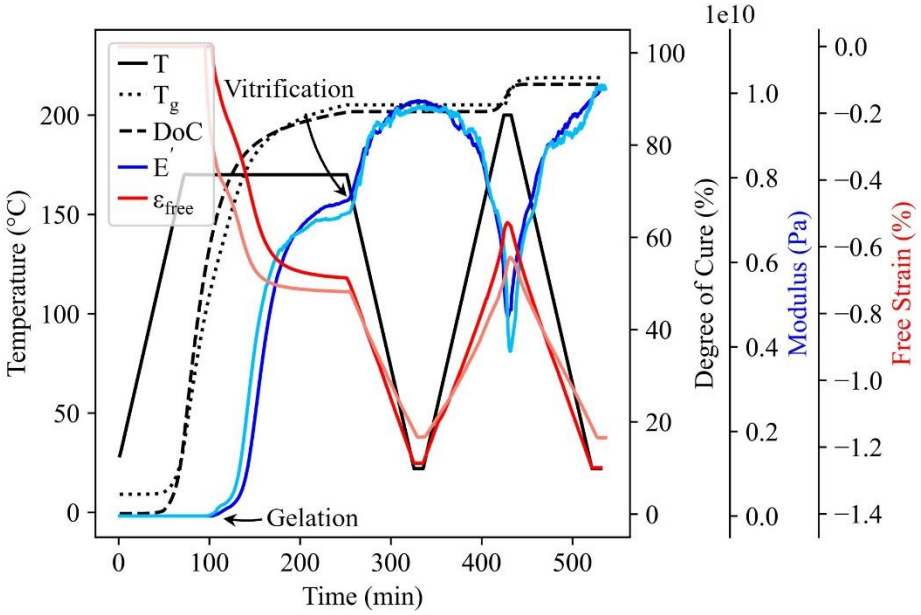

Figure 2-28. Development of dynamic storage modulus and free strains for T800S/3900-2B prepreg throughout a temperature cycle inducing gelation and vitrification at 170 °C.

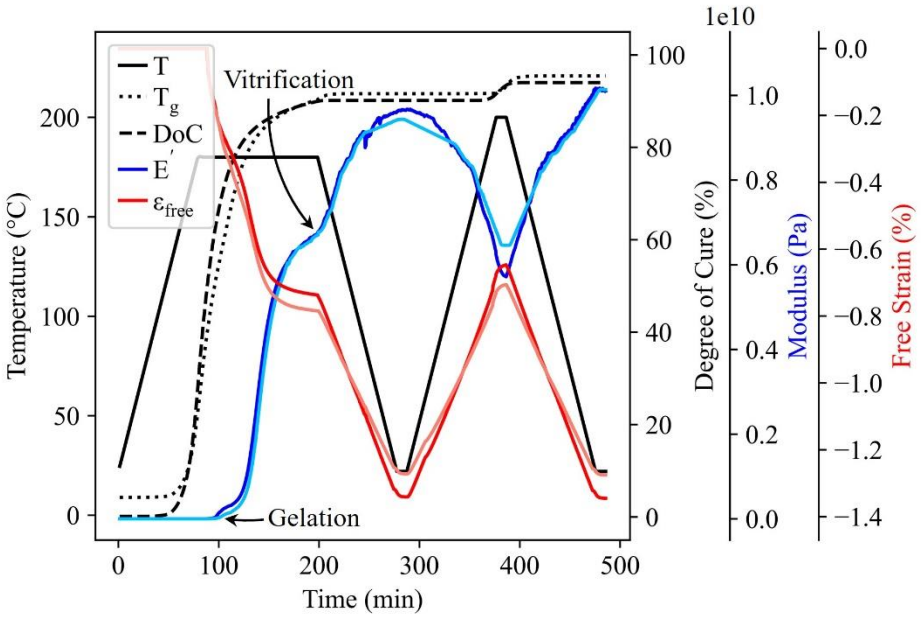

Figure 2-29. Development of dynamic storage modulus and free strains for T800S/3900-2B prepreg throughout a temperature cycle inducing gelation and vitrification at 180 °C.

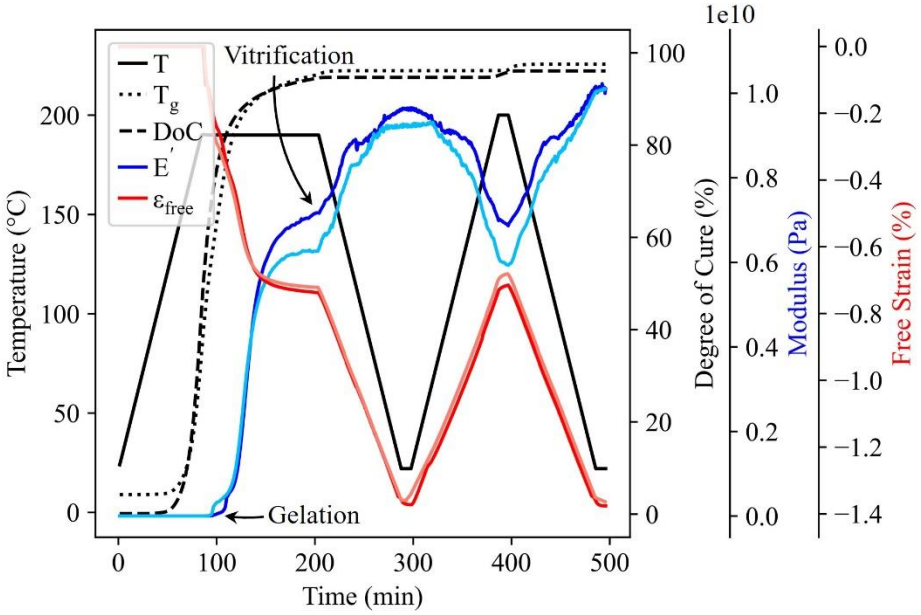

Figure 2-30. Development of dynamic storage modulus and free strains for T800S/3900-2B prepreg throughout a temperature cycle inducing gelation and vitrification at 190 °C.

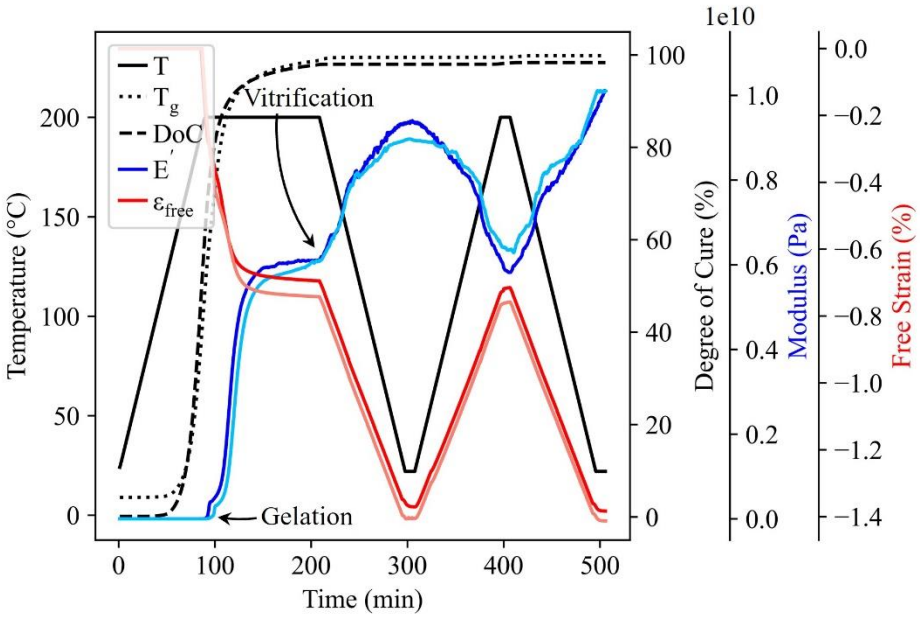

Figure 2-31. Development of dynamic storage modulus and free strains for T800S/3900-2B prepreg throughout a temperature cycle inducing gelation and vitrification at 200 °C.

During the initial cooldown phase, storage moduli sharply rise due to thermoelastic effects, while free strains drop linearly from thermal contraction.[75] In cycles featuring high isothermal hold temperatures, moduli exhibit complex behaviors during cooldown, with secondary transitions around 140 to 150 °C, indicating the thermoplastic tougheners are reverting to their glassy state. Conversely, cooldowns from temperatures below 150 °C exhibit relatively uniform contractions since the thermoplastics remained glassy throughout the prior isothermal hold period.

Upon reaching room temperature, storage modulus values stabilize within a range of approximately 9 – 11 GPa, remaining inversely correlated with the temperature at which vitrification occurred in the composite. Free strain values span from approximately -1.2 to -1.4%, with the largest absolute values stemming from the most significant temperature changes. Subsequently, the second heating phase induces reductions in storage moduli, with more pronounced drops observed in cycles with lower initial vitrification temperatures, as the processing temperature approaches or exceeds T_g and results in devitrification. The second heat-up also causes

a reduction in absolute free strains due to thermal expansion and some cure progression in cycles with a low first isothermal hold temperature. During this phase, the thermoplastic tougheners regain their rubbery characteristics when processing temperatures exceed 150 °C. Lastly, during the final cooldown period, modulus values increase to approximately 10 GPa due to thermoelastic effects, with all cycles demonstrating secondary transition behaviors upon surpassing the glass transition of the thermoplastics. Free strains evolve linearly to -1.2 to -1.4% due to another induced thermal contraction in the composite material.

Figure 2-32 illustrates the unique evolutions of T800S/3900-2B's storage modulus across the initial heating, isothermal hold, and cooling phases of the BMB cycles. In the graph, the modulus is shown against the difference between the processing temperature and the composite's instantaneous glass transition temperature. Each line in the plot is colored to denote the isothermal hold and vitrification temperature of the material, with two tests reported for each cycle. The curves demonstrate that upon gelation, moduli initially exhibit exponential-like increases with relatively rapid growth rates, which gradually slow down as the composite approaches vitrification. The absolute magnitudes of moduli at vitrification exhibit strong inverse correlations with the processing temperature. Following vitrification, moduli continue to progress with parabolic-like behaviors for low processing temperatures and exhibit additional secondary transitions in the higher-temperature tests.

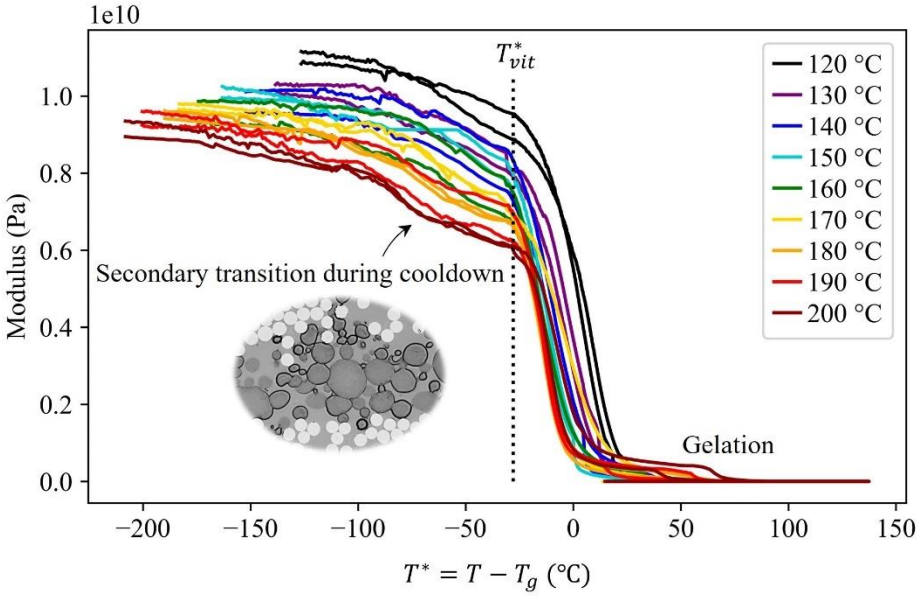

Figure 2-32. Evolution of T800S/3900-2B's dynamic storage modulus while curing at and cooling from different temperatures.

The behaviors of T800S/3900-2B's storage modulus illustrated in **Figure 2-32** can be mathematically described using a piece-wise function defined across three zones in $T - T_g$ space:

$$E'(T^*) = \begin{bmatrix} E'_{min} & \alpha < \alpha_{gel} \\ d + \dfrac{a-d}{\left(1 + \left(\dfrac{T^* - T^*_{vit}}{c}\right)^b\right)^g} & T^* \geq T^*_{vit} \\ jT^{*2} + kT^* + m & T^* < T^*_{vit} \end{bmatrix} \quad (2\text{-}22)$$

where α is the composite's instantaneous degree of cure, α_{gel} is the degree of cure at gelation, T^* is the difference between the processing temperature and the composite's instantaneous glass transition temperature, T^*_{vit} is the difference between the processing temperature and the composite's glass transition temperature at vitrification, and E'_{min} is the composite's storage modulus before gelation. In the initial segment of (2-22), the modulus is held constant until the material's gelation point ($\alpha = \alpha_{gel} = 0.48$), which was determined from DMA tests. Following

gelation, the modulus can be modeled as a five-parameter asymmetric logistic[76], while a second-order polynomial is employed to describe the cooldown behavior.

During the interval between gelation and vitrification, the primary temperature-dependent differences in modulus evolutions are in the maximum values and the horizontal positioning of the transition regions (**Figure 2-32**). Temperature dependency in the cooldown phase is evident in the magnitudes and eccentricities of the parabolas. To accommodate these temperature dependencies in the model, parameters a, c, j, k, and m can be assumed to follow second-order relationships with the processing temperature:

$$a = a_1 T^2 + a_2 T + a_3 \tag{2-23}$$

$$c = c_1 T^2 + c_2 T + c_3 \tag{2-24}$$

$$j = j_1 T_{vit}^2 + j_2 T_{vit} + j_3 \tag{2-25}$$

$$k = k_1 T_{vit}^2 + k_2 T_{vit} + k_3 \tag{2-26}$$

$$m = m_1 T_{vit}^2 + m_2 T_{vit} + m_3 \tag{2-27}$$

where T is the temperature, and all other parameters are to be determined. By employing non-linear least squares, (2-22) – (2-27) can be fitted to the data presented in **Figure 2-32**, optimal parameters can be determined (**Table 2-3**) and a mathematical model describing T800S/3900-2B's modulus behavior during processing can be generated. **Figure 2-33** superposes the fitted model and testing data, with each datapoint representing the average values obtained from two BMB tests at each temperature. The model yields highly accurate predictions of the test data, with a root mean squared error (RMSE) of 2.8%.

Table 2-3. Parameters for modeling the evolution of T800S/3900-2B's dynamic storage modulus during cure.

Parameter	Value
E'_{min}	1000 Pa
α_{gel}	0.48
T^*_{vit}	-28 °C
a_1, a_2, a_3	1.91×10^5, -9.50×10^7, 1.76×10^{10}
b	2.59×10^0
c_1, c_2, c_3	5.66×10^{-3}, -1.98×10^0, 1.96×10^2
d	2.77×10^4
g	1.79×10^0
j_1, j_2, j_3	1.66×10^1, -4.03×10^3, 6.10×10^4
k_1, k_2, k_3	3.54×10^3, -1.02×10^6, 2.40×10^7
m_1, m_2, m_3	2.32×10^5, -1.08×10^8, 1.73×10^{10}

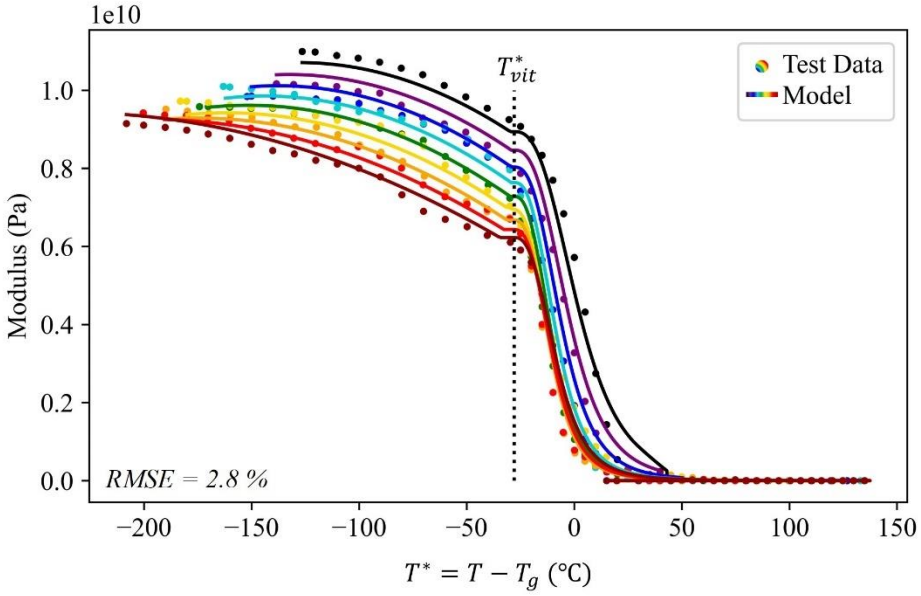

Figure 2-33. Comparison between developed model and test data for T800S/3900-2B's storage modulus evolution throughout cure.

Figure 2-34 depicts free strain progressions in T800S/3900-2B across the initial heat-up, isothermal hold, and cooldown phases of the BMB cycles. In the graph, strains are plotted against the difference between the processing temperature and the composite's instantaneous glass transition temperature. **Figure 2-35** provides an alternative view of free strain evolutions focused solely on cure shrinkage behaviors versus the composite's degree of cure. Each line in **Figure 2-34**

and **Figure 2-35** is colored according to an isothermal hold and vitrification temperature, with two tests reported for each cycle.

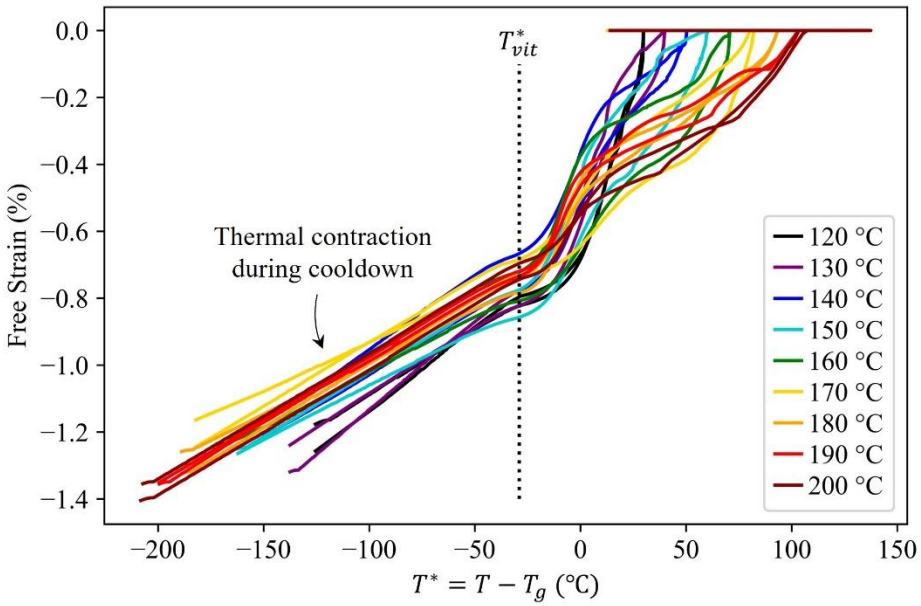

Figure 2-34. Evolution of T800S/3900-2B's cure shrinkage- and thermal-induced free strains while curing at different temperatures.

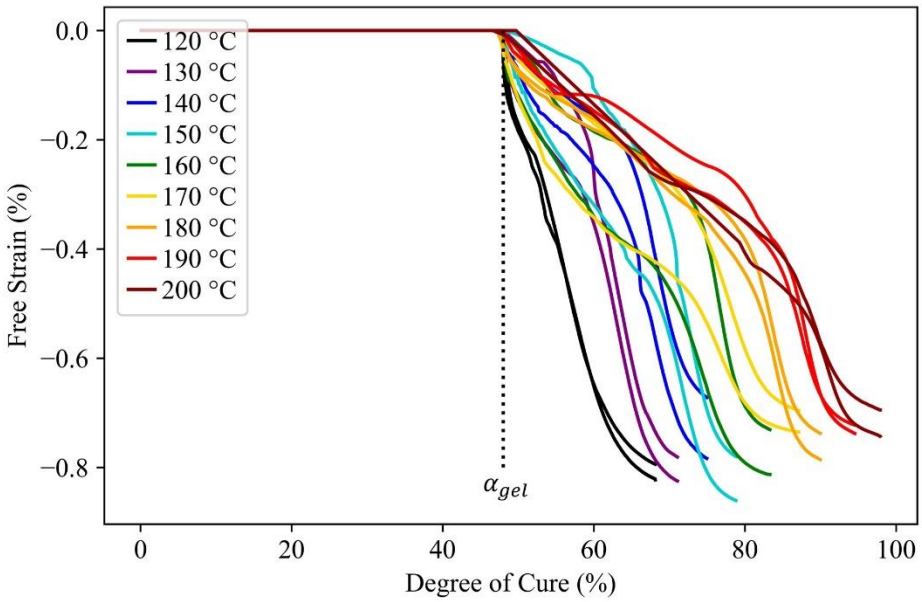

Figure 2-35. Evolution of T800S/3900-2B's cure shrinkage-induced free strains while curing at different temperatures.

Upon gelation, free strains display complex patterns, with initially rapid exponential-like behaviors that gradually decelerate near vitrification. Throughout the curing process, the absolute magnitudes of free strains also demonstrate to be generally correlated with the processing temperature. These material behaviors can be mathematically described using the following function in $T - T_g$ space:

$$d\varepsilon_{free}(T^*) = d\varepsilon_{free,cs}(T^*) + d\varepsilon_{free,th}(T^*) \tag{2-28}$$

where $d\varepsilon_{free}$ is the derivative of free strains, $d\varepsilon_{free,cs}$ is the derivative of cure shrinkage-induced free strains, $d\varepsilon_{free,th}$ is the derivative of thermal-induced free strains, and where:

$$d\varepsilon_{free,cs}(T^*) = \begin{bmatrix} 0 & \alpha < \alpha_{gel} \\ v\left(ne^{-\frac{(T^*-p)^2}{2q^2}} + se^{r(T^*+T)}\right) & \alpha > \alpha_{gel} \end{bmatrix} \tag{2-29}$$

$$d\varepsilon_{free,th}(T^*) = \begin{bmatrix} CTE_{glassy} & T < T_g \\ CTE_{rubbery} & T > T_g \end{bmatrix} \tag{2-30}$$

where CTE_{glassy} and $CTE_{rubbery}$ are the glassy and rubbery coefficients of thermal expansion and n, p, q, r, s, and v are variables to be optimized. In (2-29), the derivative of cure shrinkage is assumed to be negligible until gelation occurs ($\alpha = \alpha_{gel} = 0.48$), then follow a summation of Gaussian and exponential behavior. During the shrinkage process, the primary temperature-dependent differences between curves include the rapidity of decays after gelation and the horizontal positioning of the transition regions in $T - T_g$ space (**Figure 2-34**). To integrate these temperature dependencies into the model, parameters n, q, and r are assumed constant, while p, s, and v are assumed to adhere to the following relationships with the processing temperature:

$$p = p_1 T + p_2 \tag{2-31}$$

$$s = s_1 T^2 + s_2 T + s_3 \tag{2-32}$$

$$v = v_1 T^{v_2} \tag{2-33}$$

where T is the processing temperature and all other parameters are to be determined. By employing non-linear least squares, optimal parameters in (2-29) – (2-33) can be solved for (**Table 2-4**) and a mathematical model describing T800S/3900-2B's free strain behavior during processing can be generated. Note that CTE_{glassy} was obtained directly from BMB testing data, while $CTE_{rubbery}$ was assumed to equal three times the glassy value.[5] **Figure 2-36** and **Figure 2-37** superpose the fitted model and testing data in different spaces, with each datapoint representing the average values obtained from two BMB tests at each temperature. The model yields accurate predictions with an RMSE of 0.06 strain %.

Table 2-4. Parameters and values for modeling the evolution of T800S/3900-2B's cure shrinkage during cure.

Parameter	**Value**
α_{gel}	0.48
n	1.30×10^{-4}
p_1, p_2	-3.13×10^{-1}, 5.25×10^{1}
q	1.10×10^{1}
r	2.50×10^{-2}
s_1, s_2, s_3	1.27×10^{-10}, -5.06×10^{-8}, 5.10×10^{-6}
v_1, v_2	3.33×10^{3}, -1.57×10^{0}
CTE_{glassy}	38×10^{-6}
$CTE_{rubbery}$	114×10^{-6}

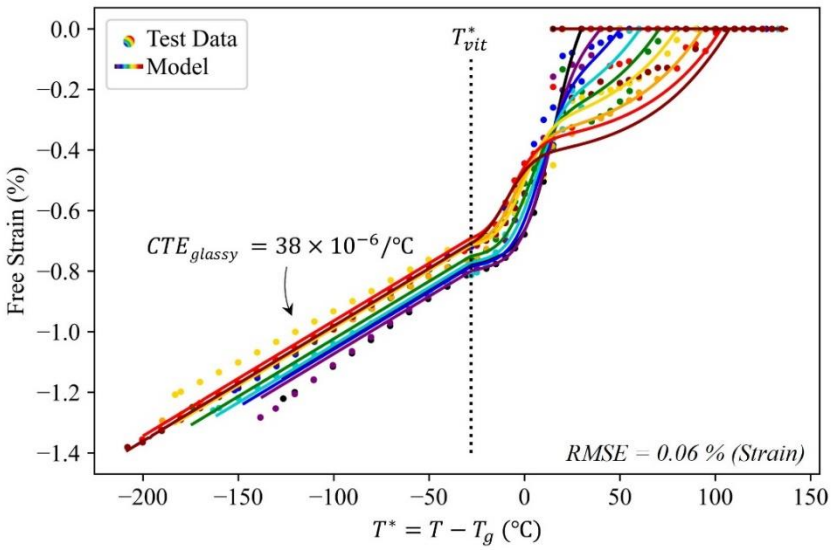

Figure 2-36. Comparison between developed model and test data for T800S/3900-2B's free strain evolution in $T - T_g$ space.

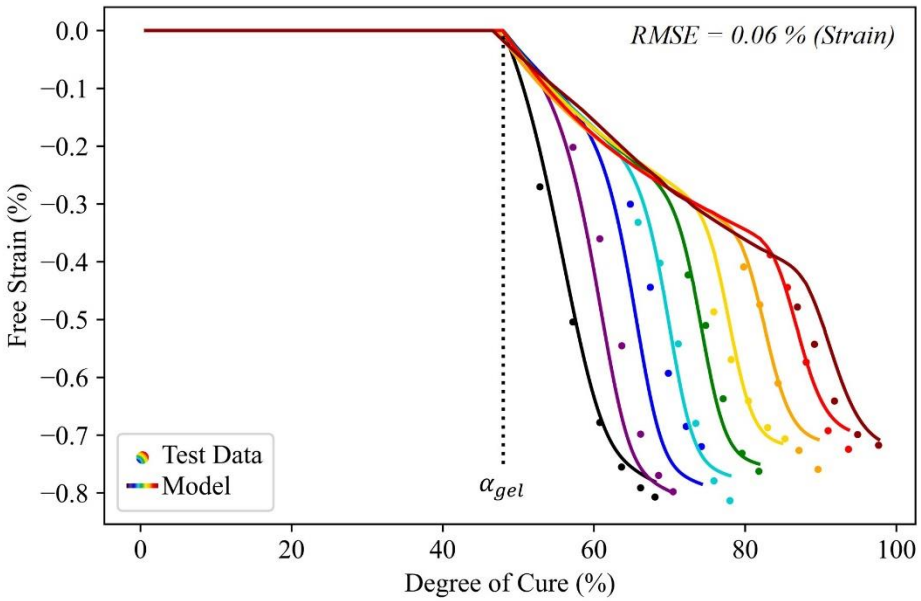

Figure 2-37. Comparison between developed model and test data for T800S/3900-2B's cure shrinkage-induced free strain evolution.

2.2.3.4 Model Validation

Figure 2-38 – 2-40 compare experimental deflections of $[0/90_n]$ asymmetric beams to numerical predictions derived from modulus and free strain models. The lighter bars represent the average of two experiments for each cycle and layup, while the darker bars are the corresponding

numerical predictions. It is important to note that predictions were computed using the CHILE model, which is an approximate approach.[64] Error bars in the plots represent standard deviations within each measurement set. Overall, the experiments and predictions correspond closely, with less than 10% error observed for all layups and cure cycles, except for one instance. In essence, the properties and models generated through BMB testing offered agreeable predictions of trends in residual stresses and PIDs, rendering them adequte for subsequent analyses.

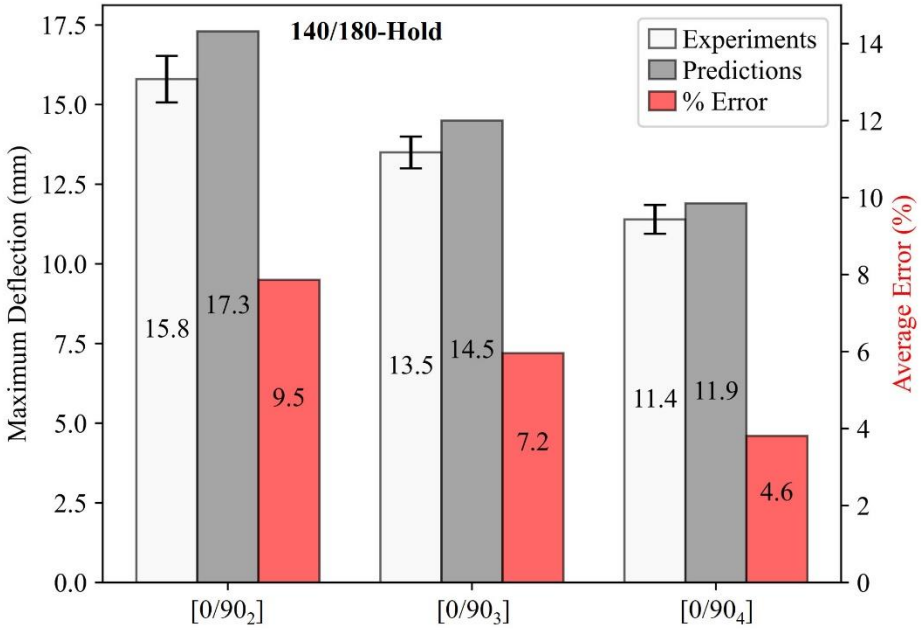

Figure 2-38. Comparison between experimental and predicted deflections of asymmetric T800S/3900-2B beams for the 140/180-Hold validation cure cycle.

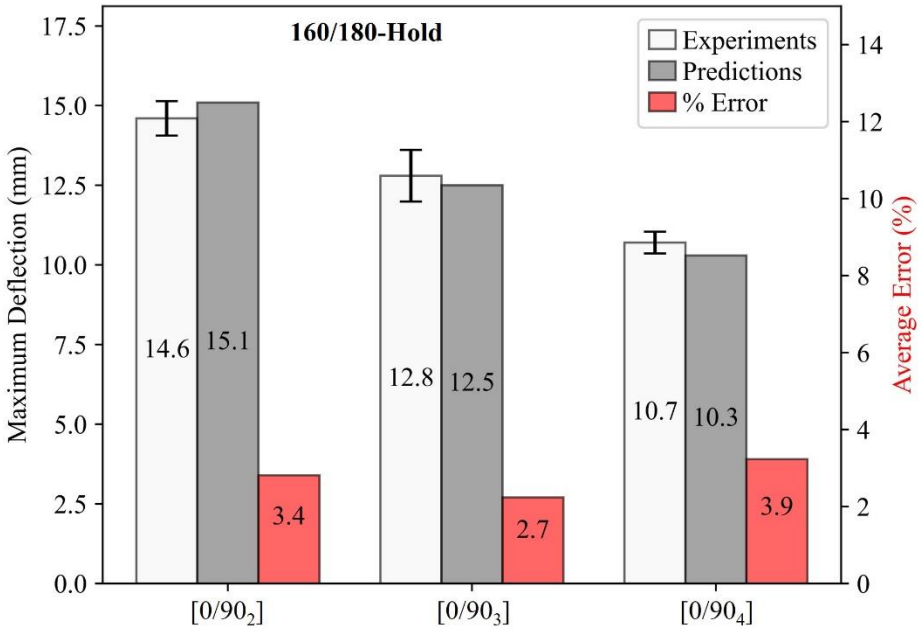

Figure 2-39. Comparison between experimental and predicted deflections of asymmetric T800S/3900-2B beams for the 160/180-Hold validation cure cycle.

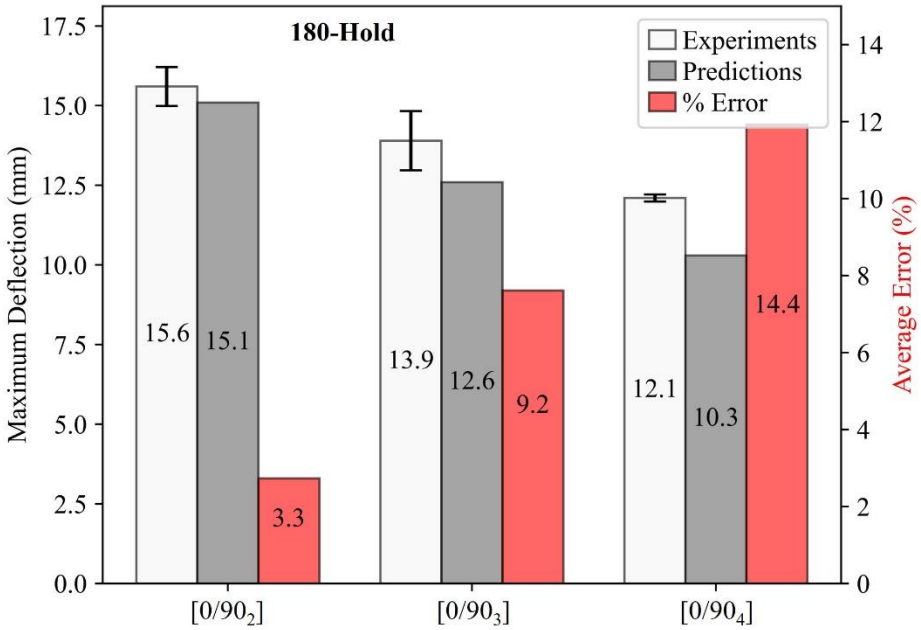

Figure 2-40. Comparison between experimental and predicted deflections of asymmetric T800S/3900-2B beams for the 180-Hold validation cure cycle.

2.3 TOOL-PART INTERACTION

2.3.1 Background

During autoclave processing, elevated pressures and temperatures promote interfacial physicochemical bonds and free strain mismatches between the tool and part. When coupled, these phenomena create a shear interaction at the tool-part interface that transfers stresses through the release coating and into the tool-adjacent plies. These interactions and their contributions to residual stresses and PIDs are surrounded by high levels of uncertainty for advanced aerospace composites.

Several studies have explored tool-part interactions during composites processing.[6–8,14,15,21–25,77–79] Twigg et al. used an instrumented tool setup to measure in-plane strains and deduce tool-part stress levels using closed-form equations.[25] They discovered early-stage sliding behavior between the tool and part, with constant shear stress at about 10 kPa, regardless of the tool surface condition or autoclave pressure. This suggested the potential of stress development even prior to resin gelation due to fiber bed interactions. Using a similar approach, Ding et al. substantiated the existence of these minor pre-gelation sliding stresses.[22] However, it is important to note that although early-stage stresses may develop, due to the composite's negligible shear modulus prior to gelation, most of these stresses would be effectively neutralized through interply slippage and thus not significantly contribute to PIDs.[5–7]

As the composite's modulus evolved in Twigg et al.'s study, the tool and part exhibited sticking behavior and a sharp rise in stress levels due to the formation of interfacial adhesive bonds.[7] Throughout the remainder of the cure cycle, tool-part strain mismatches directly increased stress levels until a shear stress limit, called the debonding stress, was reached. After debonding and a sharp drop in interfacial stresses, a sliding regime was observed, where shear

stresses remained relatively constant. These post-gelation stresses, unlike early-stage sliding behaviors, cannot be as easily mitigated through ply slippage and become locked-in due to the evolution of the composite's mechanical properties and phase transformation upon vitrification.

Instead of relying on strain measurements as an indirect approach, some researchers have developed methods to directly characterize tool-part interactions using "pull-out" methods.[23,24,77,80,81] These methods involve sandwiching a tool between composite strips and pulling the tool to quantify interfacial stresses. Past studies have used these pull-out methods to investigate the effects of parameters such as displacement rate, layup, tool surface condition, degree of cure, heating rate, and compaction pressure. Consequently, these studies have highlighted the sensitivity of tool-part interactions to such factors.

Despite these valuable contributions, uncertainties remain in understanding tool-part interaction for the current generation of interply-toughened aerospace composites. Much of the published literature relates to previous-generation material systems without interlayer toughening technology such as Hexcel 8552 prepreg.[35] Additionally, these studies have not investigated the impact of several industry-relevant processing variabilities on tool-part stress developments due to limitations in measurement techniques. This knowledge gap results in oversimplified representations of tool-part interaction, leading to inaccurate predictions of PIDs and, consequently, hindered optimization efforts in composites manufacturing.

The primary aim of this section is to investigate the impacts of processing variabilities and the inherent mechanisms of tool-part interaction in T800S/3900-2B. Rather than seeking direct comparisons with previous-generation aerospace materials, the aim is to establish a comprehensive foundation for understanding the complex phenomena involved in manufacturing current-generation aerospace materials.

2.3.2 Materials and Methods

Figure 2-41 and **Figure 2-42** show a custom DMA fixture built to measure tool-part interfacial stresses during processing. The novel setup was constructed using the shear sandwich clamp in a TA Instruments DMA 850. Custom U- and C-shaped tools, made from A2 tool steel with an ISO 1302 surface roughness grade of N3, were integrated into the system to cover the moveable and stationary clamps during testing.[50] The U-shaped tool was reused throughout the entire testing campaign, while two new C-shaped tools were prepared for each DMA test utilizing a manual shear/brake combination machine.

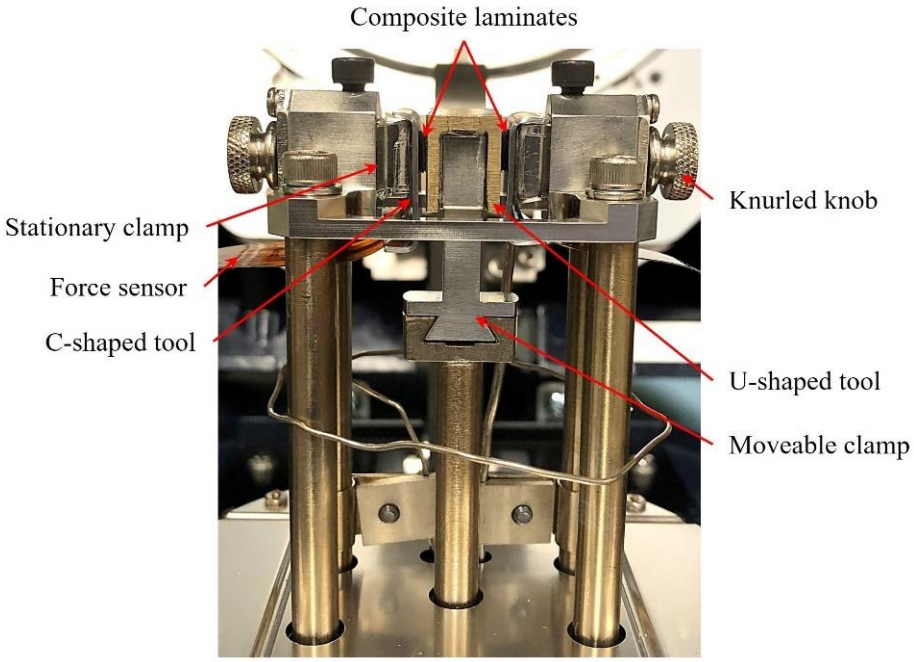

Figure 2-41. Custom DMA shear test setup used to measure tool-part interfacial stress developments during composites processing cycles.

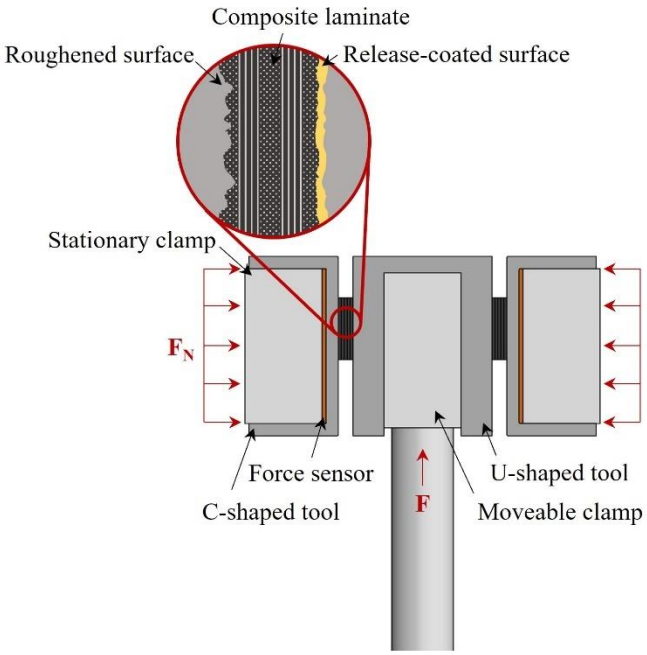

Figure 2-42. Schematic of custom DMA shear test setup used to measure tool-part interfacial stress developments during composites processing cycles.

Sample preparation for each DMA test involved creating two laminates from ten plies of T800S/3900-2B prepreg. First, each ply was cut into nominal dimensions of 4 mm (w) × 4 mm (l) using an X-ACTO knife. The plies were then stacked to create two cross-ply laminates with five plies each. For all tests, except those used to study laminate layup effects, a stacking sequence of $[90/0/\overline{90}]_s$ was utilized. Next, both laminates were simultaneously hot-debulked for 30 minutes at 60 °C on a hotplate under approximately 0.7 MPa (~7 atm) of applied pressure through caul plates. The hot debulk stage was utilized to prevent excessive compaction during DMA testing, which could otherwise have detrimental effects on the curing pressure levels. Once the laminates were debulked, they were then cooled down to room temperature before DMA testing.

Before each test, the U-shaped tool was cleaned with Frekote PMC mold cleaner[48] and a lint-free cloth to remove any surface residues. The outside surfaces on the U-shaped tool were then treated with Frekote 710-NC or covered with FEP release film. For all tests, except those explicitly examining tool surface condition effects, three coats of Frekote 710-NC were applied. Next, the

outer surfaces of the C-shapes were roughened using 80-grit aluminum oxide sandpaper for two minutes before cleaning with isopropyl alcohol (IPA). Afterward, the debulked laminates were sandwiched between U- and C-shaped tools in the DMA (**Figure 2-41** and **Figure 2-42**). Finally, compaction pressure was applied to the laminates using the knurled knobs and continuously monitored throughout each test by placing FlexiForce^{TM} HT201 piezoresistive force sensors between each stationary clamp and C-shaped tool.[82] For all tests, except those examining cure pressure effects, a pressure of 763 kPa was used.

Once the laminates were loaded into the DMA shear fixture, the system was subjected to a temperature cycle. The MRCC was utilized for all tests except those specifically examining cure temperature effects.[36] The MRCC consists of heating to 180 °C at 2 °C/min and holding for 120 minutes before cooling down. During the heat-up step, the laminates start to cure and form strong primary and mechanical bonds with the abraded C-shaped tool surfaces. The composites thus remained bonded to the C-shapes throughout the test. Meanwhile, the laminates form weaker primary and secondary bonds with the U-shaped tool since its surfaces were covered with release coating or FEP film. The laminates were held stationary during cure until they reached their gel points, where major PID-contributing tool-part stresses begin to evolve and interlaminar bonds have formed.[24,25]

Once the laminates were sufficiently gelled, an upwards force was applied from the DMA drive motor to generate vertical motion in the U-shaped tool. This motion created an in-plane displacement mismatch between the tool and part with a constant rate. For all tests, except those examining rate effects, a constant displacement rate of 0.05 mm/min was selected to be consistent with previous "pull-out" experiments.[24,77] It is worth noting that throughout the development of the shear technique, faster rates were also considered but dismissed as they did not represent

displacements and thus tool-part behaviors in manufacturing settings. Moreover, the rate of 0.05 mm/min was chosen to ensure that it fell within the allowable range of motion for the DMA setup, considering the specific sample geometry and clamp size. By applying motion at this rate from the composite's gelation point, the tool and part were ensured to maintain contact during the test.

As stated previously, standard process conditions for the DMA shear test included a tool surface condition of 3 Frekote 710-NC release coats, cure pressure of 763 kPa, laminate layup of $[90/0/\overline{90}]_s$, cure temperature of 180 °C, and displacement rate of 0.05 mm/min. In this section, the effects of process variables were examined by altering one condition while keeping others unchanged, as listed in **Table 2-5**. Two tests were performed for each variable subset, except for the evaluation of release coating aging effects, to assess test repeatability and account for material and process variabilities during the analyses.

Table 2-5. Process variables investigated using the custom DMA shear test.

Processing Variable	Values Investigated
Tool Surface Condition	FEP, 1 – 4 710-NC Release Coats, B-15/710-NC Release Coating Aged 1 – 6 Cycles
Cure Pressure	101, 222, 347, 555, 763 kPa
Laminate Layup	$[90/0/\overline{90}]_s$, $[0/90/\overline{0}]_s$, $[45/\text{-}45/\overline{45}]_s$
Cure Temperature	180, 160, 140 °C
Tool-Part Displacement Rate	0.025, 0.050, 0.075 mm/min

2.3.3 Results and Discussions

2.3.3.1 Manufacturer's Recommended Cure Cycle (MRCC)

Figure 2-43 shows the development of tool-part interfacial stresses ($\tau_{tool-part}$) during curing of $[90/0/\overline{90}]_s$ laminates, with tool surfaces covered with three layers of Frekote 710-NC, as recommended on the datasheet.[41] The temperature profile (T), simulated glass transition temperature of thermoset base resin ($T_{g,ts}$), glass transition temperature of thermoplastic particles

($T_{g,tp}$), and simulated degree of cure (DoC) are also superposed in **Figure 2-43**.[63] During the MRCC trial, the laminates were subjected to a compaction pressure of 763 kPa before heating, and the force sensors continuously tracked pressure variations throughout the test. Force sensor data revealed that the pressure remained within a 10 kPa range of the initial value throughout the entire cycle. Minimal pressure changes were similarly observed in all other DMA shear tests conducted in this study. Therefore, pressure is omitted from graphs to enhance clarity of other plotted variables. These negligible pressure changes may be attributed to a balance of forces among various factors: minor ply compaction (considering the previous hot debulking) to slightly reduce the pressure, through-thickness cure shrinkage in the composite which may also subtly decrease the pressure, and thermal expansion of the metallic fixtures potentially causing modest increases in pressure. Together, these factors produce a near-zero pressure change during the DMA shear tests.

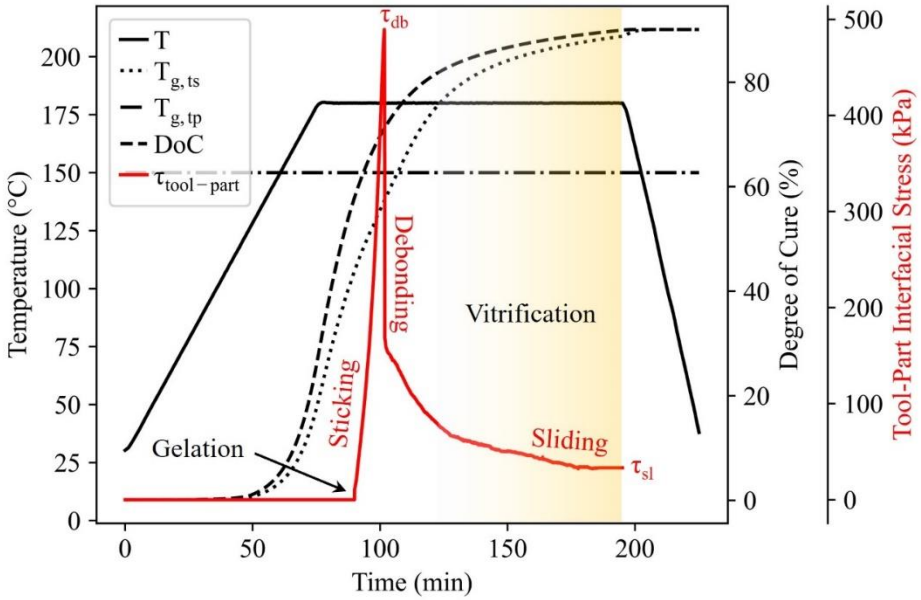

Figure 2-43. Tool-part interfacial stress development between T800S/3900-2B laminates with $[90/0/\overline{90}]_s$ layups and a steel tool covered with three Frekote 710-NC release coats.

Upon gelation, tool-part stresses evolved rapidly, dropped sharply after reaching a maximum value, then decreased nonlinearly through the remainder of the isothermal hold at 180 °C. The initial rise in stress upon gelation represents sticking (i.e., static friction) between the tool and part while the thermoset base resin is in its rubbery phase.[25] Since the temperature is well above the glass transition temperature of the thermoplastic particles, these components are also in a rubbery state. The friction between a rubbery solid and a hard surface (e.g., a tool) is mainly controlled by two mechanisms: interfacial adhesion and internal viscoelastic (VE) deformations.[56] Interfacial adhesion directly results from surface free energy (SFE) effects causing the rubbery polymer chains to form adhesive bonds and become "pinned" to atoms on the tool surface. On the other hand, internal VE contributions arise due to strain resistance from polymer chains in the bulk of the rubbery material. When subjected to normal pressure and in-plane strain, applied forces cause the rubber's polymer chains to align and stretch, leading to energy dissipation via internal VE mechanisms, as schematically illustrated in **Figure 2-44**.[56] The figure also shows two-dimensional surface micrographs of a T800S/3900-2B part and release-coated tool surface after a cure cycle to illustrate the physical conditions at the tool-part interface during processing.

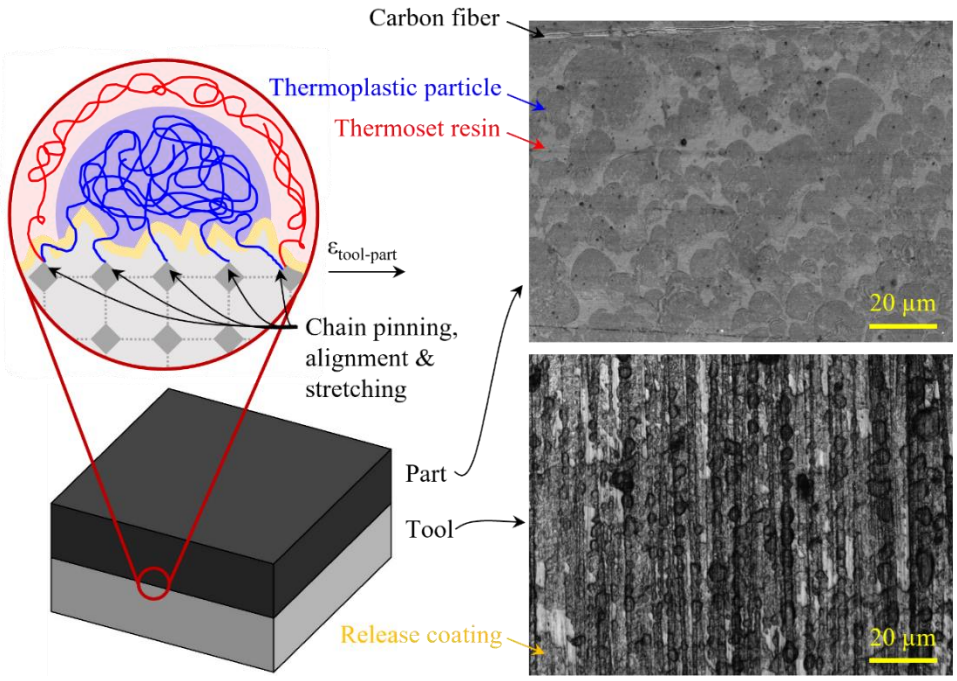

Figure 2-44. Schematic of bulk viscoelastic strain resistance mechanisms contributing to tool-part interaction (left) and digital surface micrographs of a cured T800S/3900-2B laminate and post-processing release-coated tool surface (right).

Since Frekote 710-NC RA with exceptionally low SFE properties (i.e., ~19 mJ/m^2) was applied to the tool before processing, strong interfacial adhesive bonds were unlikely to form during the DMA shear test. Therefore, the linear increase in stress upon gelation was primarily due to the internal VE effects in the composite's base resin and thermoplastic particles. In such a condition, internal VE strain resistance can be estimated as:

$$\tau \approx \tau_{VE} \approx PC \frac{E''}{\sqrt{E''^2 + E'^2}} \tag{2-34}$$

where τ is the interfacial stress, P is the normal pressure, C is a constant depending on the surface roughness of the tool, E'' is the loss modulus, and E' is the storage modulus of the rubbery material.[83,84] Since both thermoset matrix and thermoplastic particles were in direct contact with the tool surface when the interfacial strain was applied (**Figure 2-44**), the total interfacial stress would thus be approximately equal to the sum of the individual contributions:

$$\tau \approx \tau_{VE} \approx PC\left(A_{ts}\frac{E''_{ts}}{\sqrt{{E''_{ts}}^2+{E'_{ts}}^2}}+A_{tp}\frac{E''_{tp}}{\sqrt{{E''_{tp}}^2+{E'_{tp}}^2}}\right) \quad (2\text{-}35)$$

where A_{ts} is the area fraction of thermoset in contact with the tool surface, A_{tp} is the area fraction of thermoplastic in contact with the tool surface, E''_{ts} and E''_{tp} are loss moduli of the thermoset and thermoplastic components, and E'_{ts} and E'_{tp} are storage moduli of the thermoset and thermoplastic components. The fractional terms in (2-35) will be referred to as each component's "viscoelastic contribution" throughout the remainder of this section.

After approximately ten minutes (i.e., ~0.5 mm), interfacial stresses reached a maximum value of 489 kPa before sharply dropping. This ultimate stress value is the tool-part debonding stress (τ_{db}) and signifies the transition from static to kinetic friction. **Figure 2-43** illustrates that debonding occurred while the thermoset resin and thermoplastic particles were still in their rubbery states ($T > T_{g,ts}$ and $T > T_{g,tp}$). As such, during debonding, rubbery polymer chains on the part's surface undergo a rapid "snapping" or "unpinning" from the tool.[56]

The post-debonding regime in **Figure 2-43** shows a sharp drop in stress to approximately 150 kPa, then a nonlinear decline during the isothermal hold. The gradual stress decay represents sliding or kinetic friction between the tool and part.[25] After tool-part debonding, the glass transition temperature of the thermoset resin was rapidly evolving and approaching the processing temperature. However, the thermoplastic particles' glass transition temperature remained constant and below 180 °C. In other words, the composite's thermoset resin was transitioning from a rubbery viscoelastic body to a glassy elastic solid, while the thermoplastic particles remained in their rubbery state. As the thermoset transitions to an elastic solid, its VE contributions to tool-part stress are reduced, and mechanical friction becomes a non-negligible stress-contributing mechanism.[23]

The thermoset's transition to an elastic solid would reduce its viscoelastic contribution term in (2-35) and cause a direct decline in overall sliding stress values, as validated in **Figure 2-43**. Upon reaching the end of the vitrification zone, the thermoset acts like a fully elastic solid, and the dominant stress-contributing mechanism shifts to mechanical friction.[23] The final sliding stress value of approximately 35 kPa was thus primarily determined by internal VE effects in the thermoplastic particles and, secondarily, by mechanical friction in the thermoset resin.

2.3.3.2 Impacts of Tool Surface Condition

Figure 2-45 shows tool-part interfacial stress developments throughout the MRCC for five tool surface conditions, including FEP and one to four coats of Frekote 710-NC. Note that strain is plotted in logarithmic scale to illustrate discrepancies between tests more clearly. Two measured stress developments for each tool surface condition are shown by solid-colored curves, while the black dashed curve shows the simulated degree of cure (DoC) throughout the cycles.[63] A laminate layup of $[90/0/\overline{90}]_s$ and cure temperature of 180 °C were utilized for all tests.

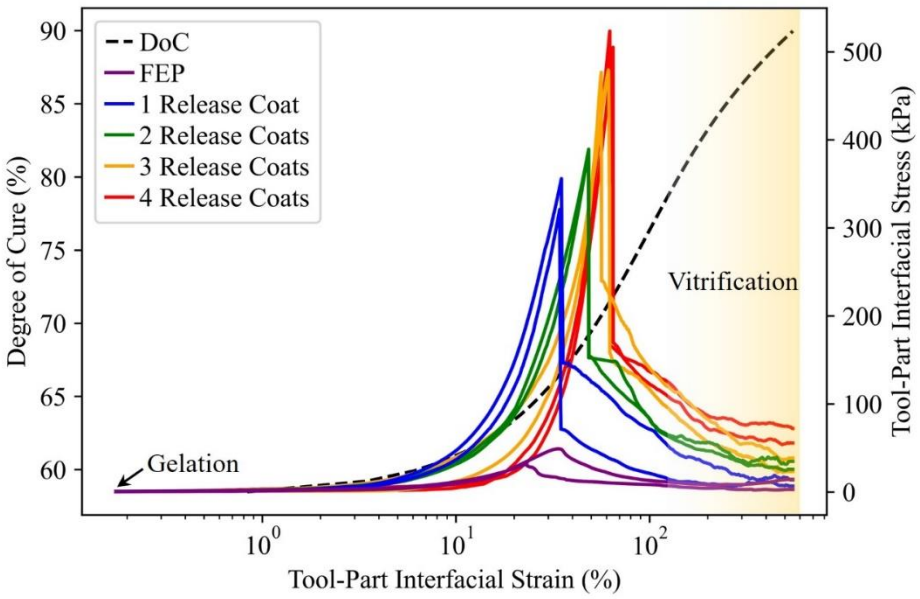

Figure 2-45. Tool-part interfacial stress developments measured for five tool surface conditions, including FEP release film and one to four Frekote 710-NC release coats.

The stress developments reported in **Figure 2-45** demonstrate that tool-part interaction for T800S/3900-2B is sensitive to tool surface conditions. These results also reveal interfacial sticking behavior during processing, regardless of the number of applied release coats. In contrast, when the U-shaped tool was covered with FEP film, stress developments were relatively gradual while lacking a sharp drop after debonding. These results are consistent with previous studies on the observation that FEP release film prohibits tool-part adhesive bonding.[24,25]

Figure 2-45 and **Figure 2-46** demonstrate that tool-part debonding stresses and, as previously discussed, tool surface roughness increased with each applied release coat. Data points in **Figure 2-46** represent the average values from two DMA tests and six laser profiles, while error bars correspond to the standard deviations within each measurement set. Although sliding stresses cannot be quantified using a single value, a general increasing trend with some overlapping can also be observed in **Figure 2-45**.

The direct increases in interfacial stress and surface roughness levels may be attributed to the agglomeration of release coating on the tool surface, a phenomenon illustrated in the sample micrographs for each condition superposed in **Figure 2-46**. As previously discussed, when a fresh coat of 710-NC is applied on top of a low-energy surface, it forms agglomerations (i.e., bumps) rather than a smooth layer, causing an increase in tool surface roughness. Although elevated pressures and temperatures cause Frekote agglomerations to behave rubbery during autoclave curing, an increase in pre-processing tool surface roughness is typically associated with elevated levels of tool-part mechanical bonding and residual stress transfers.[9,23] These results suggest that, if only completing one processing cycle, manufacturers should treat tools with conservative amounts of 710-NC release coating (i.e., only enough to restrict permanent tool-part bonding) to

reduce residual stresses and PIDs. If completing a series of processing cycles, the effects of release coating aging on tool-part stress developments must also be considered.[45]

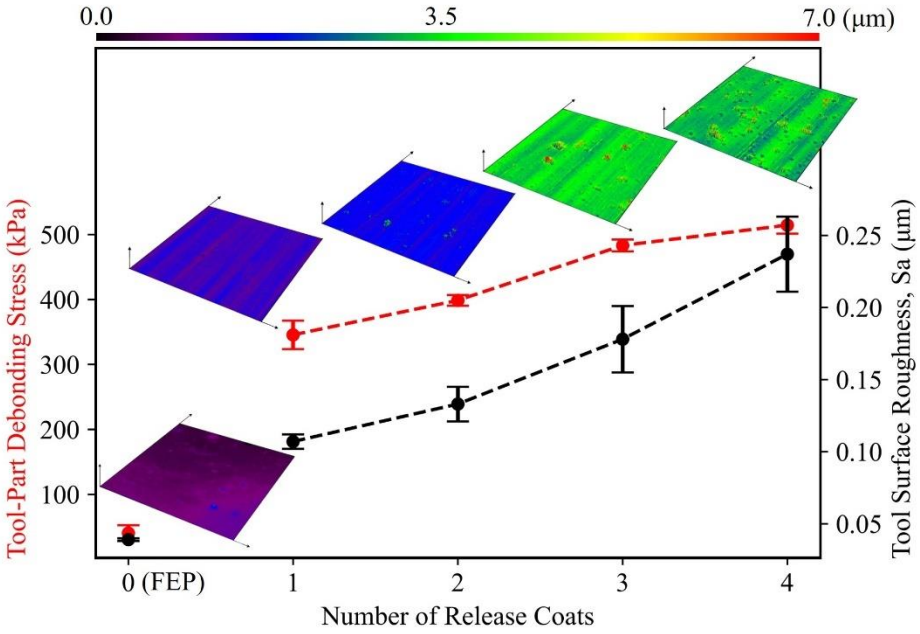

Figure 2-46. Tool-part debonding stresses measured in the DMA shear test, tool surface profiles, and tool roughness for five tool surface conditions.

Figure 2-47 illustrates the evolution of tool-part stresses during the MRCC for a tool treated with two coats of B-15 mold sealer and three 710-NC coats, aged between zero and six cycles. The B-15/710-NC release coating underwent aging through consecutive DMA tests without intermittent cleaning or reapplication steps. Stress developments after each aging period are shown by solid-colored curves, while the black dashed curve shows the simulated DoC throughout the cycles.[63] A laminate layup of $[90/0/\overline{90}]_s$ and temperature of 180 °C were utilized for all trials.

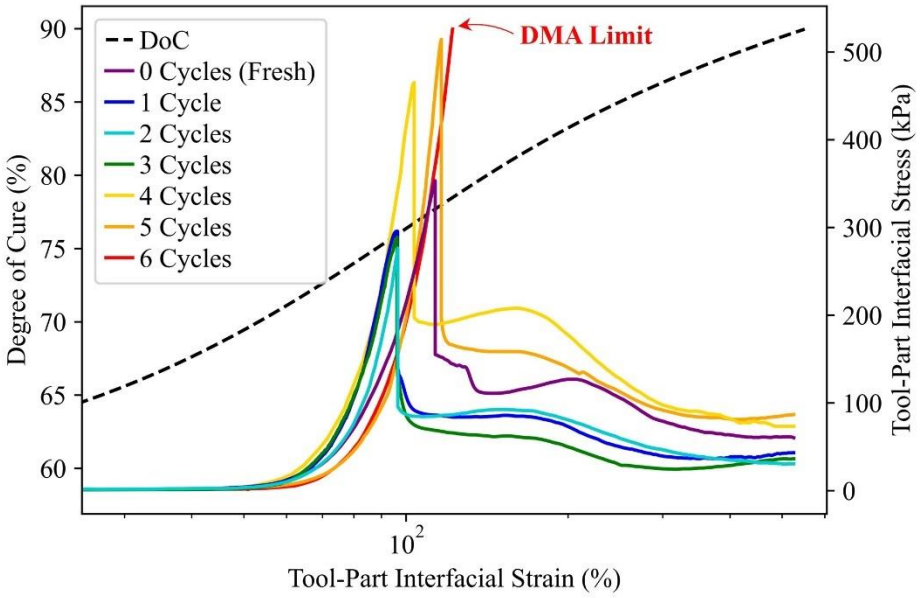

Figure 2-47. Tool-part interfacial stress developments measured for various ages of B-15/710-NC release coating using the custom DMA shear test.

The stress trends depicted in **Figure 2-47** prompt several significant discussions. Firstly, combining two layers of B-15 with three layers of 710-NC on the U-shaped tool resulted in lower debonding stresses compared to using three layers of 710-NC alone (**Figure 2-45**). This difference may be attributed to the tool surface being smoother and having lower SFE when both products were utilized together, as illustrated in **Figure 2-5**, **Figure 2-6**, and **Figure 2-11**. Secondly, the lowest debonding stresses were measured when the U-shaped tool was treated with release coating aged for two cycles. Beyond this point, tool-part stresses increased with each cycle, eventually surpassing the DMA's stress limit (~ 526 kPa) and rendering them immeasurable. These trends closely follow previous findings, where the lowest SFE values were also measured after two processing cycles due to conditioning effects (**Figure 2-12**). Overall, the findings in **Figure 2-47** underscore the importance of utilizing mold sealer and release agent together and employing proper conditioning strategies to minimize tool-part interfacial stresses during processing.

2.3.3.3 Impacts of Cure Pressure

Figure 2-48 shows tool-part interfacial stresses for five cure pressures ranging from 101 to 763 kPa. Two measured stress developments for each cure pressure are indicated by solid-colored curves, while the black dashed curve shows the DoC.[63] A laminate layup of $[90/0/\overline{90}]_s$, tool surface condition of three 710-NC release coats, and cure temperature of 180 °C were utilized for all trials. Although general behaviors were similar between the trials, the plot illustrates that tool-part debonding and sliding stresses are nonlinearly affected by cure pressure. The average debonding stresses were maximum at a cure pressure of 347 kPa and minimum at 101 kPa. Sliding stresses were comparatively minimal for the 101 kPa trials but were very similar for the other cure pressures with no clear trends.

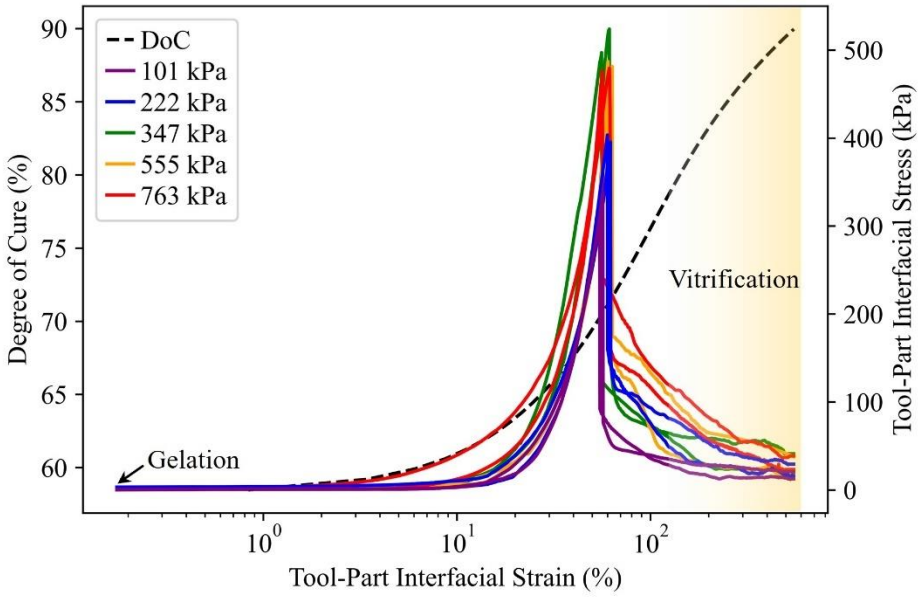

Figure 2-48. Tool-part interfacial stress developments measured for five cure pressures using the custom DMA shear test.

Figure 2-49 demonstrates that the highest debonding stresses measured at intermediate pressures corresponded to composite parts containing approximately 50% thermoset resin and 50% thermoplastic on its tool-adjacent surface. Data points in the plot represent the average values from

two DMA tests and six laser profiles, while error bars correspond to the standard deviations of each measurement set. The nonlinear relationship between cure pressure and tool-part stresses demonstrates that Amontons' law, which states a direct proportionality between interfacial stress and normal pressure, does not apply when one of the bodies is in a rubbery state.[84]

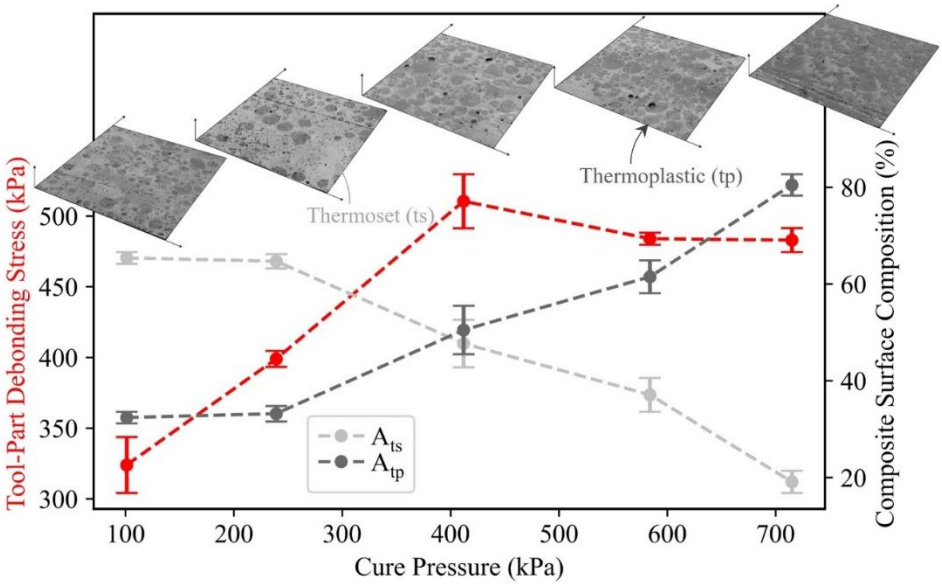

Figure 2-49. Tool-part debonding stresses measured in the DMA shear test, composite tool-side surface profiles, and composite tool-side surface composition for five cure pressures.

During processing, the thermoplastic particles become rubbery before the gelation of the thermoset matrix. This allows the thermoset resin to flow and the thermoplastic particles to deform under the applied pressure. Higher pressure leads to greater particle deformation, increased thermoplastic surface fraction (A_{tp} in (2-35)), and reduced thermoset resin (A_{ts} in (2-35)) on the tool-side surface, as illustrated in the micrographs in **Figure 2-20** and **Figure 2-49**. This affects the total VE contributions to tool-part stresses, with surfaces dominated by thermoplastic exhibiting lower debonding stresses. Overall, the nonlinear trends in tool-part stress magnitudes demonstrate that levels of tool-part interaction are highest at intermediate cure pressures in the range of 300–500 kPa due to competing VE contributions between the thermoplastic and thermoset

components during processing. These pressures should thus be avoided during manufacturing if attempting to minimize residual stresses from tool-part interaction in composite parts.

2.3.3.4 Impacts of Laminate Layup

Figure 2-50 shows tool-part interfacial stresses throughout the MRCC for three laminate layups, including $[0/90/\overline{0}]_s$, $[45/\text{-}45/\overline{45}]_s$, and $[90/0/\overline{90}]_s$. A cure pressure of 763 kPa, tool surface condition of three 710-NC release coats, and cure temperature of 180 °C were kept constant for all the trials. Upon gelation and subjection to strain, all stress profiles exhibited sticking and debonding behavior within a narrow window of 69 – 74% degree of cure. The magnitudes of debonding stresses ranged from 412 to 496 kPa, with the lowest and highest values occurring for $[45/\text{-}45/\overline{45}]_s$, and $[90/0/\overline{90}]_s$ laminates, respectively. In general, the highest sliding stresses were measured for the laminates with 0° plies adjacent to the tool surface and fibers aligned parallel to the tool-part strain, while the lowest stresses were measured for the 45° laminates.

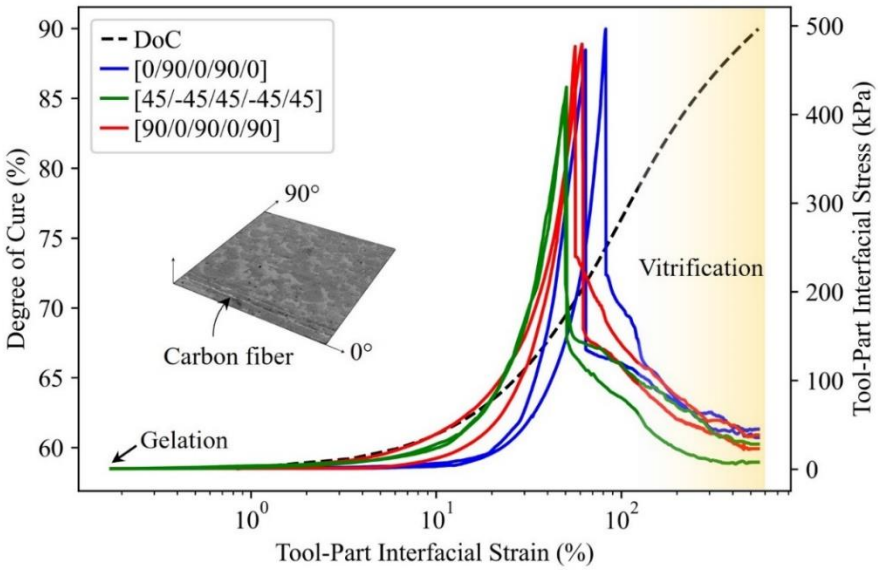

Figure 2-50. Tool-part interfacial stress developments measured for three laminate layups using the custom DMA shear test.

Previous discussions in this work have attributed interfacial stress magnitudes to internal VE strain resistance in the rubbery T800S/3900-2B material. However, it has been noted in

previous research that the presence of 90° plies non-adjacent to the tool surface can increase interfacial stresses due to mechanical interlocking and reduced stress relaxation.[24] The effects of 45° plies near the tool-part interface have not been explored, suggesting the need for future research to explain the trends observed in **Figure 2-50**. Overall, the findings in **Figure 2-50** indicate that incorporating 45° plies adjacent to the tool-part interface may reduce tool-part interaction and residual stresses during manufacturing.

2.3.3.5 Impacts of Cure Temperature

Figure 2-51 and **Figure 2-52** show duplicate tool-part interfacial stress developments for two one-hold cure cycles with alternative temperatures as compared to the MRCC. During the tests, the tool surface condition, cure pressure, laminate layup, and strain rate were kept constant at three 710-NC release coats, 763 kPa, $[90/0/\overline{90}]_s$, and 0.05 mm/min, respectively. It is most appropriate to compare the tool-part stress evolutions with values measured during the MRCC trial with a 180 °C cure temperature (**Figure 2-43**). Due to the dimensions of the U-shaped tool, only about 7.5 millimeters of displacement could be applied during testing, and thus the 140 °C and 160 °C cycles do not reach a complete degree of cure. Therefore, the alternate cycles were utilized to cause gelation and vitrification of T800S/3900-2B at different temperatures, and to investigate the effects on stress evolutions.

At a temperature of 140 °C, the composite underwent gelation and experienced strain slightly below the glass transition temperature of the thermoplastic particles. This resulted in an average tool-part debonding stress of 492 kPa. In contrast, during the one-hold cycle at 160 °C, the composite gelled and underwent strain just above the glass transition temperature of the thermoplastics, leading to an average debonding stress of 440 kPa. As previously mentioned, the average tool-part debonding stress for the MRCC cycle at 180 °C was 483 kPa. The observed

nonlinear correlation between cure temperature and tool-part stress magnitudes can likely be attributed to the unique evolutions of the composite's VE properties during each cycle.

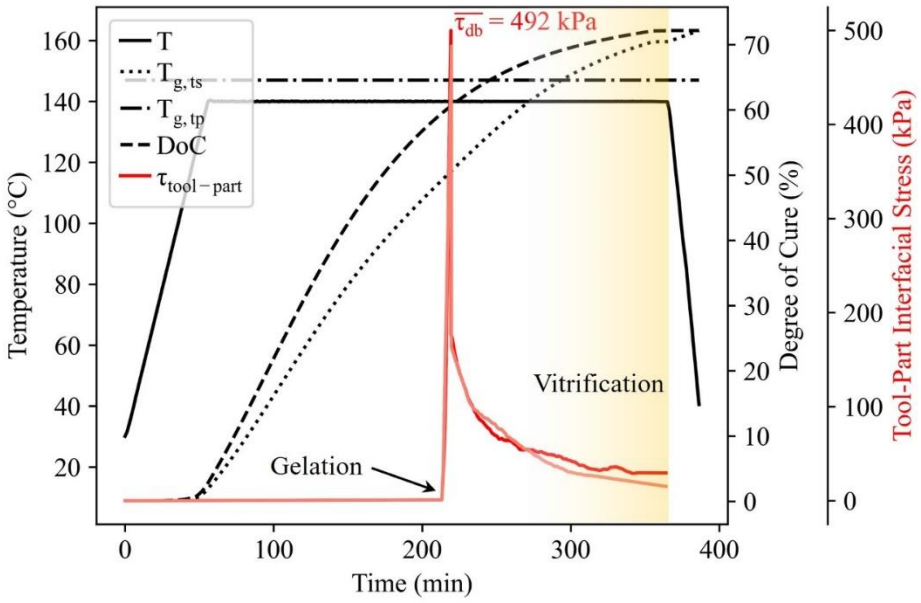

Figure 2-51. Tool-part interfacial stress development measured for a 140 °C cure temperature using the custom DMA shear test.

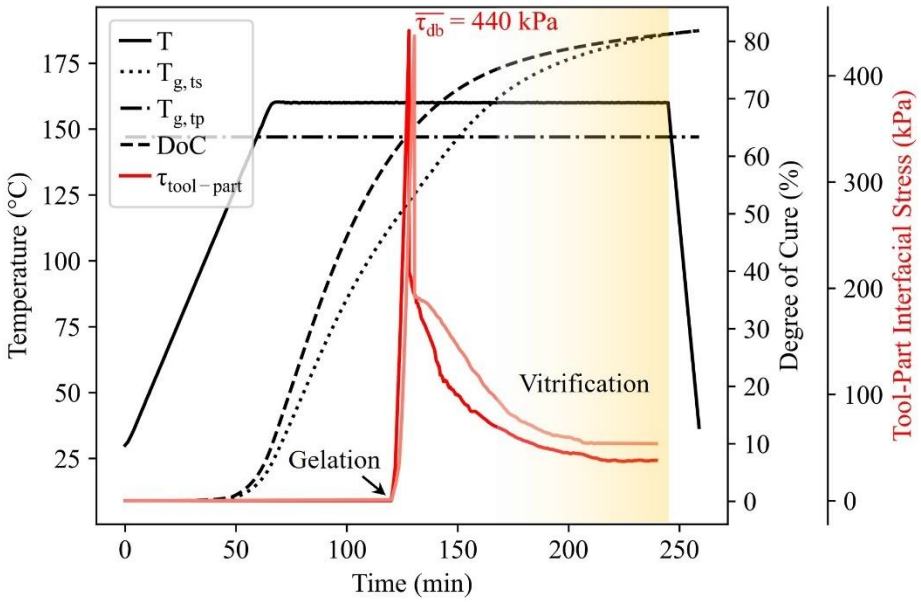

Figure 2-52. Tool-part interfacial stress development measured for a 160 °C cure temperature using the custom DMA shear test.

2.3.3.6 Impacts of Tool-Part Displacement Rate

Figure 2-53 shows tool-part interfacial stresses for three applied displacement rates, including 25, 50, and 75 µm/min. Solid-colored curves show two measured stress developments for each rate. During the tests, the tool surface condition was three 710-NC release coats, cure pressure was 763 kPa, and laminate layup was $[90/0/\overline{90}]_s$. The magnitudes of debonding stresses ranged from 371 to 489 kPa, with the lowest and highest values occurring for 75 µm/min and 50 µm/min, respectively. Sliding stresses were also generally the highest for the 50 µm/min, but lowest for the rate of 25 µm/min. Although not drastic, the lower debonding stresses for the 75 µm/min trials may have been due to the slight reduction in the degree of cure at the point of interfacial failure. Overall, the results in **Figure 2-53** suggest that tool-part debonding stresses may depend on the in-plane displacement rate at higher rates.

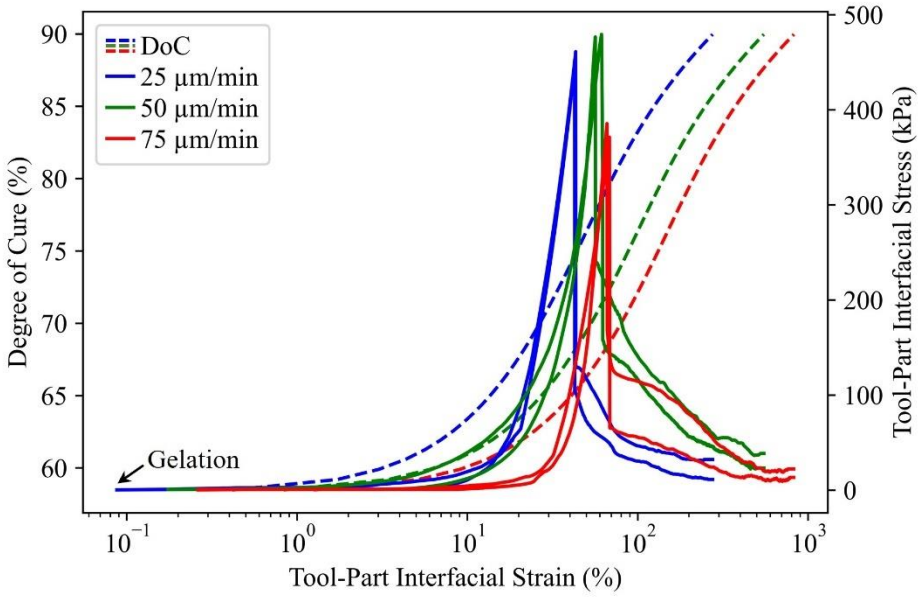

Figure 2-53. Tool-part interfacial stress developments measured for three applied displacement rates using the custom DMA shear test.

2.4 SUMMARY

In this chapter, investigations of B-15/710-NC release coating, T800S/3900-2B, and tool-part interactions were conducted. The investigation into release coating involved the use of laser scanning digital microscopy, Fourier-transform infrared spectroscopy (FTIR), and contact angle goniometry to analyze the effects of release coating type, quantity, and age on surface morphology, chemistry, and surface free energy. Evaluations of T800S/3900-2B consisted of using various microscopic techniques and dynamic mechanical analysis (DMA) to investigate the impacts of processing variabilities on the material's morphology, cured viscoelastic properties, and thermo-mechanical properties throughout the curing process. Tool-part interaction studies were conducted using a custom-built technique installed in a DMA capable of directly measuring interfacial stress developments during composites processing. The key findings from this chapter are as follows:

- The physical and chemical characteristics of tool surfaces are directly influenced by the type, quantity, and aging of the applied release coating. When using Frekote 710-NC alone, an increase in the number of layers results in higher tool surface roughness and surface free energy. However, the application of B-15 mold sealer prior to 710-NC significantly reduces tool surface roughness and surface free energy. During the initial processing cycles of a B-15/710-NC release-coated tool, a conditioning process occurs, where the coating's properties become "locked-in" and can remain stable for more than twenty autoclave processing cycles. Optimal conditioning for achieving the lowest surface free energy is likely between one and three processing cycles.
- The morphology of T800S/3900-2B can be manipulated by varying the processing pressure, with higher pressures resulting in increased deformation of thermoplastic particles. Cured T800S/3900-2B laminates exhibit unique viscoelastic properties,

including broad relaxation behaviors observed at sub-zero temperatures. The evolution of T800S/3900-2B's storage modulus and free strains while curing is significantly influenced by the thermal loading conditions applied during processing. Both modulus and free strain magnitudes demonstrate unique correlations with processing temperature, with larger absolute values generally occurring at lower temperatures and vice versa.

- Tool-part interfacial stresses for T800S/3900-2B are highly impacted by processing variabilities (**Table 2-6**). Regarding the tool surface condition, excessive application of 710-NC release coating leads to the highest levels of tool-part debonding and sliding stresses. Conversely, using smaller amounts of 710-NC or combining B-15 with 710-NC helps reduce these stresses. In terms of pressure, the most pronounced tool-part debonding stresses and PIDs are observed at intermediate pressures ranging from approximately 300 to 500 kPa, where the composite part's tool-adjacent surfaces consist of roughly equal proportions of thermoset resin and thermoplastic particles. Laminate layup and cure temperature also impact tool-part interaction behaviors due to mechanical and viscoelastic mechanisms.

Table 2-6. Tool-part debonding and sliding stress magnitudes measured for different process variabilities using a custom DMA shear test.

Tool Surface Condition	P (kPa)	Laminate Layup	T (°C)	$\dot{\varepsilon}$ (mm/min)	τ_{db} (kPa)	τ_{sl} (kPa)
FEP	763	$[90/0/\overline{90}]_s$	180	0.050	40	39 – 9
1 710-NC Coat	763	$[90/0/\overline{90}]_s$	180	0.050	346	129 – 17
2 710-NC Coats	763	$[90/0/\overline{90}]_s$	180	0.050	399	163 – 35
3 710-NC Coats	763	$[90/0/\overline{90}]_s$	180	0.050	483	204 – 36
4 710-NC Coats	763	$[90/0/\overline{90}]_s$	180	0.050	514	168 – 64
B-15/710-NC Coating (Age: 0 Cycles)	763	$[90/0/\overline{90}]_s$	180	0.050	353	113 – 60
B-15/710-NC Coating (Age: 1 Cycle)	763	$[90/0/\overline{90}]_s$	180	0.050	296	100 – 46
B-15/710-NC Coating (Age: 2 Cycles)	763	$[90/0/\overline{90}]_s$	180	0.050	276	93 – 31
B-15/710-NC Coating (Age: 3 Cycles)	763	$[90/0/\overline{90}]_s$	180	0.050	289	82 – 36
B-15/710-NC Coating (Age: 4 Cycles)	763	$[90/0/\overline{90}]_s$	180	0.050	465	197 – 73
B-15/710-NC Coating (Age: 5 Cycles)	763	$[90/0/\overline{90}]_s$	180	0.050	514	170 – 38
B-15/710-NC Coating (Age: 6 Cycles)	763	$[90/0/\overline{90}]_s$	180	0.050	> 526	
3 710-NC Coats	101	$[90/0/\overline{90}]_s$	180	0.050	324	85 – 17
3 710-NC Coats	222	$[90/0/\overline{90}]_s$	180	0.050	399	150 – 23
3 710-NC Coats	347	$[90/0/\overline{90}]_s$	180	0.050	511	151 – 31
3 710-NC Coats	555	$[90/0/\overline{90}]_s$	180	0.050	484	171 – 27
3 710-NC Coats	763	$[0/90/\overline{0}]_s$	180	0.050	485	177 – 40
3 710-NC Coats	763	$[45/-45/\overline{45}]_s$	180	0.050	422	178 – 18
3 710-NC Coats	763	$[90/0/\overline{90}]_s$	140	0.050	492	170 - 22
3 710-NC Coats	763	$[90/0/\overline{90}]_s$	160	0.050	440	203 - 46
3 710-NC Coats	763	$[90/0/\overline{90}]_s$	180	0.025	454	117 – 22
3 710-NC Coats	763	$[90/0/\overline{90}]_s$	180	0.075	378	117 – 18

3. ACCELERATED CHARACTERIZATION OF COMPOSITES USING PROBABILISTIC MACHINE LEARNING

3.1 BACKGROUND

Efficient analysis of composites manufacturing relies on thoroughly understanding relationships between processing parameters and material properties.[26] As demonstrated in the previous chapter, this knowledge is typically gained through a series of many characterization tests and the fitting of deterministic models to approximate the testing data. Unfortunately, this traditional model-based (MB) approach requires significant time and financial investments, particularly when attempting to understand complex materials. For example, in the previous chapter, the total testing time required to characterize the evolution of T800S/3900-2B's storage modulus and free strains exceeded 200 hours. Moreover, relying on deterministic fitting methods often oversimplifies the inherently probabilistic nature of composites and can lead to further misunderstandings and inaccuracies. While insights gained from traditional methods are invaluable, such extensive testing time serves as a prime example of one obstacle hindering progress in composites manufacturing. Thus, improving the traditional MB characterization workflow or developing alternative methods may be critical to help improve the efficiency of composites design, development, and manufacturing.

This chapter provides a novel approach for the accelerated characterization of composites using probabilistic machine learning (ML). The proposed strategy involves training surrogate models using Gaussian Process Regression (GPR) and limited amounts of experimental data.[85–88] In recent years, GPR has been applied to solve various composites science and engineering problems (e.g., failure predictions[89], manufacturing assessments[90]), and is thus a promising candidate to explore for material characterization. The method outlined in this chapter offers a

cost-effective and broadly applicable strategy for characterizing advanced materials and more efficiently understanding complex manufacturing phenomena.

3.2 METHODS

In this section, a methodology for efficient characterization of composites is introduced through a case study focused on thermo-mechanical properties of T800S/3900-2B. The primary objective of the method is to develop accurate models capable of describing and predicting material properties across various processing conditions, without the need for extensive experimental efforts. For this case study, the goal is to characterize the evolution of T800S/3900-2B's storage modulus and free strains while curing under different thermal loading conditions. To initiate this process, a limited set of experimental data must first be obtained. Instead of conducting new experiments, data acquired from bi-material beam (BMB) tests in the previous chapter (**Figure 2-23 – 2-31**) will be utilized for this task. Given the objective of minimizing experimental efforts, the process will begin by conducting (i.e., obtaining data from) two BMB tests. For this method to be most effective, the initial two tests should be diverse, meaning they should not impose similar or closely aligned processing conditions on the composite material.

After conducting two experiments, the initialization of predictive models for each thermo-mechanical property being characterized (i.e., modulus and free strains) begins. To initiate this process, numerical values serving as parametric inputs for BMB tests in a predictive model must be obtained. During the parametrization process, similar positions in an input space should yield similar outputs to permit an inherent "smoothness" in the model's predictions. Various methods can be employed to enhance the likelihood of achieving this smoothness, including the use of closed-form physical theories, observation of trends/relationships in the initial testing data, or other approaches.[91] In this case study, parametrization was accomplished by leveraging the

temperature-dependent connections between test results observed in the previous chapter Two parameters were obtained for each type of testing data, enabling the subsequent interpretation of the models as 3D surfaces.

After parametrization, the probabilistic machine learning technique, Gaussian Process Regression (GPR), is employed for model fitting using a custom Python code which functions as follows.[92] First, the parametrized testing data, consisting of two numerical inputs and one thermo-mechanical property output, is imported. The inputs and outputs are then normalized such that they have a mean of zero and standard deviation of one. This step helps in improving the convergence of the GPR optimization algorithm by ensuring that features are on a similar scale, thus preventing some features from dominating others during the training process.[87] Following normalization, a kernel is selected for GPR training, with the code offering many flexible options such as Constant, Rational Quadratic, Radial Basis Function (RBF), Dot Product, Matérn, and others.[85] During fitting, a kernel should be chosen which captures the complexity of the testing data without possessing a high chance of overfitting. This approach will allow the GPR model to adapt to different data structures and capture probabilistic variations.[85] After kernel selection, its covariance function is employed for GPR training, where an underlying function is predicted as the mean of a distribution over functions, following a generalized scheme of:

$$f(x) \sim \mathcal{GP}\big(m(x), k(x, x')\big) \tag{3-1}$$

where $f(x)$ is a function to be predicted, $\mathcal{GP}$ is the Gaussian Process, $m(x)$ is the mean function, and $k(x, x')$ is the kernel function describing covariance between points x and x'.

Upon initializing GPR, the trained model (i.e., predicted function) is utilized to predict thermo-mechanical outputs for training and testing datasets. In this study, the testing dataset comprises parameters corresponding to an unconventional cure cycle formulated specifically for

validation purposes. The testing cycle involves heating from 20 °C to 120 °C at 1 °C/min, holding at 120 °C for 30 minutes, heating to 160 °C at 5 °C/min, holding at 160 °C for 120 minutes, cooling to 20 °C at 3.5 °C/min, heating to 300 °C at 5 °C/min, then cooling to 20 °C at 4 °C/min. Upon predicting thermo-mechanical properties for the training and testing data, the GPR code returns various performance statistics including accuracies and uncertainties. These metrics are then collected to establish confidence intervals and form a probabilistic surrogate model capable of predicting thermo-mechanical properties.

Following the initial GPR training, a calibration process begins by iteratively incorporating additional experimental data and evaluating the models' accuracy. To initiate calibration, one experiment is conducted with parameters exhibiting the highest uncertainty in the GPR model. The new experimental results are then integrated into the training dataset, the GPR model is retrained to predict material properties, and testing parameters surrounded by the highest uncertainty are identified. These parameters are then utilized for the next experiment, the resulting data is incorporated into the model, and GPR is retrained. This process continues until the GPR model meets desired accuracy requirements. In this study, each model's accuracy is assessed by predicting storage modulus and free strain evolutions of T800S/3900-2B throughout the previously discussed unconventional cure cycle.

3.3 RESULTS AND DISCUSSIONS

Figure 3-1 and **Figure 3-2** display GPR models and their predictions for T800S/3900-2B's storage modulus and free strains at different stages of cure. Red curves in the left-side plots represent testing data from BMB tests, green surfaces depict the GPR models' mean predictions, and grey surfaces are 95% confidence bounds. The GPR models were trained using a summation of the Matérn and white noise kernels in Python's scikit-learn library:[92,93]

$$k(x, x') = k_m(x, x') + k_w(x, x') \tag{3-2}$$

In the specified kernel, the Matérn component (k_m) detects non-linear relationships in the input space using Gaussian similarity and promotes smoothness in the model's response, while the k_w accounts for independent noise or measurement error in the data. In mathematical terms, the kernel can be defined as:

$$k(x, x') = \frac{1}{\Gamma(\nu)2^{\nu-1}}\left(\frac{\sqrt{2\nu}}{l}||x - x'||\right)^{\nu} K_{\nu}\left(\frac{\sqrt{2\nu}}{l}||x - x'||\right) + \sigma_n^2 \tag{3-3}$$

where Γ is the gamma function, ν is a parameter which controls the smoothness of the resulting function, l is the length scale, K_{ν} is a modified Bessel function, and σ_n^2 is a positive constant which represents the level of noise in the dataset.[85] In this study, default values of $\nu = 1.5$ and $l = 1$ were initially chosen for GPR training, then were optimized during each calibration phase using twenty restarts in scikit-learn's hyperparameter optimizer.[93]

The right sides of **Figure 3-1** and **Figure 3-2** display thermo-mechanical property predictions throughout the unconventional testing cycle, with black curves denoting the temperature, purple curves denoting experimental results, yellow curves denoting predictions from the traditional model-based (MB) approach, and green curves showing the GPR model's predictions. As previously mentioned, the MB predictions were made by completing 18 BMB tests, then fitting deterministic models to approximate the testing data ((2-22) – (2-33)). The accuracy and testing time of the MB approach are compared to the machine learning (ML) results in **Table 3-1**.

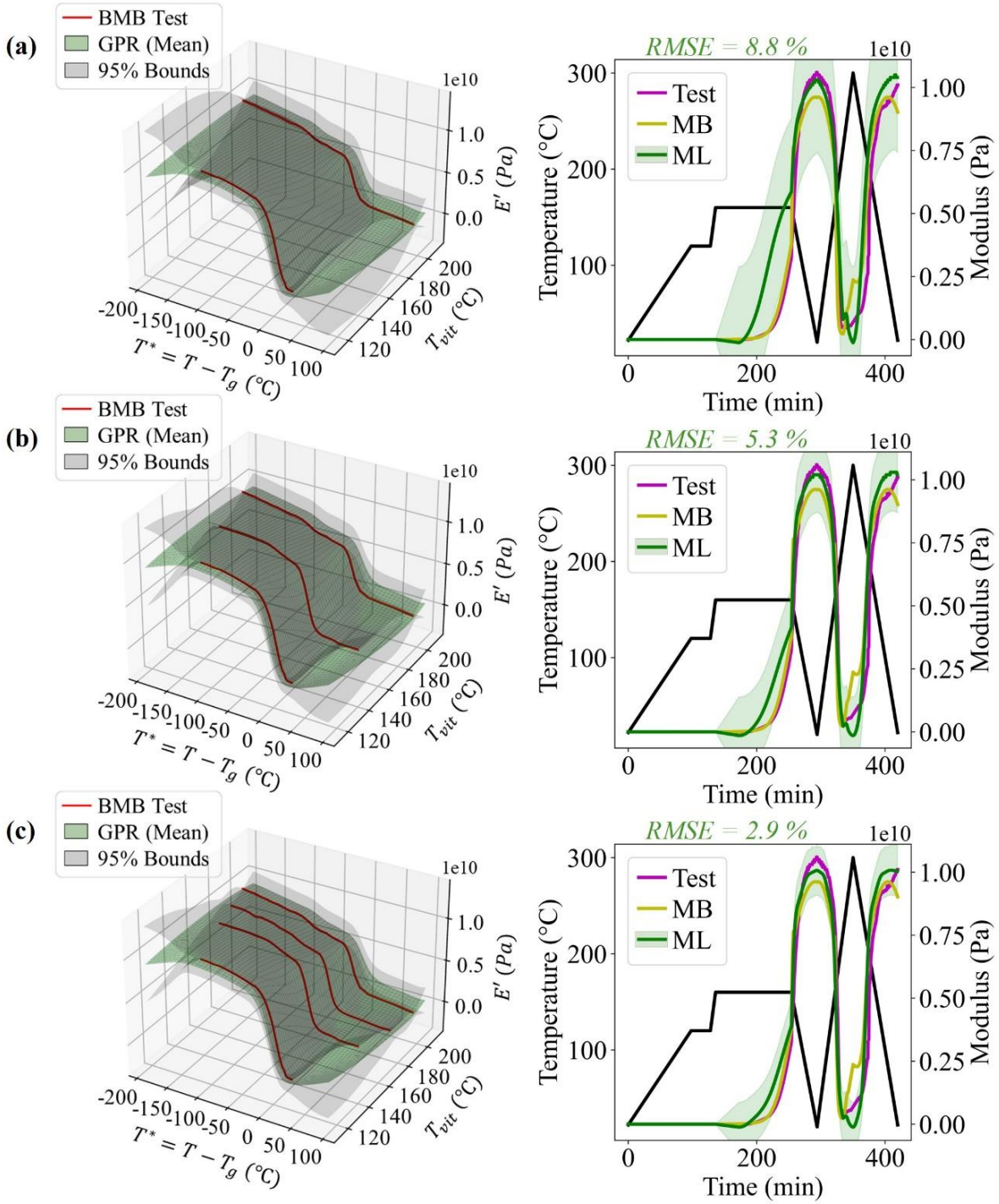

Figure 3-1. GPR model (left) and its predictions of T800S/3900-2B's storage modulus during an unconventional cure cycle (right) with different numbers of experimental results incorporated.

Figure 3-1a demonstrates that initially, the GPR model trained on two BMB tests, inducing gelation and vitrification at 120 °C and 200 °C, exhibited a RMSE of 8.8% on the testing cycle. As previously highlighted, these two experiments were specifically selected for initial training to ensure the GPR model is built upon diverse data, thereby enabling it to best approximate trends throughout the entire design space.[91] The GPR model was trained as a function of the difference between processing temperature and the composite's glass transition temperature, along with the temperature at which vitrification occurred in each cycle. These parameters were selected by identifying temperature-dependent trends in the initial data and subsequently integrating this knowledge into the model's domain.

In **Figure 3-1a**, the GPR model's mean response and confidence bounds tightly converge around the two experiments and smoothly diverge from regions lacking training data. While this model structure results in some inaccuracies at early stages of the testing cycle, its predictions closely resemble experimental results at later stages. These observations illustrate that by conducting just two BMB tests and fitting probabilistic GPR models with broadly applicable kernels, a reasonable approximation of the storage modulus behavior can be attained for an unconventional cure cycle.

Figure 3-1bc illustrate the improvement of the GPR model's accuracy with each additional experiment integrated into its training dataset. With the inclusion of three and four experiments inducing gelation and vitrification at 160 °C and 180 °C, the GPR model's predictions exhibit RMSE values of 5.3% and 2.9%, respectively. It is critical to note that despite the improvements, the MB approach still yields the closest approximation of storage modulus with an RMSE of 1.4%. However, the ML approach with four experiments required less than 25% of the testing time and is likely to further improve with the addition of more experiments.

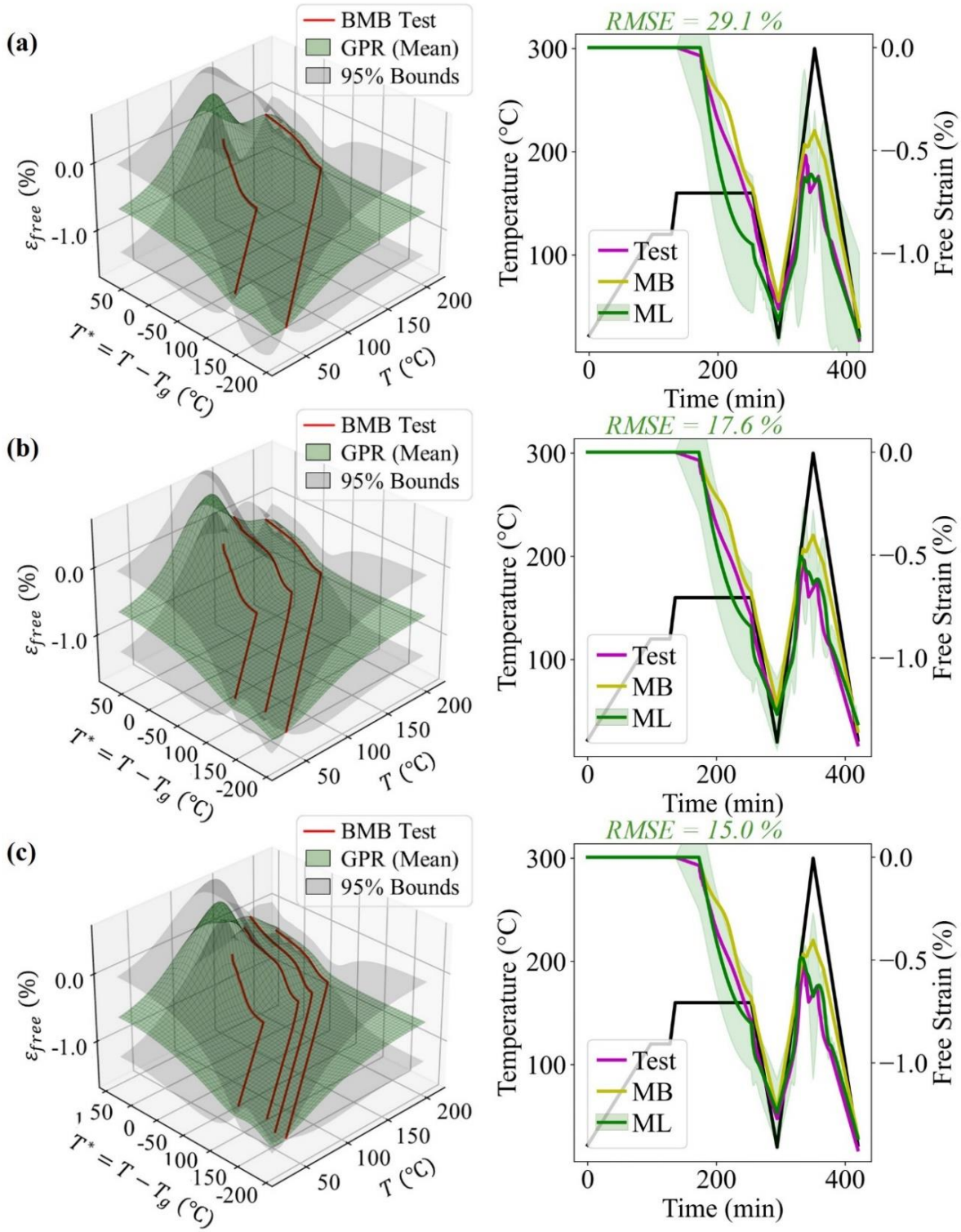

Figure 3-2. GPR model (left) and its predictions of T800S/3900-2B's free strains during an unconventional cure cycle (right) with different numbers of experimental results incorporated.

Figure 3-2 demonstrates the efficacy of the ML approach in characterizing T800S/3900-2B's free strains during processing. With the integration of test results from the same two, three, and four experiments utilized for modulus characterizations, the GPR model yielded RMSEs of 29.1%, 17.6%, and 15.0% respectively. It is important to note that these percentages are relatively higher compared to modulus errors due to the inherently low absolute values of free strains. In the task of characterizing free strains, the ML approach outperformed MB methods after just three experiments. These results underscore an additional potential drawback of the MB approach, particularly in its struggle to generalize and predict behaviors outside of the model's initial training regime. In this case, the MB approach encountered difficulty in predicting thermal expansion behaviors at temperatures exceeding those used during BMB testing and training. In contrast, the probabilistic ML approach seemed to predict these behaviors well with a much smaller amount of testing.

Table 3-1. Performance comparison of different methods employed for thermo-mechanical characterization.

Method	Testing Time (hr)	Modulus RMSE (%)	Free Strain RMSE (%)
Model-based (MB)	~ 204	1.4	23.0
Machine Learning (ML)	~ 29	8.8	29.1
Machine Learning (ML)	~ 38	5.3	17.6
Machine Learning (ML)	~ 46	2.9	15.0

3.4 SUMMARY

In this chapter, a novel method for the accelerated characterization of composites was presented. The technique utilized limited experiments and the probabilistic machine learning (ML) technique, Gaussian Process Regression (GPR), to efficiently construct accurate predictive models of T800S/3900-2B's thermo-mechanical properties. Results illustrated that even with just a few experiments, the GPR models could provide highly accurate predictions of storage modulus and free strains, offering significant time and cost savings compared to traditional model-based (MB)

approaches. Moreover, the flexibility of the approach allows for easy expansion to include additional materials, properties, and phenomena, highlighting its potential for widespread application in composite materials research and manufacturing.

4. PARAMETRIC INVESTIGATIONS OF PROCESS-INDUCED DEFORMATIONS IN L-SHAPED COMPOSITE PARTS

4.1 BACKGROUND

In this chapter, the thermo-mechanical models developed in Chapter 2 are leveraged to evaluate the impacts of processing variabilities on PIDs of L-shaped T800S/3900-2B parts. This investigation utilizes a numerical finite element (FE) framework with integrated reduced-order and analytical solutions to efficiently evaluate the impacts of layup configurations and cure cycle designs. The analyses focus on discovering novel relationships between processing parameters and PIDs to guide future research for better understanding deformations in advanced composites.

4.2 METHODS

The simulation method employed in this chapter is a multi-component numerical approach implemented through a custom Python code.[92] The method's first step involves defining the layup and geometry of a composite part, the material and geometry of a tool, and a temperature cycle which can be customized with variable heating, holding, and cooling stages. Once all the inputs are defined, the simulation progresses to a one-dimensional (1D) thermo-chemical analysis. In this stage, finite element (FE) meshes are generated to represent the tool and part in a 1D (i.e., through-thickness) heat transfer problem. The user-defined temperature cycle is then discretized, and Dykeman's cure kinetics model[63] is employed to predict the degree of cure (DoC) and glass transition temperature (T_g) of the composite at different time steps. Thermal properties of the tool and part are then calculated for each step by leveraging predicted cure states and other publicly

available data sources.[36,70] Finally, using the tool and part geometries, the 1D heat transfer problem is solved, and the temperature profile of each element throughout the defined cure cycle is predicted.

Following thermo-chemical analysis, the simulation transitions to a thermo-mechanical evaluation. First, isotropic modulus (E_r) and free strains (ε_{free_r}) in 3900-2B resin are predicted at different time-temperature steps using the previously computed cure states (i.e., α and T_g) along with models derived in Chapter 2 ((2-22) – (2-33)). Other isotropic resin properties, including Poisson's ratio (ν_r), viscosity (μ_r), shear modulus (G_r), and bulk modulus (k_r) are then computed:[66,94,95]

$$\nu_r = \frac{1}{2}\left(1 - \frac{E_r}{E_{r_\infty}}\left(1 - 2\nu_{r_\infty}\right)\right) - 0.001 \tag{4-1}$$

$$G_r = \frac{E_r}{2(1+\nu_r)} \tag{4-2}$$

$$k_r = \frac{E_r}{2(1-\nu_r-2\nu_r^2)} \tag{4-3}$$

where E_{r_∞} is the upper limit of the resin's modulus (3.25×10^9 Pa)[66] and ν_{r_∞} is the upper limit of Poisson's ratio (0.4).[96] The computed resin properties are then subsequently utilized in micromechanical predictions of T800S/3900-2B lamina-level properties throughout the defined cure cycle:[94]

$$G_{23_f} = \frac{E_{33_f}}{2(1+\nu_{23_f})} \tag{4-4}$$

$$k_f = \frac{1}{\left(\frac{4}{E_{33_f}} - \frac{1}{G_{23_f}} - \frac{4\nu_{13_f}^2}{E_{11_f}}\right)} \tag{4-5}$$

$$k_T = \frac{(k_f + G_r)k_r + (k_f - k_r)G_r V_f}{k_f + G_r - (k_f - k_r)V_f} \tag{4-6}$$

$$E_{11} = E_{11_f}V_f + E_r(1 - V_f) + \frac{4\left(\nu_r - \nu_{13_f}\right)^2 k_f k_r G_r(1 - V_f)V_f}{(k_f + G_r)k_r + (k_f + k_r)G_r V_f} \tag{4-7}$$

$$\nu_{12} = \nu_{13} = \nu_{13_f}V_f + \nu_r(1 - V_f) + \frac{\left(\nu_r - \nu_{13_f}\right)(k_r - k_f)G_r(1 - V_f)V_f}{(k_f + G_r)k_r + (k_f - k_r)G_r V_f} \tag{4-8}$$

$$G_{12} = G_r \frac{G_{13_f} + G_r + (G_{13_f} - G_r)V_f}{G_{13_f} + G_r - (G_{13_f} - G_r)V_f} \tag{4-9}$$

$$G_{23} = G_r \frac{k_r(G_r + G_{23_f}) + 2G_{23_f}G_r + k_r(G_{23_f} - G_r)V_f}{k_r(G_{23_f} + G_r) + 2G_{23_f}G_r - (k_r + 2G_r)(G_{23_f} - G_r)V_f} \tag{4-10}$$

$$E_{22} = \frac{1}{\left(\frac{1}{4k_T} + \frac{1}{4G_{23}} - \frac{\nu_{13}^2}{E_{11}}\right)} \tag{4-11}$$

$$\nu_{23} = \frac{2E_{11}k_T - E_{11}E_{22} - 4\nu_{13}^2 E_{22}k_T}{2E_{11}k_T} \tag{4-12}$$

$$d\varepsilon_{1_f} = \alpha_{1_f} dT \tag{4-13}$$

$$d\varepsilon_{3_f} = \alpha_{3_f} dT \tag{4-14}$$

$$a = \frac{\nu_{13_f}V_f + \nu_r(1 - V_f)}{E_{11_f}V_f + E_r(1 - V_f)} \tag{4-15}$$

$$d\varepsilon_2 = d\varepsilon_3 = d\varepsilon_{free_r} \tag{4-16}$$

$$d\varepsilon_r = \frac{d\varepsilon_2 - \left(d\varepsilon_{3_f} + \nu_{13_f} d\varepsilon_{1_f}\right)V_f + a d\varepsilon_{1_f} E_{11_f} V_f}{(1 + \nu_r)(1 - V_f) - aE_r(1 - V_f)} \tag{4-17}$$

$$d\varepsilon_1 = \frac{d\varepsilon_{1_f} E_{11_f} V_f + d\varepsilon_r E_r(1 - V_f)}{E_{11_f}V_f + E_r(1 - V_f)} \tag{4-18}$$

$$\varepsilon_{free_1}^i = d\varepsilon_1 + \varepsilon_1^{i-1} \tag{4-19}$$

$$\varepsilon_{free_2}^i = d\varepsilon_2 \left(\left(T^i - T_g^i\right) - \left(T^{i-1} - T_g^{i-1}\right)\right) + \varepsilon_2^{i-1} \tag{4-20}$$

$$\varepsilon_{free_3}^{i} = d\varepsilon_3 \left(\left(T^i - T_g^i \right) - \left(T^{i-1} - T_g^{i-1} \right) \right) + \varepsilon_3^{i-1} \tag{4-21}$$

where G is the shear modulus, k is the plane strain bulk modulus, k_T is the lamina's effective plane strain bulk modulus, E is the elastic modulus, ν is Poisson's ratio, V is the volume fraction, d is the derivative, ε is the free strain, α is the coefficient of thermal expansion (CTE), T is the composite's temperature, T_g is the composite's glass transition temperature, subscript 1 is the longitudinal fiber direction, 2 is the transverse fiber direction, 3 is the out-of-plane direction, f denotes the fiber, r denotes the resin, and i denotes a time-step. Terms without f or r subscripts correspond to bulk lamina properties. Throughout the lamina calculations, the following assumptions are made for T800S fiber properties: $E_{11_f} = 2.55 \times 10^{11}$ Pa, $E_{33_f} = G_{13_f} = 2.55 \times 10^{10}$ Pa, $\nu_{13_f} = 0.2$, $\nu_{23_f} = 0.25$, $V_f = 0.572$, α_{1_f} = -0.4 × 10^{-6}/°C, and α_{3_f} = 9.0 × 10^{-6}/°C.[66,97] Upon obtaining lamina properties, the defined layup is utilized to compute stiffness matrices of the laminate:[95]

$$[T] = \begin{bmatrix} \cos^2\theta & \sin^2\theta & 0 & 0 & 0 & 2\sin\theta\cos\theta \\ \sin^2\theta & \cos^2\theta & 0 & 0 & 0 & -2\sin\theta\cos\theta \\ 0 & 0 & 1 & 0 & 0 & 0 \\ 0 & 0 & 0 & \cos\theta & \sin\theta & 0 \\ 0 & 0 & 0 & -\sin\theta & \cos\theta & 0 \\ -\sin\theta\cos\theta & \sin\theta\cos\theta & 0 & 0 & 0 & \cos^2\theta - \sin^2\theta \end{bmatrix} \tag{4-22}$$

$$[T^*] = \begin{bmatrix} \cos^2\theta & \sin^2\theta & 0 & 0 & 0 & \sin\theta\cos\theta \\ \sin^2\theta & \cos^2\theta & 0 & 0 & 0 & -\sin\theta\cos\theta \\ 0 & 0 & 1 & 0 & 0 & 0 \\ 0 & 0 & 0 & \cos\theta & \sin\theta & 0 \\ 0 & 0 & 0 & -\sin\theta & \cos\theta & 0 \\ -2\sin\theta\cos\theta & 2\sin\theta\cos\theta & 0 & 0 & 0 & \cos^2\theta - \sin^2\theta \end{bmatrix} \tag{4-23}$$

$$[\bar{S}] = [T^*]^{-1} \cdot \begin{bmatrix} 1/E_{11} & -\nu_{12}/E_{11} & -\nu_{13}/E_{11} & 0 & 0 & 0 \\ -\nu_{12}/E_{11} & 1/E_{22} & -\nu_{23}/E_{22} & 0 & 0 & 0 \\ -\nu_{13}/E_{11} & -\nu_{23}/E_{22} & 1/E_{33} & 0 & 0 & 0 \\ 0 & 0 & 0 & 1/G_{23} & 0 & 0 \\ 0 & 0 & 0 & 0 & 1/G_{13} & 0 \\ 0 & 0 & 0 & 0 & 0 & 1/G_{12} \end{bmatrix} \cdot [T] \tag{4-24}$$

$$[\bar{Q}] = [\bar{S}]^{-1} \tag{4-25}$$

$$A_{ij} = \sum_{k=1}^{n} \left(\bar{Q}_{ij}\right)_k (h_k - h_{k-1}) \tag{4-26}$$

$$B_{ij} = \frac{1}{2} \sum_{k=1}^{n} \left(\bar{Q}_{ij}\right)_k (h_k^2 - h_{k-1}^2) \tag{4-27}$$

$$D_{ij} = \frac{1}{3} \sum_{k=1}^{n} \left(\bar{Q}_{ij}\right)_k (h_k^3 - h_{k-1}^3) \tag{4-28}$$

where $[T]$ is the stress-transformation matrix, $[T^*]$ is the strain-transformation matrix, θ is a rotation of the ply local axes (directions 1 and 2) with respect to the element local axes[66], $[\bar{S}]$ is the compliance matrix, $[\bar{Q}]$ is the stiffness matrix, A is the extensional stiffness matrix relating forces to midplane strains, D is the bending stiffness matrix relating moments to curvatures, and B is the coupling stiffness matrix linking extension and bending. Next, the laminate's effective extensional (E), shear (G), and bending (E_b) moduli throughout the defined cure cycle are computed:[94]

$$[a] = [A^{-1}] \tag{4-29}$$

$$[d] = [D^{-1}] \tag{4-30}$$

$$E_x = \frac{1}{a_{11} t_{lam}} \tag{4-31}$$

$$E_y = \frac{1}{a_{22} t_{lam}} \tag{4-32}$$

$$E_z = \frac{1}{a_{33} t_{lam}} \tag{4-33}$$

$$G_{yz} = \frac{1}{a_{44} t_{lam}} \tag{4-34}$$

$$G_{xz} = \frac{1}{a_{55} t_{lam}} \tag{4-35}$$

$$G_{xy} = \frac{1}{a_{66} t_{lam}} \tag{4-36}$$

$$E_{bx} = \frac{12}{d_{11} {t_{lam}}^3} \tag{4-37}$$

$$E_{by} = \frac{12}{d_{22} {t_{lam}}^3} \tag{4-38}$$

where x, y, and z are the longitudinal, transverse, and out-of-plane element directions. Process-induced lamina free strains are then related to residual laminate forces, moments, and strains throughout the cycle:

$$[\varepsilon_{123}] = [\varepsilon_{free_1} \quad \varepsilon_{free_2} \quad \varepsilon_{free_3} \quad 0 \quad 0 \quad 0]^T \tag{4-39}$$

$$\left[\varepsilon_{xyz}\right] = [T^*]^{-1} \cdot [\varepsilon_{123}] \tag{4-40}$$

$$[N] = t_{ply} \cdot [\bar{Q}] \cdot [\varepsilon_{xyz}] \tag{4-41}$$

$$z_i = t_{ply} \left(\frac{1-n}{2} + i \right) \tag{4-42}$$

$$[M] = z_i \cdot [N] \tag{4-43}$$

$$[\epsilon^0] = [\epsilon_x^0 \quad \epsilon_y^0 \quad \epsilon_z^0 \quad \gamma_{yz}^0 \quad \gamma_{xz}^0 \quad \gamma_{xy}^0]^T \tag{4-44}$$

$$[k^0] = [k_x^0 \quad k_y^0 \quad k_z^0 \quad k_{yz}^0 \quad k_{xz}^0 \quad k_{xy}^0]^T \tag{4-45}$$

$$\begin{bmatrix} \epsilon^0 \\ k^0 \end{bmatrix} = \begin{bmatrix} A & B \\ B & D \end{bmatrix}^{-1} \cdot \begin{bmatrix} N \\ M \end{bmatrix} \tag{4-46}$$

$$\epsilon_x^0 = \varepsilon_{free_x} \tag{4-47}$$

$$\epsilon_y^0 = \varepsilon_{free_y} \tag{4-48}$$

$$\epsilon_z^0 = \varepsilon_{free_z} \tag{4-49}$$

where $[\varepsilon_{123}]$ is the lamina free strains, $\left[\varepsilon_{xyz}\right]$ is the lamina free strains with respect to the laminate local axes, $[N]$ is the resultant free strain-induced laminate forces, t_{ply} is the ply thickness (0.191 mm)[36], n is the number of plies in the laminate determined from the layup, $[M]$ is the laminate moments, $[\epsilon^0]$ is the laminate midplane strains, and $[k^0]$ is the laminate curvatures at different

time-temperature increments. Finally, PIDs in L-shaped T800S/3900-2B parts are predicted by employing Takagaki et al.'s analytical solutions based on shear-lag analysis and Timoshenko beam theory:[28]

$$d\varepsilon_{free} = \frac{d\varepsilon_{free_z} - d\varepsilon_{free_x}}{1 + d\varepsilon_{free_x}} \tag{4-50}$$

$$a = \frac{1}{t}\sqrt{\frac{10G_{yz}}{E_{xb}}} \tag{4-51}$$

$$b_1 = \frac{1 + e^{2al_f}}{2aR(e^{2al_f}e^{al_1} + e^{-al_1})} \tag{4-52}$$

$$b_2 = \frac{1 + e^{-2al_1}}{2aR(e^{2al_f}e^{al_1} + e^{-al_1})} \tag{4-53}$$

$$l_1 = R\varphi \tag{4-54}$$

$$l_2 = l_f + R\varphi \tag{4-55}$$

$$d\theta = \begin{bmatrix} -d\varepsilon_{free} \times b_1(e^{al} - e^{-al}) & 0 \le l \le l_1 \\ -d\varepsilon_{free} \times b_2(e^{al} + e^{-al}e^{2al_2}) & l_1 \le l \le l_2 \end{bmatrix} \tag{4-56}$$

where $d\theta$ is the angular deformation of the L-shaped part, $d\varepsilon_{free_z}$ and $d\varepsilon_{free_x}$ are changes in through-thickness and in-plane free strains, G_{yz} is the part's through-thickness shear modulus, E_{xb} is the part's longitudinal bending modulus, l is the distance from the L-shape's corner, l_f is the flange length, R is the tool's corner radius, and φ is half of the tool's corner angle (**Figure 4-1**). By employing the solutions presented above, angular deformations in the composite part can be incrementally computed throughout the defined cure cycle. The part's final PIDs such as spring-in, warpage, and volumetric deformation can then be predicted using CHILE and geometric analyses.[64] Note that solutions presented ignore contributions from tool expansion, which may be an acceptable assumption in some scenarios, such as when Invar tooling is used.

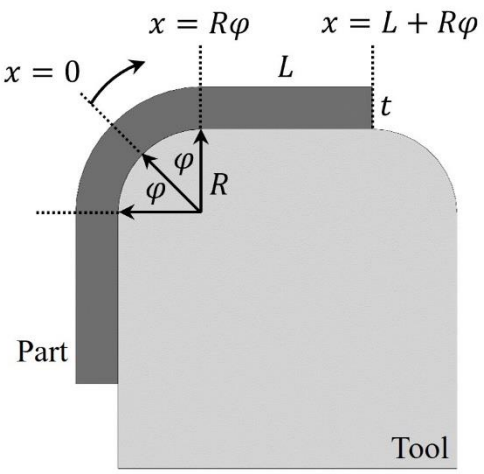

Figure 4-1. Schematic geometry of an L-shaped part on a tool.

The numerical simulation framework reveals a link between PIDs in L-shaped parts and two key properties of the composite material: the ratio of shear to bending modulus (G_{yz}/E_{xb}) and a ratio of through-thickness to in-plane free strains ($d\varepsilon_{free}$). While these relationships are well-established in current literature, their success in practical applications for advanced composites has been predominantly limited to geometric analyses, focusing on variabilities like part thickness or flange length, due to the absence of reliable material property models.[27] Consequently, a significant knowledge gap exists regarding how other process variables can contribute or dispute these relationships. This knowledge gap serves as the foundation for the remaining analyses in this chapter. Specifically, the following investigation explores how different layup and cure cycle procedures may impact thermo-mechanical properties and, consequently, dimensional changes of L-shaped T800S/3900-2B parts. It is important to note that the impacts of several processing variabilities (e.g., tool-part interaction, interply-toughened microstructures, etc.) on PIDs are neglected in the simulation framework.[21] Therefore, the data presented throughout this chapter primarily serves to guide future research aimed at understanding PIDs in advanced composites.

To begin the parametric investigations, several design spaces were constructed and evaluated using the FE simulation code. The initial focus was on exploring the impact of layup,

particularly asymmetry, on PIDs. This involved analyzing all cross-ply layups comprising eight plies, a flange length of 154.2 mm, a width of 50.8 mm, a corner radius of 15.875 mm, and a corner angle of 90° (**Figure 4-2**). Consequently, with only zero- and ninety-degree plies considered, a total of $2^8 = 256$ predictions of spring-in, warpage, and volumetric deformation were computed using the FE simulation. It is essential to note that while the ply configuration served as the independent processing variable, the primary objective of exploring this design space was to discover correlations between mechanical properties and PIDs. In other words, the investigation aimed not at identifying optimal cross-ply layups, but rather optimal stiffness properties (i.e., B_{11}) to potentially minimize PIDs. Additionally, note that the geometry of the parts was selected to allow for comparisons between numerical predictions and experimental results in later chapters.

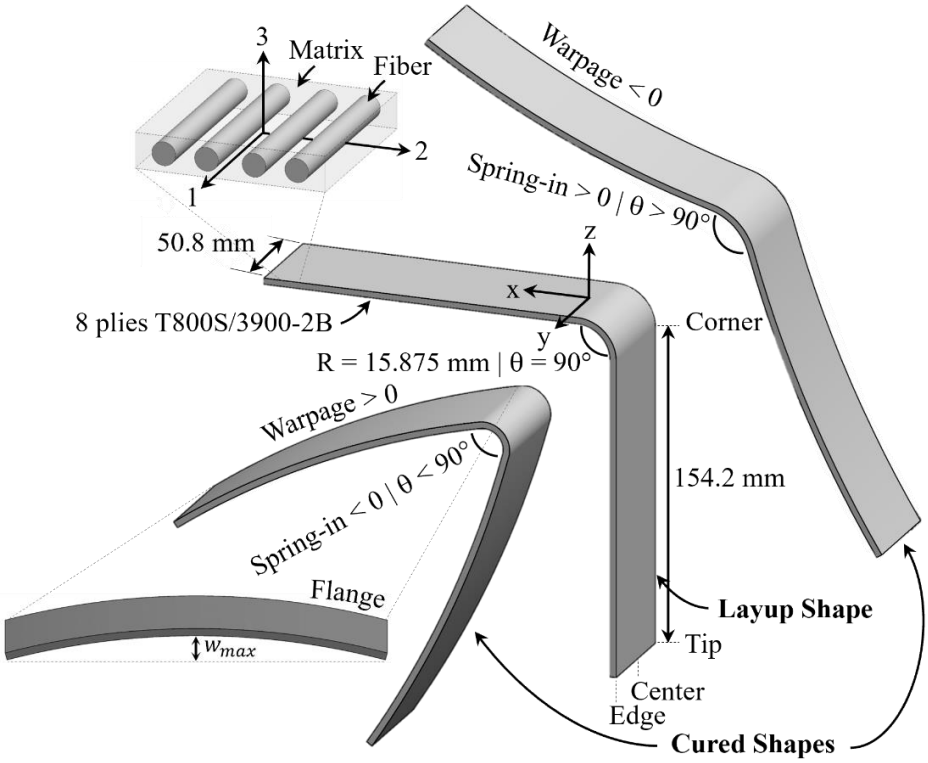

Figure 4-2. Geometry and terminology used for L-shaped PID analyses.

After layup analyses, further investigations were conducted focused on the potential impacts of cure cycle on thermo-mechanical and PID developments. Throughout these analyses,

various design spaces featuring temperature cycles inducing gelation and vitrification phase transformations in the composite under diverse thermal loading conditions were evaluated. The objective was to identify potential relationships between curing paths, temperature-dependent thermo-mechanical properties, and PID developments in T800S/3900-2B. Throughout these evaluations, the geometry of the L-shaped parts remained consistent with that of the layup investigations (**Figure 4-2**), while the ply configuration remained constant at $[0/90]_{2s}$.

Some final notes are that throughout the remainder of this work, positive spring-in values represent angle enlargements between flanges, whereas negative values represent angle enclosures. Likewise, positive and negative warpage values represent concave-down and concave-up flange distortions, respectively. Directions 1, 2, and 3 pertain to the longitudinal fiber, transverse fiber, and out-of-plane lamina dimensions (**Figure 4-2**). Lastly, directions x, y, and z are the longitudinal, transverse, and out-of-plane L-shaped laminate dimensions.

4.3 RESULTS AND DISCUSSIONS

4.3.1 Layup Investigations

Figure 4-3 and **Figure 4-4** illustrate the impacts of longitudinal bending modulus (E_{xb}), shear modulus (G_{yz}), and the in-plane/out-of-plane coupling coefficient (B_{11}) on corner spring-in and tip spring-in of L-shaped T800S/3900-2B parts. Each point in the plot corresponds to FE simulation outcomes for a cross-ply layup, with red points being layups resulting in negative spring-in values, blue points being positive spring-in, and the diameter of each point being proportional to the absolute magnitude of the PIDs. The figures demonstrate strong correlations between E_{xb} and the spring-in of L-shaped parts. Generally, laminates with higher longitudinal bending modulus due to a greater proportion of zero-degree plies and fibers aligned along the flange direction, exhibit lower spring-in at the corner and tip. This behavior can be attributed to

the relatively stiff fibers offering greater resistance to deformation upon demolding, a phenomenon accounted for in the theoretical framework utilized for spring-in predictions.[28,94]

The plots also reveal some direct yet weaker correlations between G_{yz} and spring-in. For example, laminates with lower through-thickness shear moduli demonstrate decreased spring-in only within certain regions. These trends emerge because lower shear moduli enable the alleviation of residual stresses through interply slippage, a factor also accounted for in the simulation framework.[28] However, it is important to acknowledge that these correlations lack global consistency in the plots due to the simplicity of the cross-ply design space. Since laminates with only zero- and ninety-degree plies were evaluated, differences in G_{yz} often coincided with significant adverse changes in E_{xb}, leading to counteracting effects on spring-in.

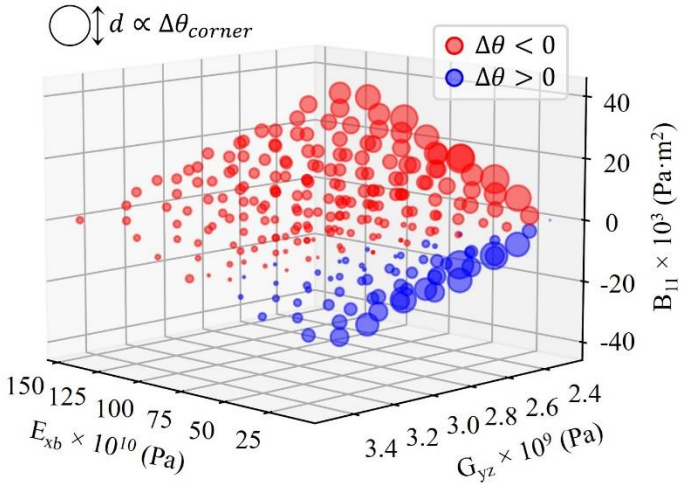

Figure 4-3. Effects of longitudinal bending modulus, through-thickness shear modulus, and in-plane/out-of-plane coupling on corner spring-in angle of L-shaped T800S/3900-2B parts.

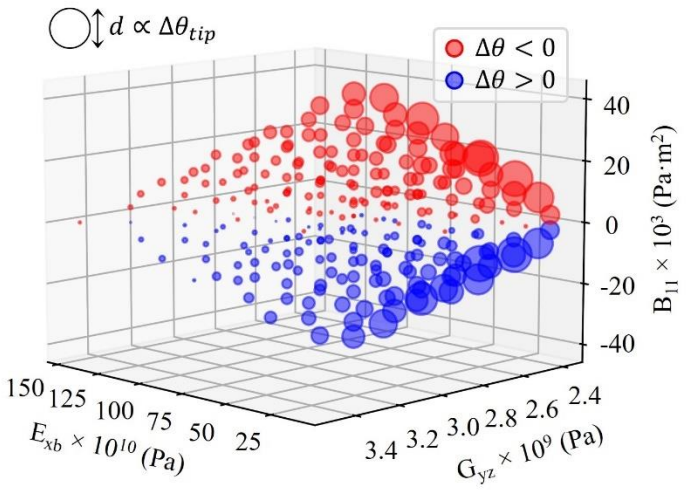

Figure 4-4. Effects of longitudinal bending modulus, through-thickness shear modulus, and in-plane/out-of-plane coupling on tip spring-in angle of L-shaped T800S/3900-2B parts.

Figure 4-3 and **Figure 4-4** also highlight intriguing connections between the in-plane/out-of-plane coupling coefficient and the spring-in behavior of L-shaped parts. Most notably, the distinction between positive and negative spring-in values is closely linked to the sign of B_{11}, with positive spring-in only occurring for negatively coupled laminates. The B_{11} values signify the direction and magnitude each laminate will deform in the out-of-plane direction in response to in-plane strain.[95] For instance, an L-shaped laminate with a negative B_{11} implies that in-plane compression during processing would result in concave-down flange distortion upon demolding and thus negative warpage. These patterns are evident in **Figure 4-5**, where all laminates with negative B_{11} also exhibit negative out-of-plane deformation. During manufacturing, these effects would force an L-shape's flanges to distort outwards at the corners and tips, often leading to positive spring-in (**Figure 4-2**).

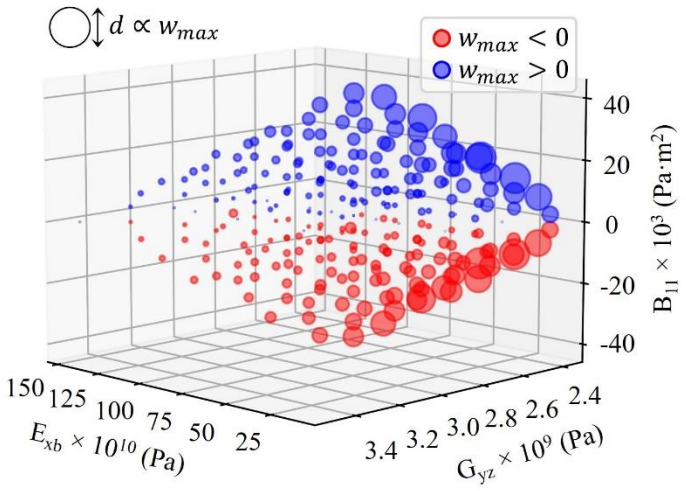

Figure 4-5. Effects of longitudinal bending modulus, through-thickness shear modulus, and in-plane/out-of-plane coupling on maximum flange warpage of L-shaped T800S/3900-2B parts.

Within the cross-ply design space, the sign and magnitude of B_{11} are directly connected with each laminate's degree of through-thickness asymmetry. Negative coupling coefficients are indicative of laminates with a larger moment of ninety-degree lamina above the midplane, considering both the number of plies and their distance from the center.[95] Laminates with the smallest (i.e., most negative) B_{11} values are highly asymmetric, with fibers predominantly oriented transversely above and longitudinally below the midplane (e.g., $[0_4/90_4]$). Thus, **Figure 4-3** demonstrates that the absolute corner spring-in of L-shaped parts can potentially be minimized by utilizing layups with above-midplane-transverse asymmetry to attain negative coupling. However, manufacturers should be cautious when employing such methods, as excessive asymmetry can lead to significant increases in warpage (**Figure 4-5**), tip spring-in (**Figure 4-4**), and thus overall deviation from the layup shape (**Figure 4-6**).

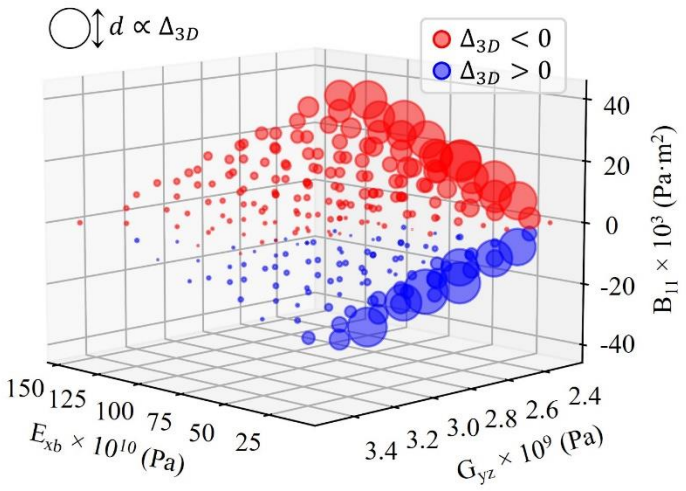

Figure 4-6. Effects of longitudinal bending modulus, through-thickness shear modulus, and in-plane/out-of-plane coupling on volumetric deformation of L-shaped T800S/3900-2B parts.

Figure 4-7 illustrates the directional stiffnesses and coupling coefficients for ten cross-ply laminates that produced the lowest volumetric deformation throughout the simulation campaign. **Table 4-1** provides the corresponding layup, spring-in, and warpage of each L-shaped part. The plot and table demonstrate that all minimally deformed laminations had negative B_{11} values, reinforcing the potential effectiveness of imposing transverse asymmetry for PID mitigation. It is worth noting that while other laminations displayed lower spring-in values than those listed in **Table 4-1**, they were highly asymmetric, resulting in elevated warpages and volumetric deformations. These findings also highlight the value of assessing PIDs volumetrically rather than relying solely on point values like spring-in, as traditionally done.[98]

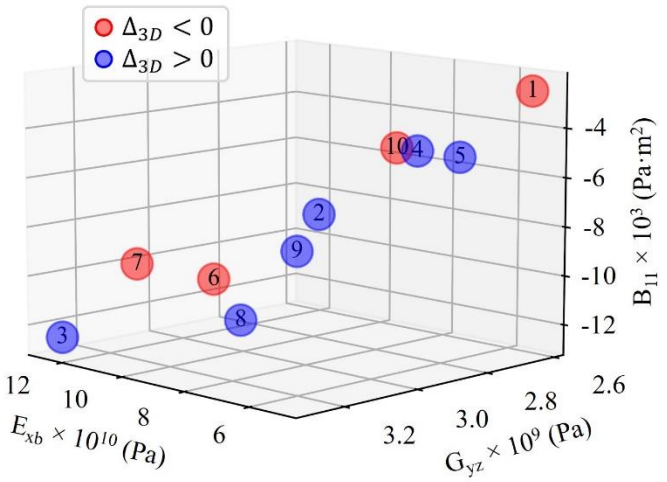

Figure 4-7. Laminations producing minimal volumetric deformation in L-shaped parts.

Table 4-1. Layups of laminations producing minimal deformation in L-shaped parts.

ID	Layup	B_{11} (Pa·m^2)	$\Delta\theta_{corner}$ (°)	$\Delta\theta_{tip}$ (°)	w_{max} (mm)	Δ_{3D} (cm^3)
1	[90/0/90/0/90/90/0/90]	-2503	-0.91	3.72	-0.80	-0.11
2	[0/90/0/0/90/0/0/90]	-7509	-0.79	4.99	-1.00	0.27
3	[0/0/0/0/0/0/90/0]	-12515	-0.46	6.71	-1.23	0.27
4	[0/90/90/0/0/90/0/90]	-5006	-0.83	4.57	-0.94	0.27
5	[90/0/0/90/0/90/0/90]	-5006	-0.76	5.84	-1.13	0.35
6	[0/0/90/0/0/0/0/90]	-10012	-0.76	5.20	-1.03	-0.40
7	[0/0/0/90/0/0/90/0]	-10012	-0.78	4.36	-0.89	-0.42
8	[0/0/90/0/0/90/90/0]	-12515	-0.57	7.41	-1.37	0.47
9	[0/0/90/90/0/90/90/0]	-10012	-0.60	6.92	-1.29	0.50
10	[90/0/0/0/90/90/90/0]	-5006	-0.86	4.09	-0.86	-0.54

If a manufacturer's aim is to minimize the total (i.e., volumetric) deformation of L-shaped parts, it is apparent that inducing transverse asymmetry at the laminate's corner may be advantageous. However, a challenge then lies in avoiding warpage in the flange that accompanies this asymmetry. One potential solution could involve inserting transverse plies as patches only covering the corner region, as schematically illustrated in **Figure 4-8**. By maintaining a relatively symmetric layup for the rest of the L-shape, warpage in the flange could be minimized, consequently reducing the part's overall PIDs. This proposed solution is beyond the scope of this study and warrants investigation in future research.

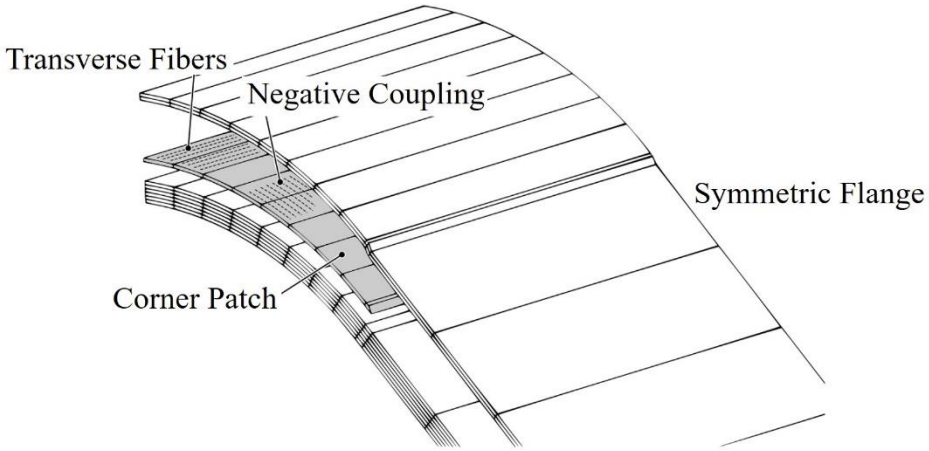

Figure 4-8. Schematic of potential asymmetric patch solution to minimize PIDs in L-shaped composite parts.[99]

4.3.2 Cure Cycle Investigations

Figure 4-9 depicts temperature (T) and degree of cure (DoC) profiles for various isothermal cure cycles employed to investigate the potential effects of cure temperature on PIDs of L-shaped T800S/3900-2B parts, assuming the part's layup cannot be altered during manufacturing. In each cycle, the temperature increases from 20 °C to an elevated temperature at a rate of 2 °C/min, held until the composite reaches an approximate DoC of 90%, and subsequently cooled to room temperature. Throughout the investigations, isothermal dwell temperatures were limited to values above 160 °C, as temperatures below this threshold cannot be utilized to achieve the desired DoC in T800S/3900-2B. Additionally, it is worth noting that the isothermal cycle at 180 °C is equivalent to the Manufacturer's Recommended Cure Cycle (MRCC).[36]

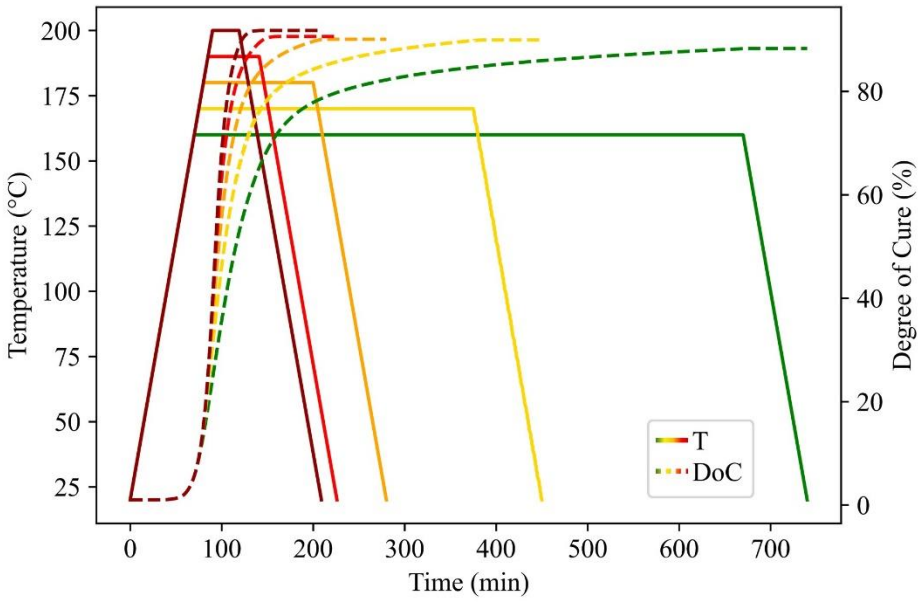

Figure 4-9. Temperature and degree of cure profiles of cycles employed for investigating the impacts of isothermal cure temperature on PIDs of L-shaped parts.

Figure 4-10a depicts the progression of thermo-mechanical properties in a symmetric cross-ply T800S/3900-2B laminate throughout the isothermal temperature cycles presented in **Figure 4-9**. The axes of the plot represent the curing temperature, a ratio of through-thickness to in-plane free strains during processing, and the ratio of through-thickness shear modulus to longitudinal bending modulus. As previously mentioned, these two thermo-mechanical ratios are known to have direct correlations with PIDs of L-shaped parts.[28] In **Figure 4-10b**, the bars illustrate the predicted tip spring-in of L-shaped parts based on these thermo-mechanical properties, while the points indicate the percentage change relative to the 180 °C MRCC.

The plots in **Figure 4-10** reveal a balance between the isothermal hold temperature, thermo-mechanical evolutions, and PIDs of L-shaped T800S/3900-2B parts. Throughout each cycle's isothermal dwell, temperature-dependent changes in thermo-mechanical properties occur. For example, while in-plane free strains (ε_{free_x}) remain relatively insignificant, through-thickness free strains (ε_{free_z}) evolve more rapidly at lower temperatures (**Figure 2-35**). Additionally, since

the through-thickness shear modulus (G_{yz}) is significantly influenced by the resin's cure state, the ratio of shear to bending modulus (E_{xb}) also progresses at a rate inversely related to temperature (**Figure 2-32**).

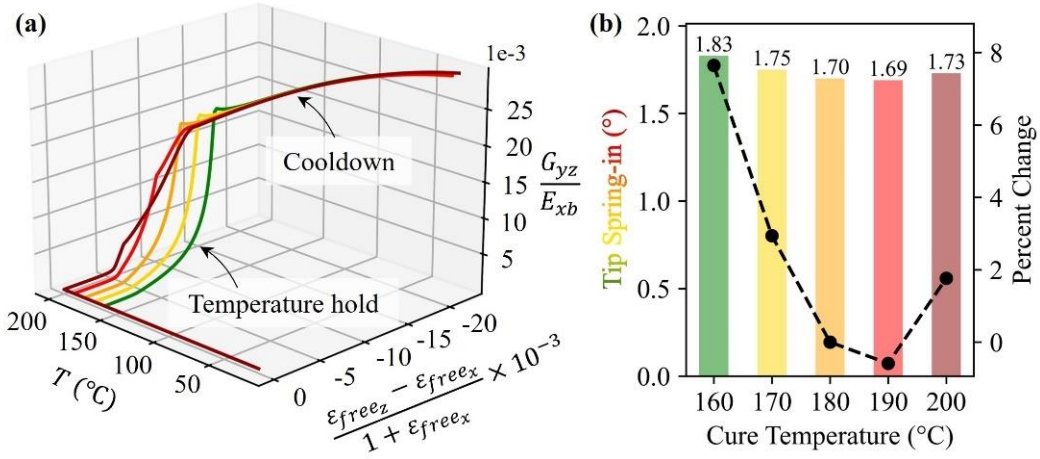

Figure 4-10. (a) Evolution of thermo-mechanical properties in a symmetric cross-ply T800S/3900-2B laminate throughout different isothermal cure cycles, and **(b)** the resulting tip spring-in of an L-shaped part.

These trends suggest potential advantages of employing higher curing temperatures to reduce PID-contributing mechanical properties and residual stresses during the vitrification process. However, these potential benefits are likely diminished during the cooldown phase, as higher cooling ranges induce more significant thermo-elastic effects. Consequently, upon reaching room temperature, the thermo-mechanical ratios established during higher-temperature isothermal holds closely align with those from lower-temperature cycles.

Figure 4-10b demonstrates that the lowest tip spring-in was predicted for the 190 °C isothermal cycle, suggesting that this temperature may offer a slightly more optimal balance of thermo-mechanical effects during curing and cooldown compared to the MRCC. It should be noted that these effects would likely play a significant role in the prepreg's VE contribution to tool-part interaction (**Figure 2-44**), which is neglected in the simulation. Hence, the balance between cure temperature, thermo-mechanical evolutions, and PIDs prompts investigation in future research.

Figure 4-11 presents the processing temperature (T) and glass transition temperature (T_g) of T800S/3900-2B over various two-hold cure cycles, where it is again assumed that the part's layup cannot be altered. These cycles were specifically designed to initiate gelation and vitrification in the prepreg at different temperatures, and to explore the effects on thermo-mechanical properties and PIDs. In each cycle, the temperature first rises from 20 °C to an elevated level at a rate of 2 °C/min. The temperature is then maintained until the prepreg reaches full vitrification ($T_g > T + 28$ °C).[62,63] Then, the processing temperature is increased to 180 °C at 0.1 °C/min, held for 120 minutes to reach an approximate DoC of 90%, then cooled to room temperature. Throughout each cycle, the second heat-up rate of 0.1 °C/min was employed to ensure that T_g remains well above the processing temperature to prevent the composite from devitrifying.

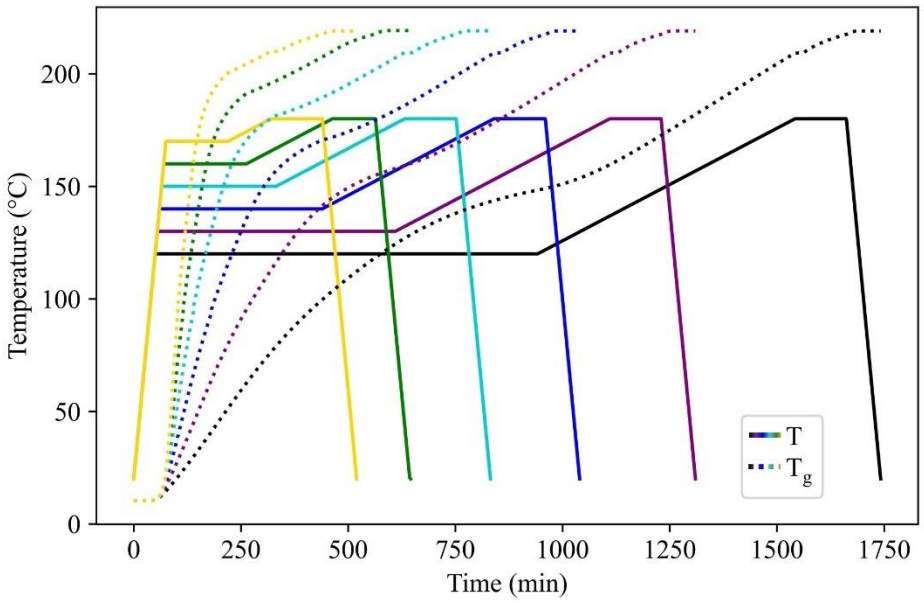

Figure 4-11. Processing and glass transition temperatures employed for investigating the impacts of gelation and vitrification temperatures on PIDs of L-shaped T800S/3900-2B parts.

In **Figure 4-12a**, the advancement of thermo-mechanical properties in a symmetric cross-ply T800S/3900-2B laminate is displayed across the two-hold temperature cycles presented in **Figure 4-11**. **Figure 4-12b** displays the projected tip spring-in of L-shaped parts based on these

thermo-mechanical properties, and the percentage change relative to the one-hold 180 °C MRCC cycle. The figures reveal correlations between the intermediate-hold and vitrification temperature and the resulting tip spring-in of L-shaped parts. At the lowest intermediate hold temperatures (120 – 140 °C), cross-linking triggers rapid through-thickness free strain and moduli developments while the thermoplastic tougheners exist in their glassy state. Consequently, PID-contributing thermo-mechanical ratios are elevated and the composite's capacity for viscoelastic stress alleviation is relatively limited. Conversely, temperatures above 150 °C initiate cross-linking when the thermoplastic particles are rubbery, resulting in reduced shrinkage and stiffnesses, and a greater potential for stress alleviation. These phenomena collectively lead to the highest tip spring-in for cycles with the lowest intermediate hold temperatures. Additionally, the findings in **Figure 4-12b** suggest that the one-hold MRCC cycle appears to be a preferable option compared to the two-hold cycles when considering PIDs. However, the two-hold cycle configuration may provide other benefits such as reducing the porosity, which is not considered in this study.

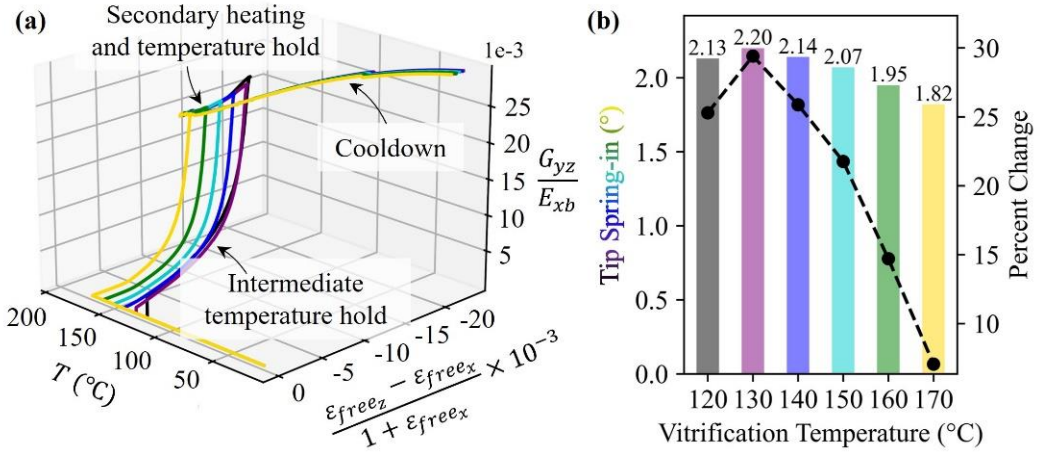

Figure 4-12. (a) Evolution of thermo-mechanical properties in a symmetric cross-ply T800S/3900-2B laminate throughout different two-hold cure cycles, and **(b)** the resulting tip spring-in of an L-shaped part.

If a manufacturer's goal is to minimize PIDs in L-shaped parts, the results in **Figure 4-12** suggest that inducing gelation and vitrification in the prepreg at low temperatures may be

detrimental. However, consider that in the two-hold cycles, the composite forms interfacial bonds with the tool during the initial low-temperature hold.[21] Subsequently, during the second slow heat-up stage, thermal expansion of the tool coupled with interfacial sticking/friction would enable the prepreg's tool-adjacent plies to stretch and transfer positive in-plane strain (ε_{free_x}) to the rest of the laminate. These phenomena may significantly reduce the through-thickness to in-plane strain ratio, potentially mitigate residual stresses and PIDs, and may be investigated in future research.

Figure 4-13 illustrates the processing temperature (T) and glass transition temperature (T_g) of T800S/3900-2B over various two-hold cure cycles initiating gelation, vitrification, and devitrification in the prepreg at different temperatures. In each cycle, the temperature first rises from 20 °C to an elevated level at a rate of 2 °C/min, then is held until the prepreg reaches full vitrification ($T_g > T + 28$ °C).[62,63] The processing temperature is then increased to 180 °C at 5 °C/min, held there for 120 minutes to reach an approximate DoC of 90%, then cooled to room temperature. Throughout each cycle, the second heat-up rate of 5 °C/min was employed to ensure that the processing temperature surpasses the prepreg's instantaneous T_g, thereby initiating devitrification and a second vitrification phase transformation at 180 °C.

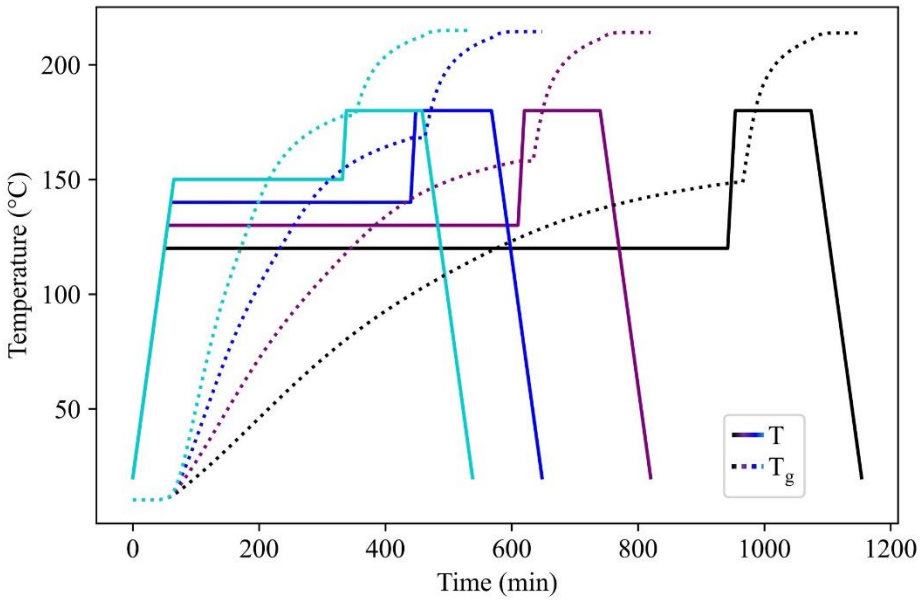

Figure 4-13. Processing and glass transition temperatures of cycles employed for investigating the impacts of devitrification on PIDs of L-shaped T800S/3900-2B parts.

In **Figure 4-14a**, the progression of thermo-mechanical properties in a symmetric cross-ply T800S/3900-2B laminate is displayed across the two-hold temperature cycles presented in **Figure 4-13**. **Figure 4-14b** displays the simulated tip spring-in of L-shaped parts based on these thermo-mechanical properties, and the percentage change relative to the one-hold 180 °C cycle. The figures suggest potentially significant impacts on PIDs resulting from devitrification. Following the initial temperature dwell and vitrification, the subsequent rapid heat-up causes the processing temperature to surpass the glass transition temperature of the composite, transforming the prepreg back to its rubbery structure. This rubbery transition is accompanied by thermal expansion which counteracts against the built-up cure shrinkage-induced strains and may alleviate much of the L-shape's geometric constraints. Subsequently, upon reaching a processing temperature of 180 °C, free strain and modulus ratios evolve once more, however less rapidly, owing to the temperature-dependent nature of the prepreg.

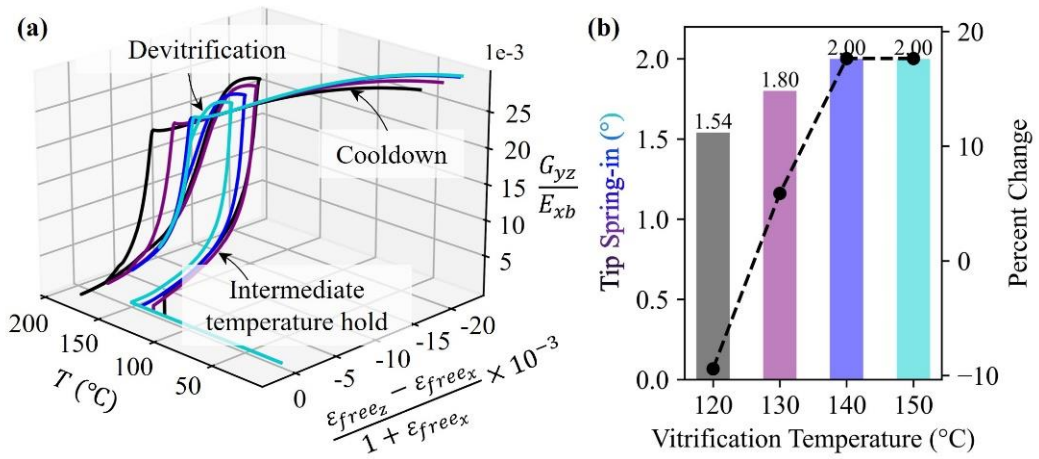

Figure 4-14. (a) Evolution of thermo-mechanical properties in a symmetric cross-ply T800S/3900-2B laminate throughout different two-hold cure cycles inducing devitrification, and **(b)** the resulting predicted tip spring-in of an L-shaped part.

The trends in **Figure 4-14** indicate potential benefits of inducing devitrification in the prepreg during the curing process. However, it is important to reconsider that in the two-hold cycles, the composite would lose its interfacial bond with the tool during the second heat-up stage upon devitrifying. As a result, interfacial friction and subsequent ply stretching due to tool thermal expansion effects would be minimal. These phenomena warrant further investigation in future research, either through experimental methods or by enhancing numerical simulation capabilities to include such effects.

4.4 SUMMARY

In this chapter, a numerical investigation into the impacts of several processing variabilities on PIDs of L-shaped composite parts was conducted. Thermo-mechanical property models established earlier in this study were incorporated into a customized finite element (FE) simulation code to efficiently assess the impacts of different layups and cure cycles. One notable discovery was that the spring-in of L-shaped parts can likely be minimized by employing asymmetric layups with negative in-plane/out-of-plane coupling coefficients (B_{11}). During manufacturing, optimal coupling properties can be achieved by orienting fibers transversely above the part's midplane

rather than below it. Cure cycles that induce vitrification and devitrification at distinct temperatures also hold promise at reducing PIDs and warrant investigation in future research.

5. EFFICIENT ANALYSIS OF PROCESS-INDUCED DEFORMATIONS USING MULTI-FIDELITY SIMULATION AND THEORY-GUIDED PROBABILISTIC MACHINE LEARNING

5.1 BACKGROUND

Although the previous chapter demonstrated that the impacts of processing variabilities on PIDs can be broadly assessed, minimizing undesired deformations via process optimization remains challenging. These difficulties primarily stem from limitations of methods traditionally used for PID predictions, typically classified into three categories, as depicted in **Figure 5-1**: low-fidelity simulation, high-fidelity simulation, and experimentation. One notable constraint of these methods is the trade-off between fidelity/accuracy and time/cost.[100]

At the bottom end of the cost/accuracy spectrum, low-fidelity simulation methods, including analytical solutions and/or reduced-order (i.e., 1D/2D) FE tools, often provide rapid and easy-to-interpret analyses while requiring relatively low material characterization and computational efforts.[19,28,101] However, as demonstrated in the previous chapter, many of these approaches often fail to describe complex processing phenomena (e.g., tool-part interaction[21]), leading to deviations from reality. Positioned in the middle, high-fidelity simulation methods (i.e., 3D FE), often provide more precise predictions but require substantially higher time commitments for material characterization, calibration, and validation.[26,33,60,66,102,103] Moreover, despite their improved accuracy, high-fidelity simulations typically neglect processing uncertainty and are impractical for optimization problems with large design spaces due to higher computational requirements. At the highest cost/accuracy level lies experimentation, involving the hands-on

manufacturing and analysis of composites. This approach offers several advantages, including the ability to bypass material characterization and capture the probabilistic nature of composites, but can be extremely time-consuming and expensive for large-scale composite structures.

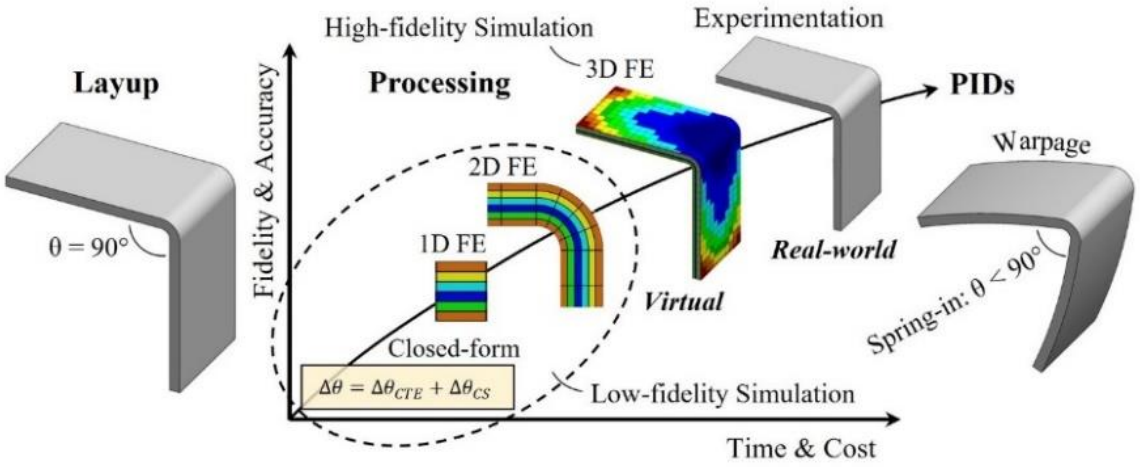

Figure 5-1. Schematics of process-induced deformations (PIDs) in an L-shaped composite part and the trade-off between time/cost and fidelity/accuracy in analysis methods.

The cost/accuracy trade-offs pose a dilemma for manufacturers when selecting methods to predict process phenomena and outcomes. One common strategy involves generating an extensive set of simulation data (Chapter 4) alongside a smaller experimental dataset. Attempts are then made to calibrate the simulations by connecting virtual and real-world domains using deterministic methods (e.g., least-squares). However, due to the difficulties and expenses in obtaining large data, the virtual-to-real connection and calibration attempts often rely on suboptimal amounts of data, leading to inaccurate manufacturing assessments and inefficient process optimization attempts.

Given the outlined challenges, there exists an opportunity to explore alternative and more efficient PID prediction and composites process analysis approaches. This chapter introduces one such approach based on theory-guided machine learning (TMGL). The effectiveness of the TGML method is assessed by predicting PIDs of L-shaped T800S/3900-2B parts. The strategies presented

offer an alternative, cost-efficient, and broadly applicable framework for solving manufacturing problems of composites using multi-fidelity simulation and limited experimental data.

5.2 METHODS

5.2.1 Low-fidelity Simulation

In this section, the low-fidelity numerical model for predicting PIDs is reiterated, drawing on an analytical strategy from Takagaki et al. and employed in the previous chapter.[28] The model uses the in-situ shear and bending moduli of a laminate, free strains, and geometric parameters of L-shaped parts as inputs to estimate incremental stresses and deformations during processing. Input properties were derived by simulating the degree of cure (DoC) and glass transition temperature (T_g) throughout the MRCC using a well-established cure kinetics model[63], then computing thermo-mechanical properties from models developed in Chapter 2.[60] The CHILE integration scheme was then applied to predict the final corner spring-in, tip spring-in, and maximum warpage of the L-shaped parts.

5.2.2 High-fidelity Simulation

This section presents a high-fidelity simulation approach for predicting PIDs. Since the method is well-established and validated, only a brief overview is provided, while a more detailed description can be found in work published by Zappino et al.[104] This high-fidelity scheme utilizes a refined 1D kinematic model rooted in the Carrera Unified Formulation (CUF) and CHILE assumptions, for efficient layer-wise (LW) modeling and accurate 3D representations of residual stresses and PIDs.[66,103,105] The model utilizes bending and shear moduli (E and G), Poisson's ratio (ν), coefficient of thermal expansion (CTE), and free strains (ε_{free}) in each of the three principal directions, sourced from published literature and the results from one BMB validation test (**Figure**

2-29).[36,63,104,106] After each high-fidelity simulation, geometric analyses were performed to derive corner spring-in, tip spring-in, and maximum warpage at the center and edge of each laminate.

5.2.3 Experimentation

Each experimental test in this chapter consisted of laying up three L-shaped composite parts with identical layups and curing them in an autoclave. Three parts were fabricated during each experiment to obtain a statistically robust dataset with built-in material and process variabilities, facilitating a probabilistic assessment of the effects on PIDs. The setups and steps employed during each experiment are shown in **Figure 5-2**. First, a custom-shaped tool made of 6.35 mm-thick A-36 steel was covered with one layer of FEP release film. FEP was used to minimize tool-part interaction during processing and thus its effects were neglected in this study.[21] Next, three L-shaped laminates consisting of eight T800S/3900-2B plies were laid up, equally spaced across the width of the tool. Each L-shaped part had a flange length of 154.2 mm, a width of 50.8 mm, a corner radius of 15.875 mm, and a corner angle of 90° (**Figure 4-2**). Then, the tool and composite laminates were covered with another sheet of FEP and one layer of breather cloth. Finally, the system was sealed in vacuum bagging, loaded into an autoclave, and subjected to the MRCC for curing.[36]

After each autoclave cycle, the cured L-shaped parts were demolded from the tool and excess resin bleed was carefully trimmed from the edges using an X-ACTO knife. The parts were then placed on their sides and a Keyence LJ-X8400 laser scanner was used to generate two-dimensional profiles at three locations spaced across the width of each part. The laser scanner was installed on a custom mechanical gantry system to ensure precise and consistent measurements for each trial. One profile was scanned just inside each edge and one profile was captured at the center of each part, as illustrated on the righthand side of **Figure 5-2**. Following the scans, profiles were

overlaid onto plots featuring the premeasured tool profile at the respective location. A custom Python code was then used to extract spring-in and warpage values at the center and edges of each part.[92]

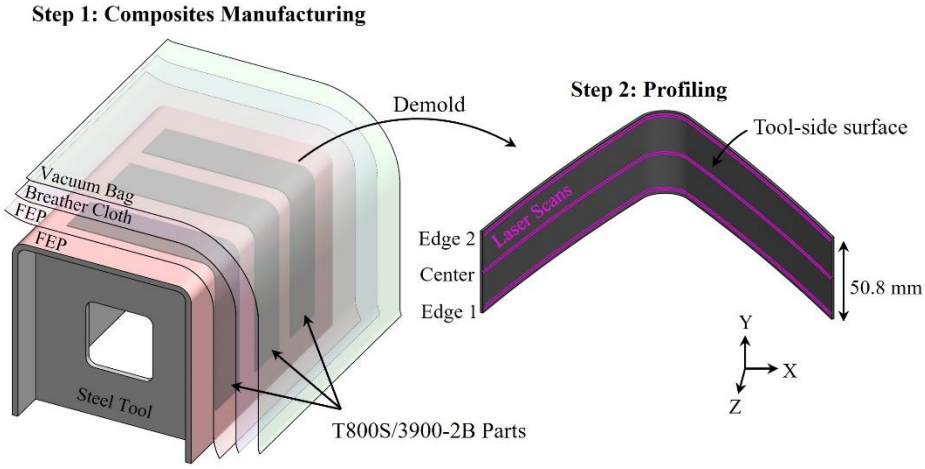

Figure 5-2. Setups for fabricating and profiling L-shaped composite parts.

5.2.4 TGML Prediction Methodology

In this section, a novel methodology for efficient prediction of PIDs and analysis of composites manufacturing phenomena using multi-fidelity simulation data, experimental data, and TGML is presented.[91,100,107–110] This chapter focuses on introducing the method through a relatively simple case study of predicting PIDs for L-shaped parts with eight-ply layups comprised solely of zero- and ninety-degree plies, cured according to the MRCC. The outlined procedures are designed to be general, allowing for potential expansion to include other manufacturing methods and variables.

The prediction process, schematically outlined in **Figure 5-3**, starts with generating low-fidelity simulation data for a design space, as outlined in Sections 4.2 and 5.2.1. Focusing on eight-ply cross-ply layups, simulations were conducted for $2^8 = 256$ potential laminates with zero- and ninety-degree plies. Utilizing the low-fidelity scheme, predictions for corner spring-in, tip spring-

in, and maximum warpage were efficiently obtained in approximately 24 minutes on a standard desktop.

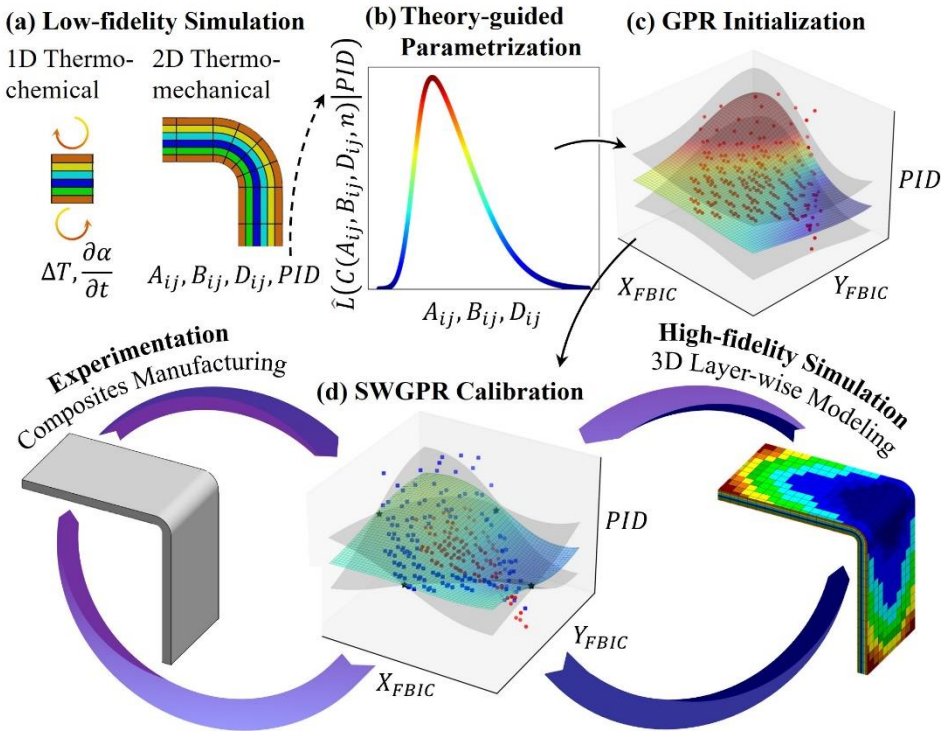

Figure 5-3. Flowchart of efficient PID prediction method using multi-fidelity simulation and theory-guided machine learning (TGML).

After constructing the low-fidelity dataset, initialization of predictive models for each PID type (i.e., corner spring-in, tip spring-in, and warpage) begins. To start this process, numerical values serving as parametric inputs for each lamination must be obtained. Closed-form physical theories are utilized for this task to ensure smoothness in the predictive model and provide physics-based "guidance" to the domain.[91,100,107,109] In this study, parametrization was achieved using Classical Laminated Plate Theory (CLPT), leveraging established connections between stiffnesses and PIDs of composites.[19,28,101,111] Employing CLPT and publicly available material properties, all elements of the extensional (A), coupling (B), and bending stiffness (D) matrices were

computed for each laminate.[36,63,104,106] This yielded a high-dimensional dataset of 27 stiffness coefficients and three PID predictions (i.e., corner spring-in, tip spring-in, and warpage).

Training a model on a highly parametrized design space with a large input-to-output ratio is prone to overfitting, computationally demanding, and challenging in terms of interpretation. To address these constraints, input parameters must be refined to an optimal number. This task was accomplished using a strategy inspired by Schwarz[112] and Claeskens and Hjort[113], termed Focused Bayesian Information Criterion (FBIC). To balance accuracy and interpretability of the model, the Bayesian Information Criterion (BIC), a well-established parameter selection method, is employed.[113] BIC assesses the appropriateness of input subsets by maximizing the likelihood function on the training data and penalizing the number of parameters to prevent overfitting. To consider computational time, an additional term is introduced, creating a custom parameter selection method, the FBIC:

$$FBIC = -2\ln(\hat{L}) + kt\ln(n) \tag{5-1}$$

where $\hat{L}$ is the model's maximized likelihood function (~ accuracy on training data), k is the number of parameters, n is the number of datapoints, t is the computational time needed for model training, and models with lower FBIC values are preferred.

Applying (5-1) and enforcing the constraint $k = 3$ to allow the models to be interpretable as 3D surfaces, GPR training was conducted on various two-input parameter subsets (e.g., A_{11} and B_{22}) to predict simulated PIDs. During GPR fitting, the underlying function is predicted as the mean of a distribution over functions that is dependent on the values of inputs, outputs, and Gaussian measurement noise (i.e., uncertainty). This initial GPR training phase was completed using a summation of the Radial Basis Function (RBF) and white noise kernels in Python's scikit-learn library.[92,93]

With 27 potential input parameters, there were 351 potential subset combinations for each PID output, all of which GPR modeled in approximately four minutes. Afterward, using (5-1), the FBIC was computed for each model. The two-parameter input subset yielding the lowest FBIC was considered optimal, leading to the exclusion of the remaining 25. It is critical to note that input parameter subsets were not equally optimal for all three PID types and thus the process was repeated to build GPR models for each.

After constructing GPR models, a calibration process begins by iteratively replacing low-fidelity simulation data with high-fidelity simulation and experimental data. This process was guided by assigning noise levels to different data types in the model based on the proximity of low- and high-fidelity simulation points to the experimental data. This approach enables the GPR model to consider data from various sources differently, placing greater "trust" in and near experimental points. Conversely, in regions lacking experiments, the model exhibits heighted uncertainty. This establishes a GPR model with a spatially weighted uncertainty structure, termed Spatially Weighted Gaussian Process Regression (SWGPR).

To illustrate the SWGPR approach, consider a simple space with data from one experiment and one lower-fidelity virtual source, where the outputs (e.g., PIDs) are assumed to be a function of some arbitrary parameter (**Figure 5-4a**). Similar to assuming that PID magnitudes are alike for nearby inputs, a smoothness in noise or uncertainty can also be assumed. To incorporate this, as the distance between a lower-fidelity and experimental datapoint increases, the influence or weight of the low-fidelity point on the model's predictions decreases following a Gaussian distance-decay function:

$$w_{ij} = e^{-d_{ij}^2/2\left(h \times d_{ij,max}\right)^2} \tag{5-2}$$

where w_{ij} is the weight of each lower-fidelity datapoint, d_{ij} is the Euclidean distance between a lower-fidelity and experimental datapoint, h is a decay factor influencing the rate of weight decay, and $d_{ij,max}$ is the maximum distance between two datapoints in the domain.

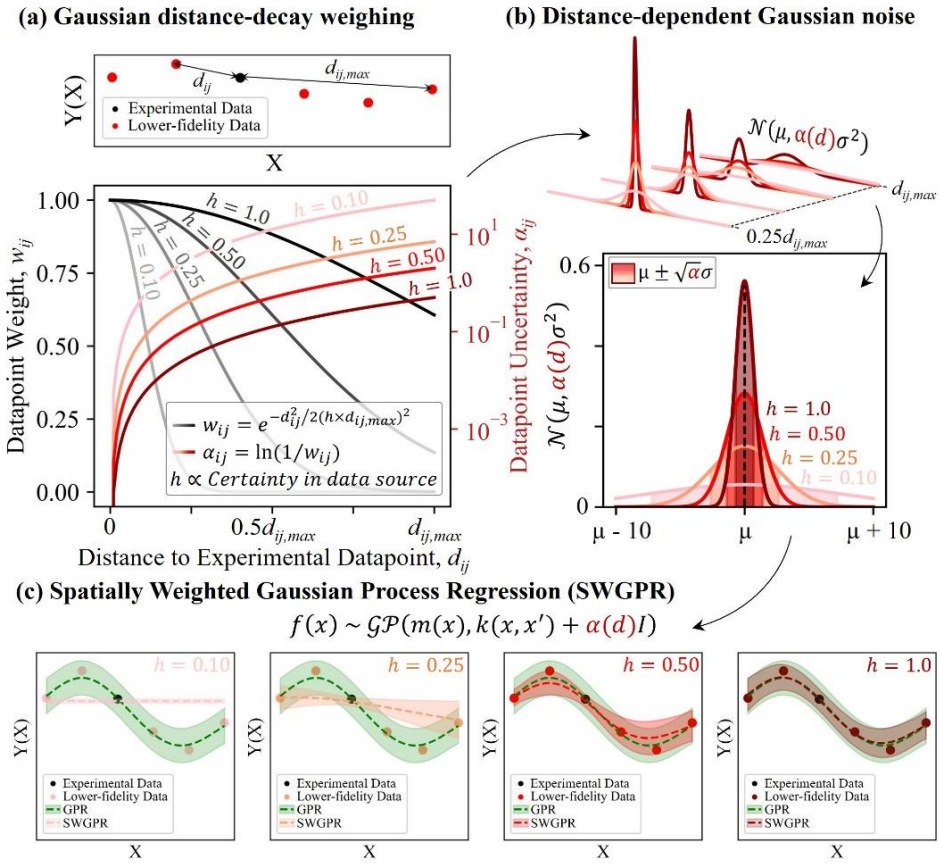

Figure 5-4. (a) Gaussian distance-decay weight and uncertainty, **(b)** Gaussian noise, and **(c)** SWGPR predictions for different uncertainty levels in a lower-fidelity data source.

Figure 5-4a illustrates the Gaussian distance-decay function for various h values, where the magnitude is a direct reflection of the uncertainty in a data source. If there is high uncertainty in modeling, material properties, or other variables, this knowledge can be implemented by specifying a smaller h value. Once weights are determined, a distance-weighted sum is calculated when multiple experimental points are present. These weights are then directly translated into noise levels using the following equation:

$$\alpha_{ij} = \ln\left(1/w_{ij}\right) \tag{5-3}$$

where α_{ij} is considered the variance of additional Gaussian noise surrounding a datapoint. **Figure 5-4b** depicts normal distributions corresponding to Gaussian noises for various decay factors and interpoint distances. After establishing α_{ij} for each lower-fidelity point, these values are incorporated into the GPR framework, altering its prediction scheme to:

$$f(x) \sim \mathcal{GP}(m(x), k(x, x') + \alpha(d)I) \tag{5-4}$$

where $f(x)$ is a function to be predicted, $\mathcal{GP}$ is the Gaussian Process, $m(x)$ is the mean function, $k(x, x')$ is the kernel function describing covariance between points x and x', $\alpha(d)$ is an array of distance-dependent noise levels for each datapoint, and I is the identity matrix.

During fitting, α values are added to the kernel matrix's diagonal to introduce point-specific noise and a multiscale uncertainty structure in the model. **Figure 5-4c** illustrates SWGPR predictions for various decay factors, where dashed lines indicate its mean response, shaded areas represent 95% confidence bounds, and global covariance is modeled as the summed RBF and white noise kernels. For one extreme (h = 0.1), there is high uncertainty in lower-fidelity data, resulting in strong reliance and tight convergence around the experiment. Conversely, when h = 1.0, uncertainties are similar among fidelities and SWGPR predicts closely with the traditional GPR without $\alpha(d)$ terms.

Building on prior discussions, a three-fidelity TGML prediction scheme requires specifying h values for each virtual data source. To achieve this, uncertainties in simulation datapoints are assumed to primarily stem from material properties referenced during modeling. In simpler terms, inaccuracies in virtual data are hypothesized to be mostly attributed to numerical inputs rather than modeling capabilities, given the challenging nature of composites characterization and using publicly-sourced properties. Consequently, h is set equal to the inverse of the number of material properties used as inputs: h = 1/3 = 0.33 for low-fidelity and h = 1/15 =

0.07 for high-fidelity simulation. It is crucial to note that a smaller h value for high-fidelity simulation does not imply lower accuracy but acknowledges a larger margin for error due to a higher number of inputs.

After establishing h for each virtual data source, the TGML prediction method enters its final stage. At this point in the case study, a GPR model trained on 256 low-fidelity simulations is available for each PID type. The last step involves calibrating these models by conducting targeted high-fidelity simulations or experiments until a specified accuracy is achieved. The overarching goal is to attain desired accuracy with the minimum number of experiments and high-fidelity simulations to keep the model cost-effective.

To initiate calibration, one experiment is performed with parameters exhibiting the highest uncertainty in the GPR model. The experimental results replace the low-fidelity datapoint with the same input parameters, and other virtual points are weighed per (5-2) and (5-3). The SWGPR model is then retrained to predict PIDs and identify a new location with the highest uncertainty. Next, the parameters for which SWGPR are most uncertain are fed into the high-fidelity simulation scheme, PIDs are predicted, and the model is retrained. If the addition of high-fidelity simulation data improves accuracy, the process repeats with the high-fidelity simulation scheme. If accuracy remains unchanged or decreases, the process halts, and another experiment is conducted and added to the model. This process continues until the model meets accuracy requirements, where in this study, SWGPR must predict PIDs within the standard deviation of six testing laminates.

5.3 RESULTS AND DISCUSSIONS

In this section, the training of an SWGPR model for predicting the tip spring-in at the center of six L-shaped composite parts with layups and input parameters listed in **Table 5-1** is illustrated. Then, the SWGPR approach is extended to predict post-curing deformed L-shapes. The L-shape

prediction involved predicting all PID types (corner spring-in, tip spring-in, and warpage at the center and edge of each part), then generating interpolated profiles from these values.

Table 5-1. Layups and input parameters of testing laminates employed for evaluating the accuracy of SWGPR models.

Laminate	Layup	$B_{11} \times 10^{-3}$ (Pa·m^2)	D_{22} (Pa·m^3)
1	[90/90/90/90/0/0/0/0]	40.05	23.23
2	[0/90/0/90/90/0/90/0]	0.00	15.63
3	[90/0/0/90/0/90/90/0]	0.00	23.24
4	[0/0/0/0/0/0/0/0]	0.00	2.95
5	[90/0/90/0/90/90/0/90]	-2.50	31.16
6	[0/0/0/0/0/0/90/90]	-30.04	20.70

Figure 5-5 displays an SWGPR model and its predictions for tip spring-in of L-shaped laminates **(a)** before and **(b)** after undergoing calibration. Red points in the left-side plots represent low-fidelity simulations, blue squares are high-fidelity simulations, and black stars are experiments used for model training. Multi-colored surfaces depict the SWGPR models' mean predictions, while grey surfaces are 95% confidence bounds. Tip spring-in is plotted against B_{11} and D_{22}, identified as optimal parameters using the FBIC. The right side of the graphics display tip spring-in predictions for the six testing laminates, with black outlined bars and error bars representing average experimental values and standard deviations, respectively.

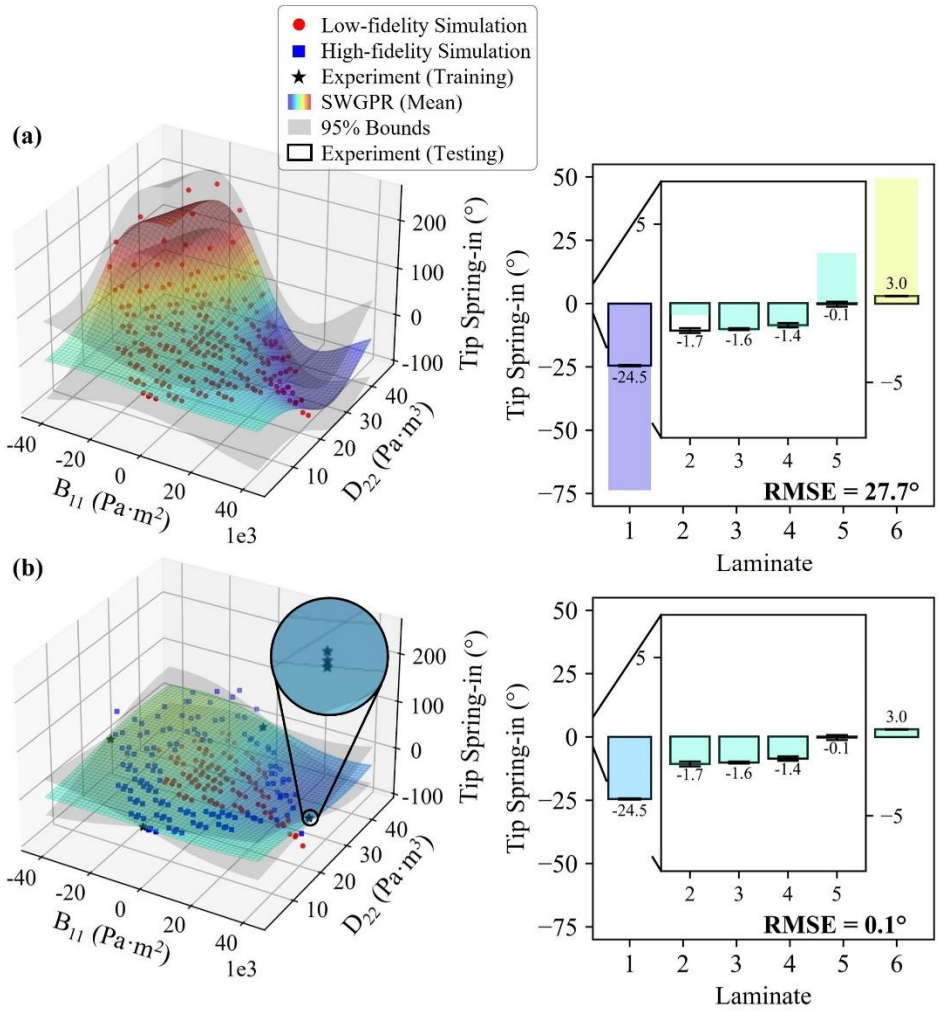

Figure 5-5. SWGPR model **(a)** before and **(b)** after calibration and its predictions of tip spring-in for L-shaped composite parts.

Initially, the SWGPR model trained on 256 low-fidelity simulations without spatial weighing exhibited a large RMSE of 27.7° in predicting tip spring-in for the six testing laminates. Upon adding the first experiment, the model's mean response and confidence bounds converged around the experiment and loosely followed low-fidelity data with additional Gaussian noises. Integrating high-fidelity simulation data then led to an evolving structure with increasing accuracy until approximately 40 simulations were added and the RMSE plateaued at 4.4°. Another experiment was then required near the model's bounds, suggesting inaccuracies in the high-fidelity simulation scheme and the need for multiple experiments in the domain. After calibration, the

SWGPR model incorporated 114 low-fidelity simulations, 138 high-fidelity simulations, 4 experiments, achieved a minimal RMSE of 0.1°, and predicted within the standard deviation for all six testing laminates. Most notably, the calibrated SWGPR structure was dominated by virtual simulation data and only required a minimal number of experiments for accuracy convergence. Overall, this illustrates that the SWGPR approach can effectively utilize virtual and real-world datatypes for accurate and cost-efficient analysis of composites manufacturing phenomena.

Figure 5-6 shows average experimental profiles for the cured L-shaped parts compared with SWGPR predictions after the calibration process. As previously mentioned, experimental profiles were generated through laser scanning the L-shaped coupons, two photos of which are also shown in the figure. All PID types necessitated four experiments, with minimal variation in the number of high-fidelity simulations to meet accuracy specifications. Overall, **Figure 5-6** demonstrates that similar to the convergence observed in tip spring-in predictions, the SWGPR method achieves highly accurate predictions of the L-shaped parts with minimal material characterization and experimental efforts, showing promise in better understanding PIDs and other facets of composites manufacturing.

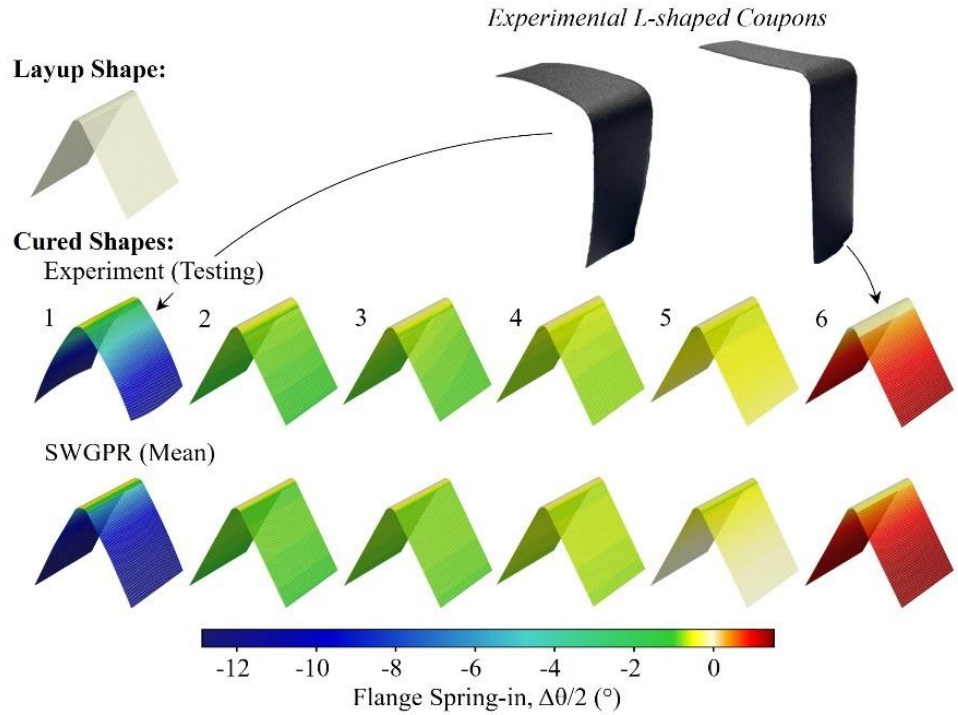

Figure 5-6. Comparison between experimental PIDs and predictions using calibrated SWGPR models.

5.4 SUMMARY

This chapter introduced an innovative approach for accurate and efficient analysis of composites manufacturing by combining multi-fidelity simulations, experimentation, and theory-guided machine learning (TGML). The method utilizes a novel strategy, Spatially Weighted Gaussian Process Regression (SWGPR), to build computationally fast surrogate models for predicting PIDs in L-shaped T800S/3900-2B parts. The SWGPR approach accurately predicts spring-in and final deformed shapes of cured L-shaped laminates after integrating just four experiments into the models' training domains and bypassing complex material characterization. The strategies presented hold promise for further investigation, understanding, and improvement of composites manufacturing.

6. ACCELERATED PROCESS OPTIMIZATION TO MINIMIZE DEFORMATIONS IN COMPOSITES USING THEORY-GUIDED PROBABILISTIC MACHINE LEARNING

6.1 BACKGROUND

This chapter presents a novel approach for process optimization of composites to minimize PIDs without the use of any material characterization or process simulation tools. The proposed method consists of limited element-level tests combined with TGML.[91,107,108,114–116] The method relies solely on experimental data to build and calibrate theory-guided GPR models and iteratively converge on optimal solutions with a few guided steps. The method introduced in this chapter offers an alternative, cost-efficient, and generalizable approach for mitigating process-induced defects in composite parts.

6.2 METHODS

6.2.1 Composites Manufacturing

Each experiment in this chapter followed identical procedures as described in Section 5.2.3 and schematically illustrated in **Figure 5-2**. First, three identical L-shaped parts were laid up evenly across an FEP-covered steel tool's width, vacuum sealed using standard bagging procedures, placed in an autoclave, and subjected to the MRCC. After curing and demolding, three laser scans were generated for each part and were superimposed on plots containing the tool's premeasured profile for that specific location. Then, using a custom Python[92] code, the two-dimensional area (δ) between the tool and part profiles was calculated using piecewise numerical (i.e., trapezoidal) integration. Next, using the three two-dimensional areas for each flange (i.e., one at each edge and one at the center) and their corresponding coordinates with respect to the part's width (Y), a single volumetric deformation value (Δ) was calculated using another iteration of trapezoidal integration. This volumetric value, illustrated in **Figure 6-1**, was used to quantify the

overall deformation for each composite part manufactured in this study. Positive and negative deformation values correspond to volumetric expansions or contractions between flanges relative to the layup shape. In cases where the direction (i.e., sign) of deformation varies across the length of a part's flange, the positive and negative contributions are added and thus deformation may tend to approach zero.

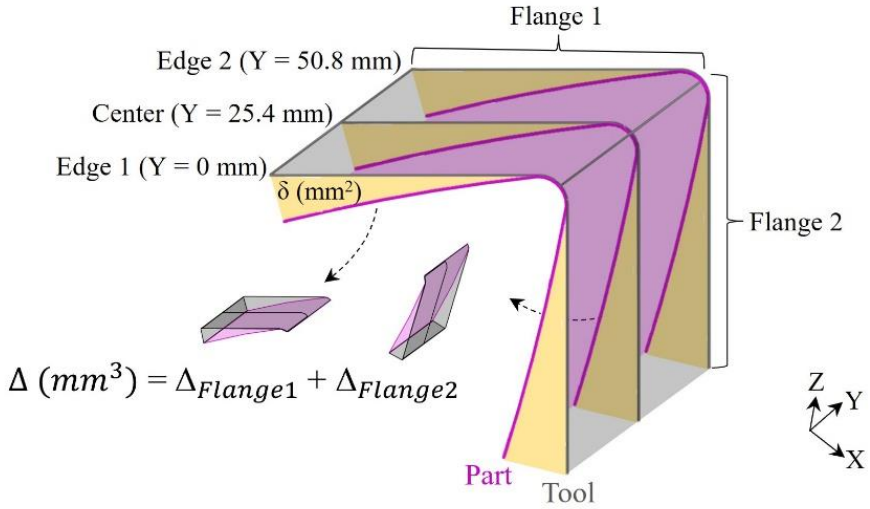

Figure 6-1. Graphic representation of approach used to quantify deformation of L-shaped composite parts.

6.2.2 TGML Optimization Methodology

In this section, the general form of an optimization methodology is presented, designed to find optimal process parameters to minimize PIDs in L-shaped composite parts while meeting manufacturing cost specifications. The method employs an iterative Bayesian solution scheme based on limited experimental testing and TGML, as depicted in **Figure 6-2**. The TGML strategy is comprised of two main phases: Initialization and Optimization. During Initialization, closed-form theories (i.e., governing physical laws) are used to parametrize the potential solutions (e.g., layup, cure cycle) considered for each optimization problem. Next, a custom cost function is defined to quantify the manufacturing cost of each potential solution. In manufacturing settings, the cost of a composite part will be partially related to its total deformation, since larger PIDs

would necessitate increased time, material, and labor to compensate for the higher degree of component mismatches.[101] Additionally, the overall cost of a part would be directly linked to the manufacturing time (i.e., cycle time) required to produce it. Therefore, in this study, custom cost functions will be defined as a function of deformation and manufacturing time.

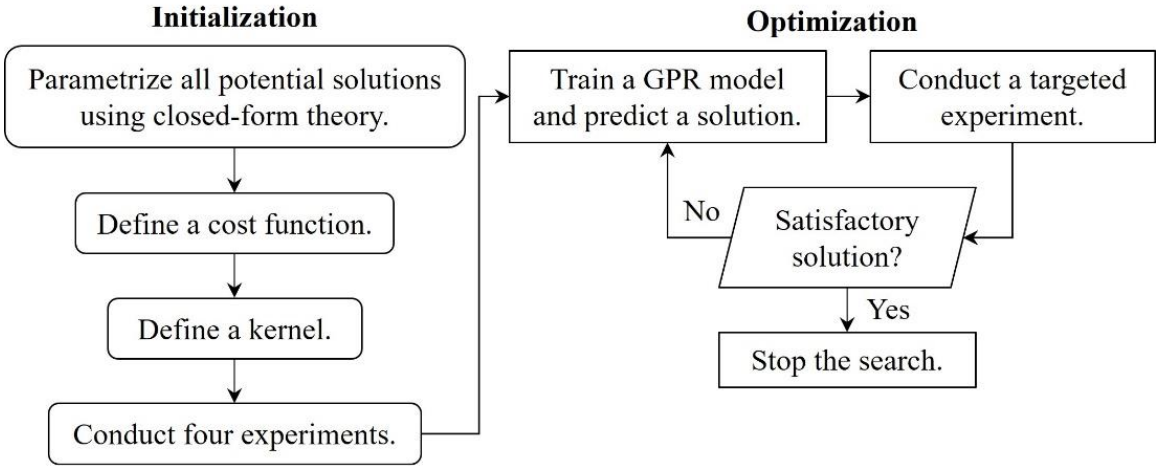

Figure 6-2. TGML process optimization methodology to minimize PIDs in composite parts.

After the cost function is defined, a kernel is selected to be used for GPR model training. As previously highlighted, a kernel should be chosen which captures the complexity of the defined cost function without possessing a high chance of overfitting.[117] Finally, the last step of Initialization is to conduct four experiments at strategic points in the design space, each with a diverse set of training parameters. Given that each experiment yields data for three samples, this results in the creation of a robust and statistically significant dataset for initial GPR training.

After completing the four Initialization steps, a GPR model is trained to predict the cost of all the potential solutions using the results of the four initial experiments. During training, the GPR model learns underlying trends and correlations in the data, then generates mean predictions and probability distributions for the costs of all other potential solutions. Then, a targeted experiment is conducted with parameters for which the GPR model's mean prediction is optimal. After one targeted experiment, the GPR model is retrained with the updated experimental results and

produces a new mean prediction for an optimal solution. Finally, experiments are conducted and the GPR model is retrained until an optimal solution is predicted and validated experimentally. The results and discussions in the following sections will demonstrate each step of the TGML method for two manufacturing scenarios: layup and cure cycle optimization to minimize PIDs.

6.3 RESULTS AND DISCUSSIONS

6.3.1 Layup Optimization

As discussed previously, the first step of the TGML method is to parametrize all potential solutions to be considered in the optimization search. In this case study, eight-ply layups consisting of zero- and ninety-degree plies were considered as potential solutions. However, UD laminates (i.e., $[0]_8$ and $[90]_8$) were omitted from the analysis, and thus, a total of $2^8 - 2 = 254$ possible layups were evaluated. It should be noted that the layups chosen as potential solutions were selected based on work from previous chapters and that the design space may be easily extended or altered in future problems.

Once the potential solutions were defined, each layup was parametrized using two theory-based features. This approach also serves to provide physics-based "guidance" to the domain and enhance the model's accuracy, forming the basis of the "theory-guided" machine learning approach. The first feature was set equal to the linear determinant of each laminate's ABD stiffness matrix (Chapter 4).[111] Mechanical properties needed for stiffness calculations were obtained from publicly available literature.[26,36,106] The determinants of each matrix were calculated using LU factorization in Python and will be referred to as "ABD" values through the remainder of this chapter.[92,118] Laminates with negative in-plane/out-of-plane coupling coefficients (B_{11}) were assigned negative ABD values to parametrically distinguish between opposite layups with identical stiffness magnitudes. The second feature was set equal to the ratio of through-thickness

shear stiffness (G_{yz}) to bending stiffness (E_{xb}), following closed-form theory available for process-induced stresses and deformation of curved composite parts.[19,28,101] After the theory-based features were established, each layup was projected into a TGML design architecture with two unique theory-based features, shown as points in **Figure 6-3**.

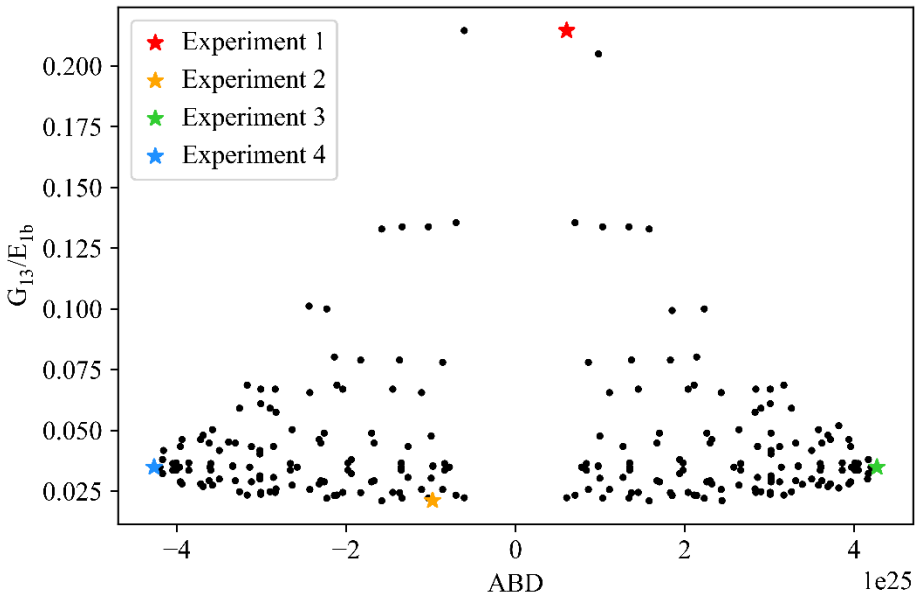

Figure 6-3. Theory-based design space consisting of all potential solutions (black points) and the first four experiments (colored stars) used for layup optimization.

After all the layup candidates were parametrized, a function was defined to quantify the cost of each potential solution. As previously mentioned, the total cost of each composite part in this work is considered to be a function of deformation and manufacturing time. Since only eight ply layups were considered in this work and thus manufacturing time is consistent among the potential solutions, the cost of each laminate was set equal to:

$$Cost = |\Delta| \tag{6-1}$$

where $|\Delta|$ is the absolute value of the L-shape's final deformation. This defined cost function is illustrated in **Figure 6-4**, where the manufacturing time variable is included only for visualization purposes.

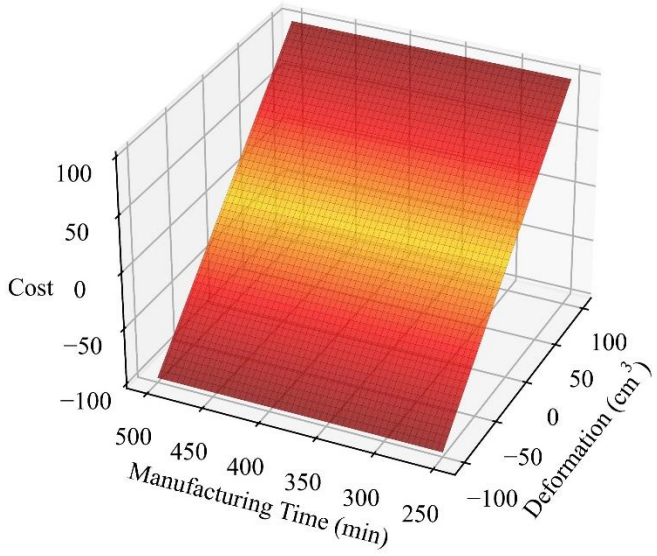

Figure 6-4. Cost function defined for layup optimization.

After the cost function was defined, a kernel was selected to be used for GPR training and optimization. For this study, a summation of the Radial Basis Function (RBF) and white noise kernels was used to describe the covariance between datapoints:[117]

$$k(x, x') = k_{rbf}(x, x') + k_w(x, x') \tag{6-2}$$

In the specified kernel, the RBF component (k_{rbf}) detects non-linear relationships using Gaussian similarity, promotes smoothness in the model's response, and allows for generalizability, while the k_w accounts for independent noise in the data. In mathematical terms, the kernel can be defined as:

$$k(x, x') = e^{\frac{||x-x\prime||^2}{2l^2}} + \sigma_n^2 \tag{6-3}$$

where l is the length scale of the RBF kernel and σ_n^2 is a positive constant representing the noise level in the dataset. In this study, σ_n^2 was set to the default value of unity, while l was bounded between 1×10^{-5} and 1×10^{5} then optimized each iteration using scikit-learn's hyperparameter tuning capabilities.[93] Then, according to the final Initialization step, four experiments were conducted at

the upper and lower bounds of the TGML design architecture. The layups and features chosen for the initial tests are listed in **Table 6-1** and illustrated in **Figure 6-3** as colored star points.

Table 6-1. Layups and theory-based features used for GPR training of the first four layup optimization experiments.

Experiment	Layup	GPR Inputs	
		ABD $(\times \mathbf{10^{24}})$	$\mathbf{G_{13}/E_{1b}}$
1	[90/90/90/90/0/90/90/90]	6.05	0.215
2	[0/0/0/90/90/0/0/0]	-9.81	0.021
3	[90/0/0/90/0/90/90/0]	42.7	0.035
4	[0/90/90/0/90/0/0/90]	-42.7	0.035

Figure 6-5 shows the spatial profiles and flange spring-in of one L-shaped composite part from each of the first four layup optimization experiments. As previously mentioned, the stacking sequence of each laminate is listed in **Table 6-1**. The tool's profile (i.e., layup shape) is also shown in the figure for comparison purposes. Note that positive spring-in values represent angle enlargements, while negative values represent angle enclosures. Correspondingly, positive and negative deformation values are indicative of volumetric expansions or contractions between flanges relative to the layup shape. Although all layups produced negative deformation, **Figure 6-5** demonstrates that the layup used in Experiment 1, with the highest G_{yz}/E_{xb} term, produced significantly larger absolute deformation than the other three training tests. These results reinforce the closed-form theory used during parametrization, which describes PIDs for curved composites parts as directly correlated to the ratio of through-thickness shear modulus to bending stiffness.[19,28,101]

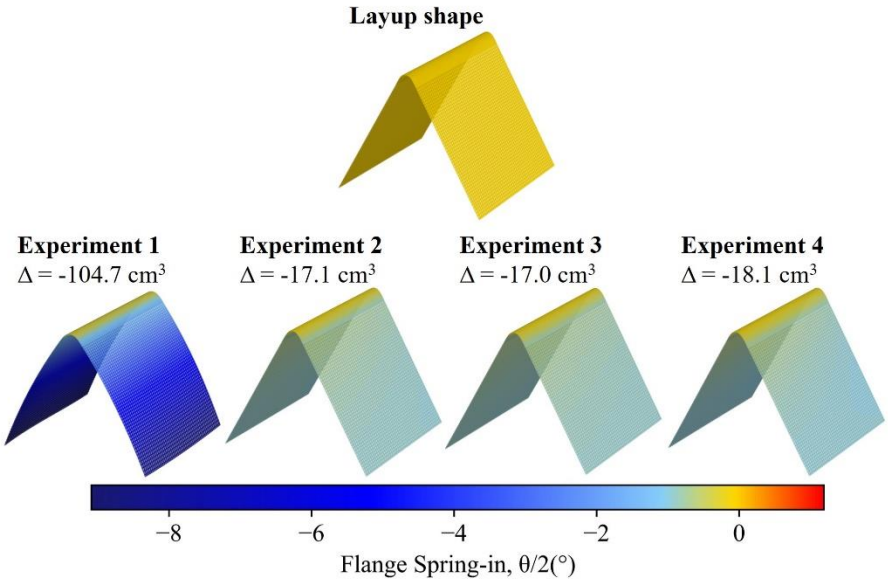

Figure 6-5. Spatial profiles and flange-spring-in of L-shaped composite parts with layups specified by the first four GPR training experiments.

Figure 6-6 shows a surface of the GPR model's mean response after training/initialization from four experiments. The prior experimental data, from which the GPR model is trained, is shown as black points. These consist of the GPR inputs listed in **Table 6-1** and three measured deformation values for each layup. The mean predicted values for all other layups in the TGML design space are depicted by the colored surface and demonstrate a strong dependence on the laminates' ABD stiffness properties. Additionally, the surface predicts a sharp increase in cost and absolute deformation for laminates with large G_{yz}/E_{xb} ratios, primarily due to the significant experimental deformation observed in Experiment 1. Therefore, after training based on four tests, the GPR model predicted the smallest deformation for a [0/0/0/90/0/90/0/90] layup with a low G_{yz}/E_{xb} term. Following the TGML optimization methodology, this stacking sequence was used as the next experiment's layup.

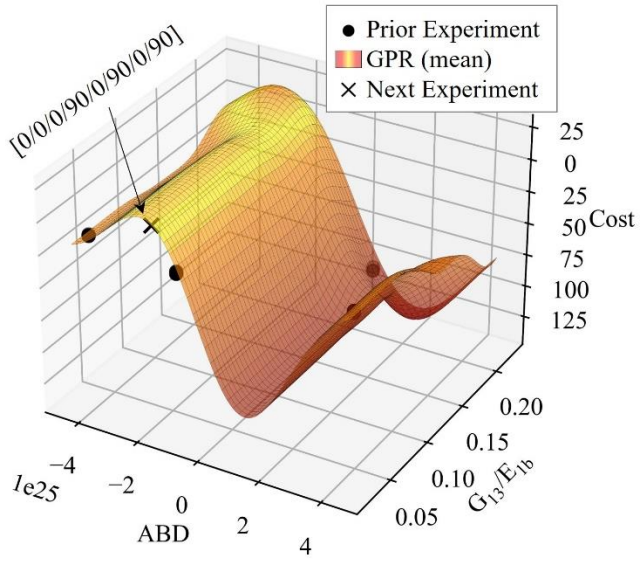

Figure 6-6. GPR model trained on four experiments and its prediction of the optimal layup (next experiment) to minimize PIDs.

Figure 6-7 shows the profile and spring-in of one L-shaped composite part cured according to the layup specified by the first GPR targeted experiment. Compared with the first four experiments, the first targeted layup produced a significant reduction in absolute deformation but resulted in net positive deformation. This form of deformation occurred due to the high magnitude of concave up flange warpage causing a volumetric enlargement between flanges. Although deformation remained evident in the first targeted laminate, the results in **Figure 6-7** demonstrate that the GPR algorithm successfully provided a layup with reduced absolute PIDs after just four training tests. Next, following the TGML methodology, the results from Experiment 5 were added to the training dataset and a new solution was predicted.

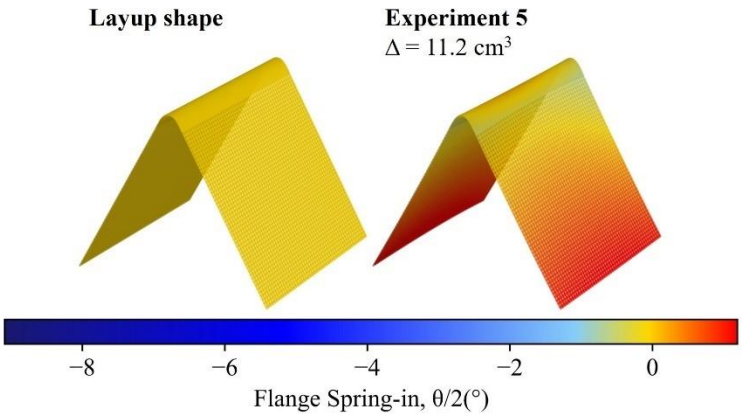

Figure 6-7. Spatial profile and flange spring-in of an L-shaped composite part cured according to the first GPR targeted layup.

Figure 6-8 shows a surface of the GPR model's mean response after four initial and one targeted experiment. Again, prior experimental data on which the GPR is trained is shown in black points, whereas the mean predicted values for all other layups throughout the design space are illustrated by the colored surface. After five total experiments, the GPR model presented a similar interrelationship between ABD, G_{yz}/E_{xb}, and deformation as the first iteration. However, since the first targeted laminate resulted in a net positive deformation, the GPR model predicted a minimal deformation for a different layup with more zero-degree plies beneath the midplane: [0/0/0/0/90/0/90/0]. Once more, following the TGML optimization methodology, this stacking sequence was used as the next experiment's layup.

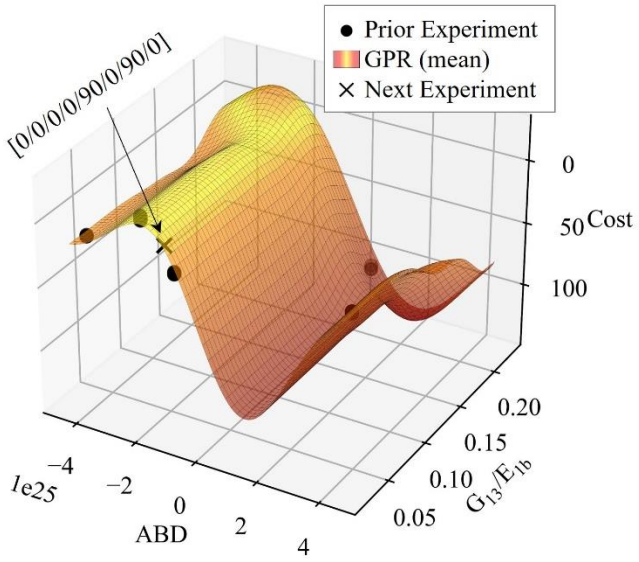

Figure 6-8. GPR model trained on four initial and one targeted experiment and its prediction of the optimal layup (next experiment) to minimize PIDs.

Figure 6-9 shows the profile and spring-in of one L-shaped composite part cured according to the layup specified by the second GPR targeted experiment. The profile illustrates a close agreement with the layup shape and produced an average overall deformation of -2.6 cm^3. To put this value into perspective, this magnitude of deformation corresponds to an average out-of-plane distortion of approximately 150 μm along the length of each flange. In the context of this study, such a minimal deformation value meant the GPR model converged to an optimal solution with near-zero deformation after four initial and two targeted tests guided by theory. The TGML method's stepwise convergence to an optimal layup which minimizes PIDs in L-shaped composite parts is reiterated in **Figure 6-10**.

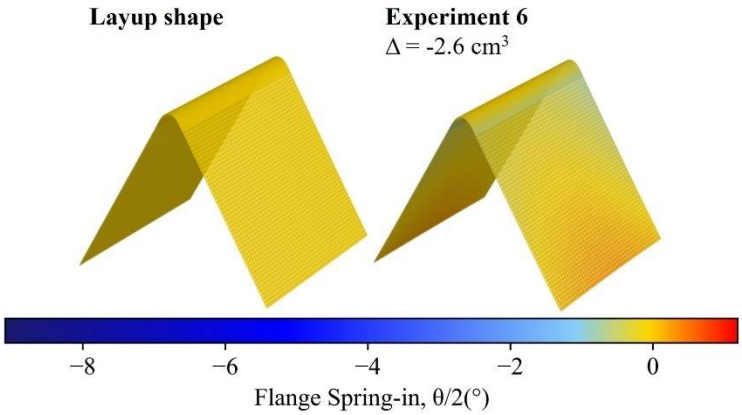

Figure 6-9. Spatial profile and flange spring-in of an L-shaped composite part cured with the second GPR targeted layup.

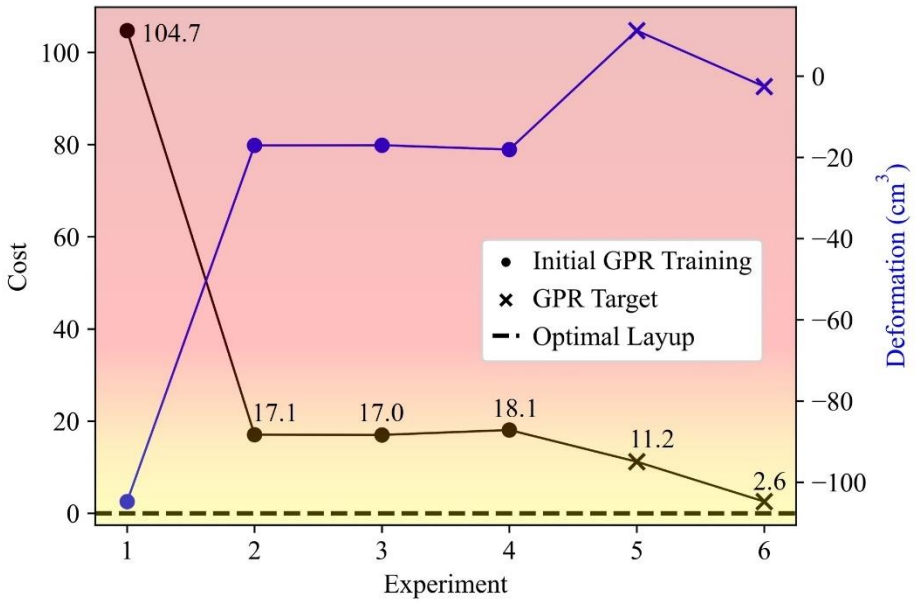

Figure 6-10. TGML optimization method's convergence to an optimal layup which minimizes cost and deformation of L-shaped composite parts.

6.3.2 Cure Cycle Optimization

In this subsection, the TGML method previously utilized for layup optimization is employed to find a cure cycle that produces lower PIDs and costs less than the MRCC. As previously discussed, the first step of the TGML method initializes by constructing a design architecture consisting of parametrized potential solutions. In this case study, potential solutions include two-stage (i.e., "two-hold", "two-step", etc.) cure cycles, wherein all cycles include a

variable first stage and a fixed second stage consisting of a temperature hold and cool-down equal to 180 °C for 120 minutes and 2.78 °C/min, respectively (**Figure 6-11**). The second-stage temperature and cool-down values were chosen based on the MRCC for the T800S/3900-2B material system to ensure a final degree of cure of approximately 90%.[36] It should be noted that the cure cycle configuration chosen for a potential solution space was selected based on its simplistic nature and that the design space may be extended or tailored in future problems.

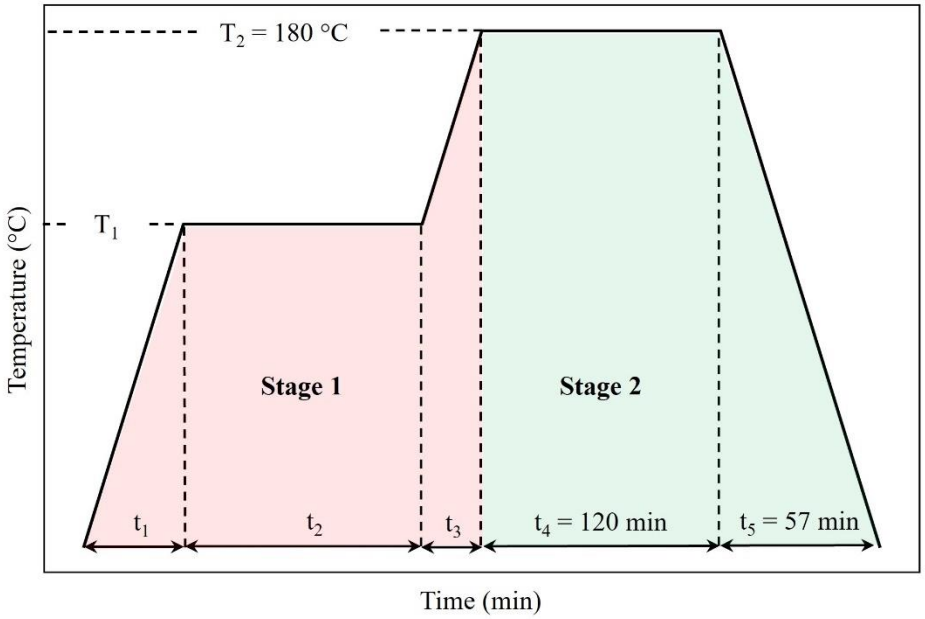

Figure 6-11. Generalized temperature profile of a two-stage cure cycle with a variable first stage and a fixed second stage.

The first stage of a cure cycle may be described by four main parameters: first heat-up time (t_1), hold temperature (T_1), hold time (t_2), and second heat-up time (t_3). By setting constraints or potential values for these parameters, a wide range of evaluable solutions can be generated. In this work, six values for T_1 (120, 130, 140, 150, 160, 170 °C) and t_2 (900, 600, 420, 300, 240, 180 min) were used as parameters for potential hold temperatures and times. The choice of potential hold times was based on the time for complete vitrification to occur ($T_g > T + 28$℃) at each value of T_1.[62,63] Additionally, values for t_1 and t_3 were determined by constraining ramp rates to 2, 4, and

8 °C/min for the first heat-up and 0.1, 2, 4, and 8 °C/min for the second heat-up. Consequently, by defining three potential first ramp rates, six hold temperatures, six hold times, and four second ramp rates, a total of 3 × 6 × 6 × 4 = 432 possible cure cycles were defined to be considered as potential optimization solutions in this case study.

After the list of potential solutions was constructed, closed-form theory was used to generate two additional parameters to describe each of the 432 cycles. First, the evolution of T800S/3900-2B's glass transition and the temperature at which vitrification occurs (T_{vit}) during each cycle were calculated using Dykeman's model.[63] The vitrification temperature has been demonstrated to be highly influential in the development of process-induced residual stresses and deformations in similar thermosetting composite materials.[119,120] Given the presence of thermoplastic tougheners in T800S/3900-2B, the state of these particles during processing could also play a critical role in residual stress formation and PID levels. To account for the effects of thermoplastic tougheners in the cure cycle parameters, the glass transition temperature of the particles ($T_{g,tp}$), which was assumed to be 150 °C, was subtracted from each T_{vit} value for every cycle.[71] Thus, the fifth parameter to describe each cycle was set equal to $T_{vit} - T_{g,tp}$.

The sixth and final parameter was included to recognize the significance of devitrification ($T > T_g$) in the development of residual stresses. Following the cure kinetics model used for T_{vit} calculations[63], cycles exhibiting no devitrification were assigned a value of 0, while cycles experiencing devitrification were labeled with a parameter of 1. Thus, at the completion of the parametrization phase, a list of 432 potential solutions was constructed, each with a unique combination of six parameters: t_1, T_1, t_2, t_3, $T_{vit} - T_{g,tp}$, and 0 or 1 corresponding to devitrification.

In the next step of the Initialization phase, a cost function for each cure cycle in terms of deformation and manufacturing time (i.e., cycle time) is defined. Unlike in layup optimization, the

different potential solutions (i.e., cure cycles) will have a range of manufacturing times and thus the total cost of each cure cycle was set to include this variable:

$$Cost = \frac{K}{C + ve^{-B\Delta}} + L\Delta - B + 0.1t \tag{6-4}$$

where Δ is the deformation of the L-shaped parts, t is the total cycle time, K (1000) are the lower and upper bounds of a sigmoid function, B (0.1866) is the sigmoid function's growth rate, v (0.2229) and C (1) are constants which affect the steepness of the sigmoid function's transitions, and L (1) is the slope of a linear function. All constants included in the function were standard values commonly used in the sigmoid function. In nonmathematical terms, the equation above states that the total cost of each cycle is exponential-linearly dependent on the deformation of L-shaped parts, and linearly dependent on total manufacturing time. A sigmoid function was used to estimate cost due to its widespread use in probability estimation and ML problems, and to assess the effectiveness of the TGML procedure when attempting to optimize more complex functions. A plot of the defined cost as a function of deformation and manufacturing time is shown in **Figure 6-12**. The cost for the one-hold MRCC cycle, calculated from previous experiments, is also illustrated in the plot. As previously mentioned, the goal of this case study is to find a two-hold cure cycle in the design space which produces lower PIDs and costs less than the MRCC.

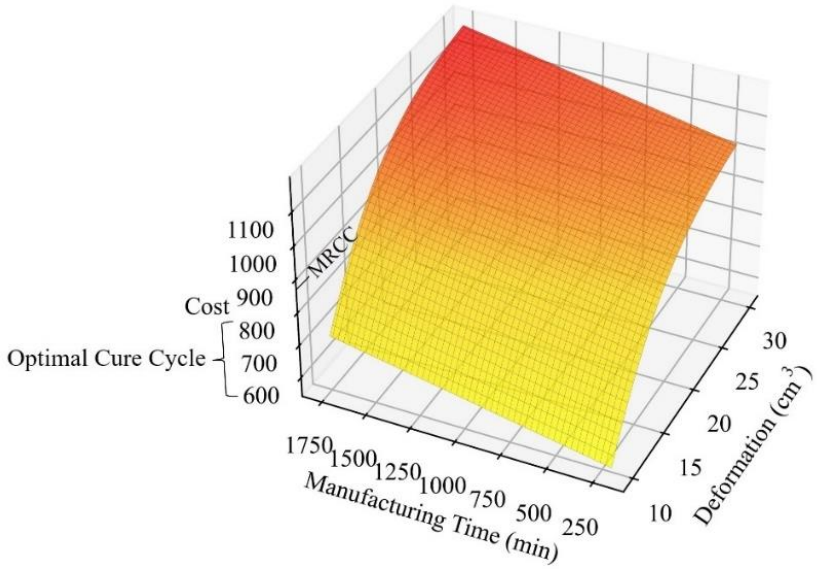

Figure 6-12. Cost function defined for cure cycle optimization.

After the cost function was defined, a kernel was selected for GPR training and optimization. For this case study, a combination of linear and Matérn kernels was used to describe the covariance between datapoints:[117]

$$k(x, x') = k_l(x, x') + k_m(x, x') \tag{6-5}$$

$$k(x, x') = (x \cdot x') + \frac{1}{\Gamma(\nu)2^{\nu-1}}\left(\frac{\sqrt{2\nu}}{l}\left||x - x'|\right|\right)^{\nu} K_\nu\left(\frac{\sqrt{2\nu}}{l}\left||x - x'|\right|\right) \tag{6-6}$$

where Γ is the gamma function, ν is a parameter which controls the smoothness of the resulting function, l is the length scale, and K_ν is a modified Bessel function,.[85] In this study, values of $\nu = 2.5$ and $l = 1$ were initially chosen for GPR training, then were optimized during each calibration phase using twenty restarts in scikit-learn's hyperparameter optimizer.[93] This allowed for the complex exponential-linear behavior of the cost function to be captured while still maintaining generalizability.

The final step of the Initialization phase was to conduct four experiments. The temperature profiles (T), simulated glass transition temperatures of the thermoset ($T_{g,ts}$) and thermoplastic

($T_{g,tp}$), and degree of cure (DoC) for each of the four selected cycles are shown in **Figure 6-13**.[63] The simulated vitrification temperatures for Experiments 1, 2, 3, and 4 were 120, 150, 120, and 180 °C, respectively. Devitrification occurred in Experiments 2 and 3 but did not occur in Experiments 1 and 4. The four cycles used during GPR initialization were chosen because they offer a wide range of diverse training parameters, as listed in **Table 6-2**.

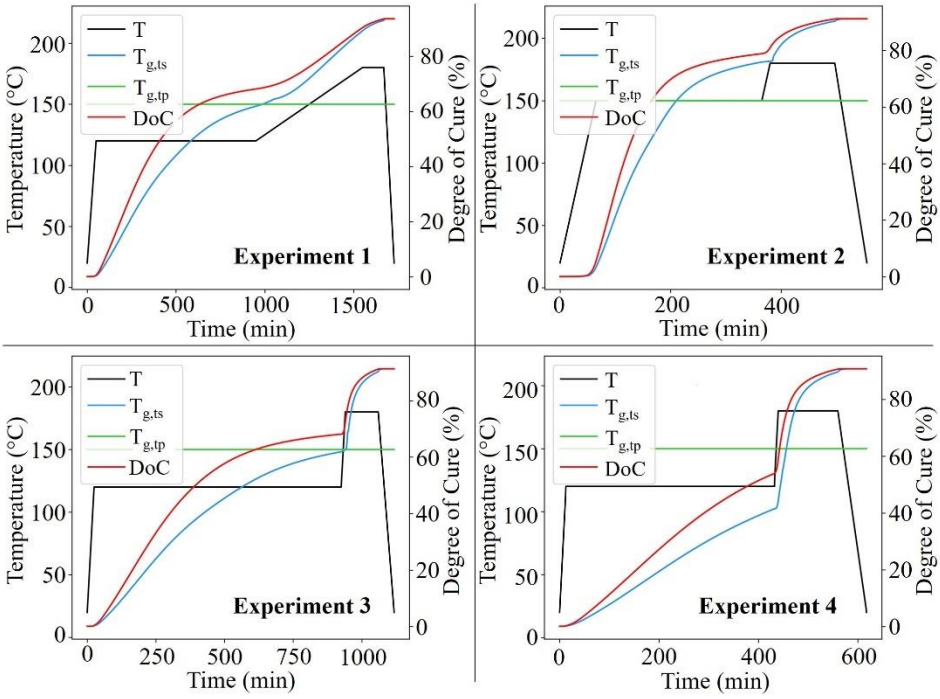

Figure 6-13. Processing temperatures, glass transition temperatures, and degree of cure for the first four cure cycle optimization experiments.

Table 6-2. GPR training parameters for the first four cure cycle optimization experiments.

Experiment	GPR Inputs					
	t_1 (min)	**T_1 (°C)**	**t_2 (min)**	**t_3 (min)**	**$T_{vit} - T_{g,tp}$ (°C)**	**Devitrification? (0 = No, 1 = Yes)**
1	50	120	900	600	-30	0
2	35	150	300	15	0	1
3	25	120	900	15	-30	1
4	12.5	120	420	7.5	30	0

Figure 6-14 shows the spatial profiles and flange spring-in of one L-shaped composite part cured during the four initial experiments. The profile and spring-in of the tool and a composite part cured according to the one-hold MRCC are also included in the figure for comparison. The average deformation (Δ), manufacturing time (t), and total cost of each cycle are also listed in the figure. The results in **Figure 6-14** entice two discussion-worthy points. First, Experiment 4, which caused vitrification to occur at the highest temperature of 180 °C, showed to significantly elevate PID levels in the L-shaped composite parts. These findings reinforce results obtained in previous studies on similar materials, showing a direct link between vitrification temperature and deformation.[119] Secondly, the profile and deformation measurements from Experiment 1 showed that PIDs may be significantly reduced by adding lower-temperature intermediate holds into a cure cycle. For example, during Experiment 1, the material vitrified at 120 °C and exhibited a reduction in deformation of approximately 10% for the cross-ply laminate.

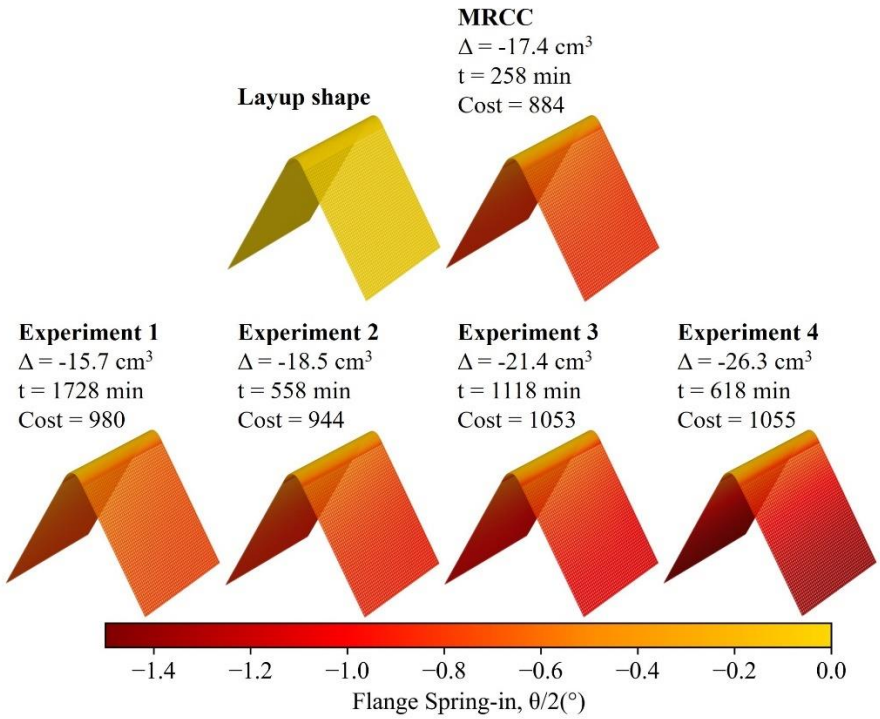

Figure 6-14. Spatial profiles, deformation (Δ), manufacturing time (t), and cost of L-shaped composite parts cured according to the first four GPR training experiments compared with the layup shape and one-hold MRCC cycle.

Although Experiment 1 demonstrated a significant reduction in deformation, the total cost of the cycle was higher than the MRCC's due to the relatively long cycle time. These results indicated that the optimal solution had not been completed in the four training tests, and that initializing a GPR search was the necessary next step to conduct following the TGML method. Thus, using the six inputs listed in **Table 6-2** and the three experimental costs of each of the four training cycles, the trained GPR model predicted the smallest cost and deformation for the following sequence of parameters: t_1 = 32.5 min, T_1 = 150 °C, t_2 = 300 min, t_3 = 300 min, $T_{vit} - T_{g,tp}$ = 0 °C, and Devitrification = 0. This sequence equates to a cure cycle of heating from 20 to 150 °C at 4 °C/min, holding at 150 °C for 300 minutes, heating to 180 °C at 0.1 °C/min, holding at 180 °C for 120 minutes, then cooling to room temperature. The specified cycle was thus chosen for the first targeted experiment and is labeled as Experiment 5 through the remainder of this section. Note that unlike during layup optimization, the GPR predictions for each of the potential solutions cannot be visualized using a three-dimensional surface due to the high number of input variables.

Figure 6-15a shows the spatial profile and flange spring-in of one L-shaped composite part cured according to the first GPR targeted test. The overall deformation, manufacturing time, and total cost of Experiment 5 are also compared to the MRCC results in the figure. Compared to the MRCC test, the first targeted cycle showed a lower absolute deformation value. These results demonstrate that the GPR algorithm successfully provided parameters for a cure cycle with reduced PIDs after just four training tests. However, the total cost of the first targeted cycle remained slightly higher than the MRCC's due to the relatively long cycle time.

Since the cost constraints had not been satisfied after one targeted cycle, the GPR model was retrained with updated experimental results, consisting of four training tests and one targeted

test. After retraining, the GPR model predicted the smallest cost and deformation for the following sequence of parameters: t_1 = 75 min, T_1 = 170 °C, t_2 = 180 min, t_3 = 2 min, $T_{vit} - T_{g,tp}$ = 20 °C, and Devitrification = 0. This sequence equates to a cure cycle of heating from 20 to 170 °C at 2 °C/min, holding at 170 °C for 180 minutes, heating to 180 °C at 2 °C/min, holding at 180 °C for 120 minutes, then cooling to room temperature. The specified cycle was thus chosen for the second targeted experiment and is labeled and referenced as Experiment 6 through the remainder of this section.

Figure 6-15b shows the spatial profile and flange spring-in of one L-shaped composite part cured according to the second GPR targeted experiment. The relative deformation, manufacturing time, and total cost of Experiment 6 are also compared to the MRCC results in the figure. Compared with the MRCC test, the second targeted cycle showed an approximate 5% reduction in volumetric deformation and lower manufacturing cost. In other words, the GPR algorithm converged to an optimal solution after four initial and two targeted experiments guided by theory. **Figure 6-16** summarizes the experimental results obtained for each cure cycle throughout this case study and outlines the TGML method's convergence to an optimal solution.

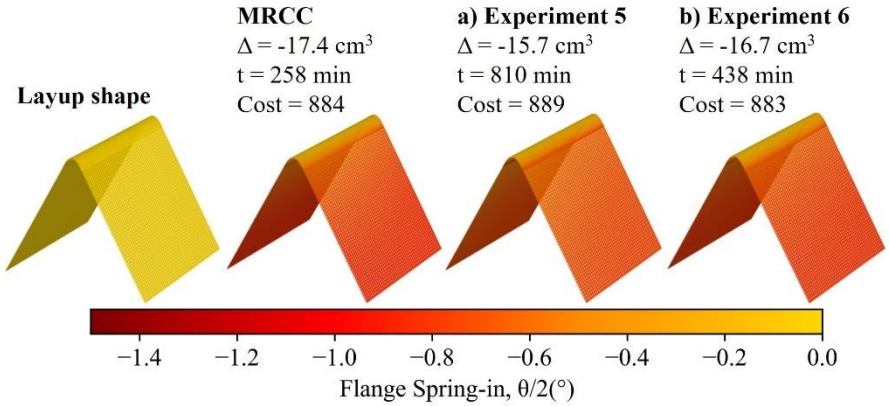

Figure 6-15. Spatial profiles, deformation (Δ), manufacturing time (t), and cost of an L-shaped composite part cured according to the a) first and b) second GPR targeted experiment compared with the layup shape and one-hold MRCC cycle.

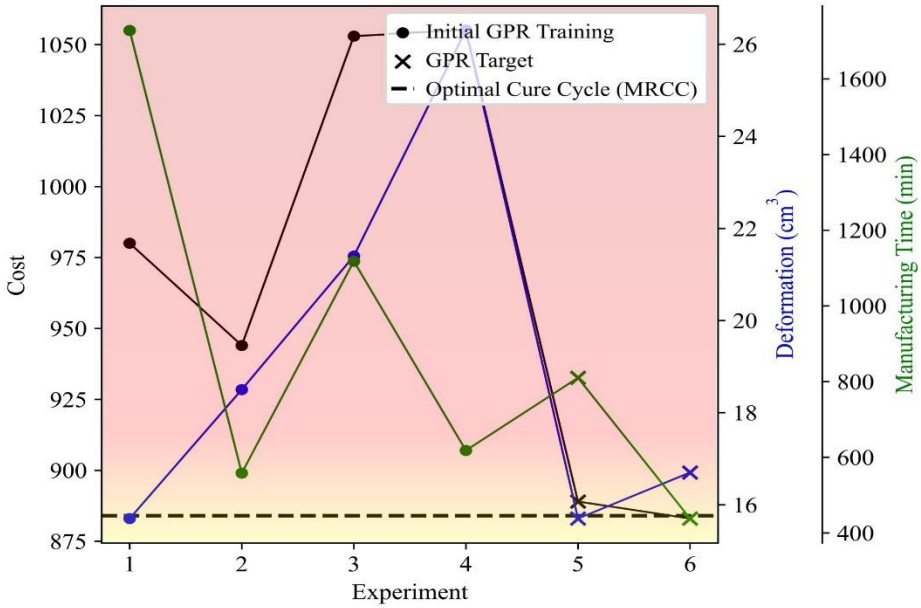

Figure 6-16. TGML optimization method's convergence to an optimal cure cycle which minimizes deformation in L-shaped composite parts while meeting cost constraints.

6.4 SUMMARY

This chapter demonstrated a novel process optimization approach and its application to minimize PIDs in composite parts without using any material characterization of process simulation. The proposed strategy consists solely of a limited number of element-level experiments and Gaussian Process Regression (GPR) guided by closed-form theory. The TGML procedure is generalizable and may be used to efficiently minimize PIDs (e.g., spring-in, warpage, volumetric deformation, etc.) for any quantifiable part geometries and optimize any other residual stress-contributing process parameters (e.g., out-time, tool surface condition, etc.). In this chapter, the TGML optimization strategy was utilized for two case studies: layup and cure cycle optimization to minimize PIDs in L-shaped T800S/3900-2B parts. For both cases, optimal parameters were identified and validated through a mere six experiments and without any material characterization or simulation efforts.

7. SUMMARY, CONCLUSIONS, AND FUTURE WORK

7.1 SUMMARY AND CONCLUSIONS

The primary aim of this research was to investigate the impacts of processing uncertainty and variability on residual stresses and deformations in advanced aerospace composites, with a specific focus on Toray T800S/3900-2B, a current-generation aerospace material used in production of aircraft such as the Boeing 787. The research began with a comprehensive characterization of various material properties and manufacturing phenomena that may significantly impact process-induced deformations (PIDs) yet are surrounded by high levels of uncertainty. Emphasis was placed on three key areas: 1) understanding the physicochemical behavior of release coating, 2) characterizing the evolution of thermo-mechanical properties (i.e., modulus and free strains) of T800S/3900-2B during cure, and 3) investigating underlying mechanisms of tool-part interactions. Key findings from these analyses are as follows:

- The type, quantity, and age of release coating directly impact tool surface roughness and free energy throughout production. During the initial processing cycles of a freshly release-coated tool, a conditioning process takes place, where the coating's characteristics become "locked-in" and can maintain stability for over twenty autoclave processing cycles for flat parts. Optimal conditioning for minimizing tool surface free energy is likely achieved within one to three processing cycles.
- Variations in processing conditions significantly impact the thermo-mechanical properties of T800S/3900-2B. Increased autoclave pressures result in greater deformation of thermoplastic particles, while different curing temperatures create diverse evolutions in storage modulus and free strains. Mathematical models describing these thermo-mechanical behaviors can be referenced in Chapter 2.

- Processing variabilities play significant roles in tool-part interactions for T800S/3900-2B. Excessive application of release coating can elevate these interactions, while using lesser amounts can reduce associated stresses. Cure pressure also has pronounced effects, with the highest tool-part stresses observed at intermediate autoclave pressures. Laminate layup and cure temperature impact tool-part interaction behaviors due to mechanical and viscoelastic mechanisms. A novel theory and mathematical model describing the tool-part interaction behavior for T800S/3900-2B can be referenced in Chapter 2.

Following the characterization effort, a novel method was developed for accelerating composite characterization, utilizing Gaussian Process Regression (GPR) to efficiently construct predictive models of thermo-mechanical properties. This approach demonstrated significant time and cost savings compared to traditional methods and holds promise for addressing other characterization challenges.

The next research phase involved a parametric exploration of layup and cure cycle impacts on PIDs of L-shaped composite parts. Thermo-mechanical property models were incorporated into finite element (FE) simulations to examine various design variables. A key discovery was that the spring-in of L-shaped parts may potentially be minimized by employing asymmetric layups featuring transverse fibers above the part's midplane and negative in-plane/out-of-plane coupling coefficients (B_{11}).

Subsequently, an innovative method was developed for accurate and efficient analysis of PIDs and composites manufacturing, employing multi-fidelity simulations, experimentation, and theory-guided machine learning (TGML). This method utilized a novel strategy, Spatially Weighted Gaussian Process Regression (SWGPR), to construct rapid and accurate surrogate

models for predicting PIDs in L-shaped T800S/3900-2B parts. These strategies offer tremendous potential for continued exploration and understanding of composites manufacturing.

Finally, a novel process optimization approach was developed capable of minimizing PIDs in composite parts without using any material characterization or process simulation. This adaptable strategy was devised by employing theory-guided machine learning (TGML) and was demonstrated to efficiently find layup and cure cycle solutions to meet manufacturing cost constraints. The strategy presented holds potential to effectively minimize various types of PIDs such as spring-in, warpage, and volumetric deformation. Furthermore, the TGML method may offer tremendous cost-saving benefits in manufacturing scenarios and other industries where quick problem-solving is crucial.

7.2 FUTURE WORK

During the course of this research, several paths for future investigations have emerged:

- Many analyses underscored the significant influence of thermo-mechanical properties on process-induced deformations (PIDs) in T800S/3900-2B. Across all analyses, it was evident that reducing the prepreg's through-thickness shear modulus and free strains during processing may prove advantageous in mitigating PIDs. These properties are likely modifiable through optimizing the formulation of the material, including the thickness of interply-toughening layers.
- There exists a clear need for the enhancement of tool-part interaction modeling and the integration into an efficient process simulation framework. Developing a method to numerically represent complex behaviors at the tool-part interface during processing holds the potential to significantly enhance the fidelity and efficacy of process simulation tools.

- The utilization of probabilistic methods has demonstrated tremendous potential in efficiently addressing diverse challenges in this research. With the ongoing advancement of machine learning (ML) and artificial intelligence (AI), there is a need to continue expanding the methodologies developed in this study. This will allow scientists and engineers to gain deeper insights into PIDs in composites and efficiently solve other problems.

BIBLIOGRAPHY

[1] Odagiri N, Kishi H, Yamashita M. Development of TORAYCA prepreg P2302 carbon fiber reinforced plastic for aircraft primary structural materials. Advanced Composite Materials 1996;5:249–54. https://doi.org/10.1163/156855196X00301.

[2] Fernlund G, Mobuchon C, Zobeiry N. 2.3 Autoclave Processing. Comprehensive Composite Materials II, Elsevier; 2018, p. 42–62. https://doi.org/10.1016/B978-0-12-803581-8.09899-4.

[3] Ersoy N, Tugutlu M. Cure kinetics modeling and cure shrinkage behavior of a thermosetting composite. Polym Eng Sci 2010;50:84–92. https://doi.org/10.1002/pen.21514.

[4] Manohar K, Hogan T, Buttrick J, Banerjee AG, Kutz JN, Brunton SL. Predicting shim gaps in aircraft assembly with machine learning and sparse sensing. J Manuf Syst 2018;48:87–95. https://doi.org/10.1016/J.JMSY.2018.01.011.

[5] Zobeiry N, Poursartip A. The origins of residual stress and its evaluation in composite materials. Structural Integrity and Durability of Advanced Composites: Innovative Modelling Methods and Intelligent Design, Woodhead Publishing; 2015, p. 43–72. https://doi.org/10.1016/B978-0-08-100137-0.00003-1.

[6] Twigg G, Poursartip A, Fernlund G. Tool–part interaction in composites processing. Part II: numerical modelling. Compos Part A Appl Sci Manuf 2004;35:135–41. https://doi.org/10.1016/S1359-835X(03)00132-5.

[7] Twigg G, Poursartip A, Fernlund G. Tool–part interaction in composites processing. Part I: experimental investigation and analytical model. Compos Part A Appl Sci Manuf 2004;35:121–33. https://doi.org/10.1016/S1359-835X(03)00131-3.

[8] Potter KD, Campbell M, Langer C, Wisnom MR. The generation of geometrical deformations due to tool/part interaction in the manufacture of composite components. Compos Part A Appl Sci Manuf 2005;36:301–8. https://doi.org/10.1016/J.COMPOSITESA.2004.06.002.

[9] Stefaniak D, Kappel E, Spröwitz T, Hühne C. Experimental identification of process parameters inducing warpage of autoclave-processed CFRP parts. Compos Part A Appl Sci Manuf 2012;43:1081–91. https://doi.org/10.1016/J.COMPOSITESA.2012.02.013.

[10] Bellini C, Sorrentino L. Analysis of cure induced deformation of CFRP U-shaped laminates. Compos Struct 2018;197:1–9. https://doi.org/10.1016/J.COMPSTRUCT.2018.05.038.

[11] Huang CK, Yang SY. Warping in advanced composite tools with varying angles and radii. Compos Part A Appl Sci Manuf 1997;28:891–3. https://doi.org/10.1016/S1359-835X(97)00045-6.

[12] Roozbehjavan P, Tavakol B, Ahmed A, Koushyar H, Das R, Joven R, et al. Experimental and numerical study of distortion in flat, L-shaped, and U-shaped carbon fiber–epoxy composite parts. J Appl Polym Sci 2014;131:40439. https://doi.org/10.1002/APP.40439.

[13] Albert C, Fernlund G. Spring-in and warpage of angled composite laminates. Compos Sci Technol 2002;62:1895–912. https://doi.org/10.1016/S0266-3538(02)00105-7.

[14] Yuan Z, Wang Y, Peng X, Wang J, Wei S. An analytical model on through-thickness stresses and warpage of composite laminates due to tool–part interaction. Compos B Eng 2016;91:408–13. https://doi.org/10.1016/J.COMPOSITESB.2016.01.016.

[15] Zeng X, Raghavan J. Role of tool-part interaction in process-induced warpage of autoclave-manufactured composite structures. Compos Part A Appl Sci Manuf 2010;41:1174–83. https://doi.org/10.1016/J.COMPOSITESA.2010.04.017.

[16] Chen W, Zhang D. Improved prediction of residual stress induced warpage in thermoset composites using a multiscale thermo-viscoelastic processing model. Compos Part A Appl Sci Manuf 2019;126:105575. https://doi.org/10.1016/J.COMPOSITESA.2019.105575.

[17] Fiorina M, Seman A, Castanie B, Ali KM, Schwob C, Mezeix L. Spring-in prediction for carbon/epoxy aerospace composite structure. Compos Struct 2017;168:739–45. https://doi.org/10.1016/J.COMPSTRUCT.2017.02.074.

[18] Ding A, Wang J, Li S. Understanding process-induced spring-in of L-shaped composite parts using analytical solution. Compos Struct 2020;250:112629. https://doi.org/10.1016/J.COMPSTRUCT.2020.112629.

[19] Wisnom MR, Potter KD, Ersoy N. Shear-lag Analysis of the Effect of Thickness on Spring-in of Curved Composites. J Compos Mater 2006;41:1311–24. https://doi.org/10.1177/0021998306068072.

[20] Ding A, Wang J, Ni A, Li S. A new analytical solution for cure-induced spring-in of L-shaped composite parts. Compos Sci Technol 2019;171:1–12. https://doi.org/10.1016/J.COMPSCITECH.2018.12.004.

[21] Schoenholz C, Zobeiry N. Investigating the impacts of processing variability on tool-part interaction for interply-toughened aerospace composites using a novel shear technique. Compos Part A Appl Sci Manuf 2024;178:107973. https://doi.org/10.1016/J.COMPOSITESA.2023.107973.

[22] Ding A, Fang S, Li X, Sun L, Wang J, Chen H. Experimental and numerical investigation of tool-part interaction on the process-induced distortions in composite structures. Compos Struct 2022;279:114871. https://doi.org/10.1016/J.COMPSTRUCT.2021.114871.

[23] Kaushik V, Raghavan J. Experimental study of tool–part interaction during autoclave processing of thermoset polymer composite structures. Compos Part A Appl Sci Manuf 2010;41:1210–8. https://doi.org/10.1016/J.COMPOSITESA.2010.05.003.

[24] Ersoy N, Potter K, Wisnom MR, Clegg MJ. An experimental method to study the frictional processes during composites manufacturing. Compos Part A Appl Sci Manuf 2005;36:1536–44. https://doi.org/10.1016/J.COMPOSITESA.2005.02.010.

[25] Twigg G, Poursartip A, Fernlund G. An experimental method for quantifying tool–part shear interaction during composites processing. Compos Sci Technol 2003;63:1985–2002. https://doi.org/10.1016/S0266-3538(03)00172-6.

[26] Zobeiry N, Forghani A, Li C, Gordnian K, Thorpe R, Vaziri R, et al. Multiscale characterization and representation of composite materials during processing. Philosophical Transactions of the Royal Society A: Mathematical, Physical and Engineering Sciences 2016;374. https://doi.org/10.1098/RSTA.2015.0278.

[27] Takagaki K, Minakuchi S, Takeda N. Process-induced strain and distortion in curved composites. Part II: Parametric study and application. Compos Part A Appl Sci Manuf 2017;103:219–29. https://doi.org/10.1016/J.COMPOSITESA.2017.09.019.

[28] Takagaki K, Minakuchi S, Takeda N. Process-induced strain and distortion in curved composites. Part I: Development of fiber-optic strain monitoring technique and analytical methods. Compos Part A Appl Sci Manuf 2017;103:236–51. https://doi.org/10.1016/J.COMPOSITESA.2017.09.020.

[29] Fernlund G, Floyd A, Shewfelt M, Hudek M. Process analysis and tool compensation for a complex composite panel. American Society for Composites 22nd Annual Technical Conference, Seattle, WA, 2007.

[30] COMPRO Simulation Software | Convergent n.d. https://www.convergent.ca/products/compro-simulation-software (accessed March 2, 2023).

[31] RAVEN Simulation Software | Convergent n.d. https://www.convergent.ca/products/raven-simulation-software (accessed October 30, 2023).

[32] Zhu Q, Geubelle PH, Li M, Tucker CL. Dimensional accuracy of thermoset composites: Simulation of process-induced residual stresses. J Compos Mater 2001;35:2171–205. https://doi.org/10.1106/NHUB-BXGK-4X8L-777F.

[33] Ding A, Li S, Wang J, Zu L. A three-dimensional thermo-viscoelastic analysis of process-induced residual stress in composite laminates. Compos Struct 2015;129:60–9. https://doi.org/10.1016/J.COMPSTRUCT.2015.03.034.

[34] Zobeiry N. VISCOELASTIC CONSTITUTIVE MODELS FOR EVALUATION OF RESIDUAL STRESSES IN THERMOSET COMPOSITES DURING CURE. Doctor of Philosophy Thesis. University of British Columbia, 1997.

[35] HexPly ® 8552 2020.

[36] 3900 Prepreg System | Toray Composite Materials America, Inc. 2020.

[37] Markatos DN, Tserpes KI, Rau E, Markus S, Ehrhart B, Pantelakis S. The effects of manufacturing-induced and in-service related bonding quality reduction on the mode-I fracture toughness of composite bonded joints for aeronautical use. Compos B Eng 2013;45:556–64. https://doi.org/10.1016/J.COMPOSITESB.2012.05.052.

[38] Critchlow GW, Litchfield RE, Sutherland I, Grandy DB, Wilson S. A review and comparative study of release coatings for optimised abhesion in resin transfer moulding applications. Int J Adhes Adhes 2006;26:577–99. https://doi.org/10.1016/J.IJADHADH.2005.09.003.

[39] Goss B. The effective use of mould release agents. Reinforced Plastics 2004;48:24–6. https://doi.org/10.1016/S0034-3617(04)00402-3.

[40] LOCTITE FREKOTE B-15 - Mold sealer - Henkel Adhesives 2013. https://www.henkel-adhesives.com/us/en/product/mold-release-agents/loctite_frekote_b15.html (accessed September 1, 2022).

[41] LOCTITE FREKOTE 710NC - Release Agent - Henkel Adhesives 2015. https://www.pccomposites.com/product/frekote-710nc/ (accessed September 1, 2022).

[42] Blass D, Dilger K. CFRP-Part Quality as the Result of Release Agent Application – Demoldability, Contamination Level, Bondability. Procedia CIRP, vol. 66, Elsevier; 2017, p. 33–8. https://doi.org/10.1016/J.PROCIR.2017.03.219.

[43] Schoenholz C, Li S, Bainbridge K, Huynh V, Gray A, Chen X, et al. A Machine Learning-Based Portable Inspection Method for Evaluation of Tool Surface Condition and Release Coating in Composites Manufacturing. SAMPE 2022 2022. https://doi.org/10.33599/NASAMPE/S.22.0740.

[44] Schoenholz C, Li S, Bainbridge K, Huynh V, Gray A, Chen X, et al. An Automated Evaluation Method of Tool Surface Condition in Composites Manufacturing Using Machine Learning and Sparse Sensing. SAMPE Journal: Tooling Technology Advancement/Applications 2023;59:10–23.

[45] Schoenholz C, Li S, Bainbridge K, Huynh V, Gray A, Zobeiry N. Accelerated In Situ Inspection of Release Coating and Tool Surface Condition in Composites Manufacturing Using Global Mapping, Sparse Sensing, and Machine Learning. Journal of Manufacturing and Materials Processing 2023, Vol 7, Page 81 2023;7:81. https://doi.org/10.3390/JMMP7030081.

[46] Bainbridge K, Schoenholz C, Zobeiry N. Investigating the aging of release coating in aerospace composites manufacturing. University of Washington Undergraduate Research in MSE 2021;2:7–11. https://doi.org/10.6069/ssywg443.

[47] Máša V, Horňák D, Petrilák D. Industrial use of dry ice blasting in surface cleaning. J Clean Prod 2021;329:129630. https://doi.org/10.1016/J.JCLEPRO.2021.129630.

[48] LOCTITE FREKOTE PMC - solvent-based post mould cleaner - Henkel Adhesives n.d. https://www.henkel-adhesives.com/us/en/product/mold-release-cleaners/loctite_frekote_pmc.html (accessed December 28, 2022).

[49] Schoenholz C, Zobeiry N. INVESTIGATING THE EFFECTS OF RELEASE COATING ON TOOL-PART INTERACTION AND PROCESS-INDUCED DEFORMATIONS IN COMPOSITES MANUFACTURING. International SAMPE Technical Conference, vol. 2023- April, Soc. for the Advancement of Material and Process Engineering; 2023. https://doi.org/10.33599/NASAMPE/S.23.0007.

[50] ISO - ISO 1302:2002 - Geometrical Product Specifications (GPS) — Indication of surface texture in technical product documentation 2002. https://www.iso.org/standard/28089.html (accessed September 28, 2022).

[51] Aero2 PCS 60 - Precision & Versatile Dry Ice Blasting Machine - Cold Jet n.d. https://www.coldjet.com/our-equipment/dry-ice-blasting-equipment/aero2-series/aero2-pcs-60/ (accessed October 6, 2022).

[52] Owens DK, Wendt RC. Estimation of the surface free energy of polymers. J Appl Polym Sci 1969;13:1741–7. https://doi.org/10.1002/APP.1969.070130815.

[53] de Gennes P-G, Brochard-Wyart F, Quéré D. Capillarity and Wetting Phenomena. Springer New York; 2004. https://doi.org/10.1007/978-0-387-21656-0.

[54] Parker BM, Waghorne RM. Surface pretreatment of carbon fibre-reinforced composites for adhesive bonding. Composites 1982;13:280–8. https://doi.org/10.1016/0010-4361(82)90011-8.

[55] Jeenjitkaew C, Luklinska Z, Guild F. Morphology and surface chemistry of kissing bonds in adhesive joints produced by surface contamination. Int J Adhes Adhes 2010;30:643–53. https://doi.org/10.1016/J.IJADHADH.2010.06.005.

[56] Persson BNJ. On the theory of rubber friction. Surf Sci 1998;401:445–54. https://doi.org/10.1016/S0039-6028(98)00051-X.

[57] OriginLab Corporation. OriginPro 2024 n.d.

[58] Tracey A, Flinn B. Infrared Spectroscopy: A Potential in Process Quality Assurance Method for Composite Bonding Surface Preparation. 44th ISTC - Charleston SC - Oct 22-25 / 2012, 2012.

[59] Wenzel RN. Surface roughness and contact angle. Journal of Physical & Colloid Chemistry 1949;53:1466–7. https://doi.org/10.1021/J150474A015/ASSET/J150474A015.FP.PNG_V03.

[60] Thorpe RJ. Experimental characterization of the viscoelastic behavior of a curing epoxy matrix composite from pre-gelation to full cure. Master of Applied Science. University of British Columbia, 2013. https://doi.org/10.14288/1.0073820.

[61] Precision Brand. Steel Feeler Gage 1/2" x 12" Blades n.d. https://www.precisionbrand.com/product-category/1-2-x-12-blades-steel-feeler-gage/ (accessed December 28, 2022).

[62] Department of Defense Handbook, Composite Materials Handbook, Volume 1. Polymer Matrix Composites Guidelines for Characterization of Structural Materials. vol. 1. 2002.

[63] Dykeman D. Minimizing uncertainty in cure modeling for composites manufacturing. Doctor of Philosophy. University of British Columbia, 2008. https://doi.org/10.14288/1.0066334.

[64] Zobeiry N, Vaziri R, Poursartip A. Computationally efficient pseudo-viscoelastic models for evaluation of residual stresses in thermoset polymer composites during cure. Compos Part A Appl Sci Manuf 2010;41:247–56. https://doi.org/10.1016/J.COMPOSITESA.2009.10.009.

[65] Li C, Zobeiry N, Keil K, Chatterjee S, Poursartip A. Advances in the Characterization of Residual Stress in Composite Structures. SAMPE 2014 - SEATTLE, 2014.

[66] Johnston AA. AN INTEGRATED MODEL OF THE DEVELOPMENT OF PROCESS-INDUCED DEFORMATION IN AUTOCLAVE PROCESSING OF COMPOSITE STRUCTURES. Doctor of Philosophy. University of British Columbia, 1997.

[67] Kassapoglou C. 8. Design and Analysis of Composite Beams. Design and Analysis of Composite Structures: With Applications to Aerospace Structures. Second Edition, West Sussex, United Kingdom: John Wiley & Sons, Ltd.; 2013, p. 189–236. https://doi.org/https://doi.org/10.1002/9781118536933.ch8.

[68] Kishi H, Ozaki A, Odagiri N. Prepreg and Composite. 5413847, 1995.

[69] Odagiri N, Suzue S, Kishi H, Nakae T, Matsusaki A. Fiber Reinforced Composite Materials Having Resin Practice Inter-layer Zones. 5028478, 1991.

[70] T800S Technical Data Sheet | Toray Composite Materials America, Inc. 2018.

[71] Chen C, Poursartip A, Fernlund G. Influence of the glass transition of interlaminar particles on shear behaviour during cure of interlayer toughened thermoset composites. Compos Part A Appl Sci Manuf 2021;147:106447. https://doi.org/10.1016/J.COMPOSITESA.2021.106447.

[72] Kim BS, Chiba T, Inoue T. Phase separation and apparent phase dissolution during cure process of thermoset/thermoplastic blend. Polymer (Guildf) 1995;36:67–71.

[73] Kishi H, Odagiri N. 14. Toughened thermoset resin matrix composites. Series in Materials Science and Engineering: Aerospace Materials, 2001, p. 187–98. https://doi.org/10.1201/9781420034721.CH14.

[74] Rasband WS. ImageJ. US National Institutes of Health, Bethesda, Maryland, USA 1997. https://imagej.nih.gov/ij/ (accessed September 8, 2022).

[75] Garstka T, Ersoy N, Potter KD, Wisnom MR. In situ measurements of through-the-thickness strains during processing of AS4/8552 composite. Compos Part A Appl Sci Manuf 2007;38:2517–26. https://doi.org/10.1016/J.COMPOSITESA.2007.07.018.

[76] Gottschalk PG, Dunn JR. The five-parameter logistic: A characterization and comparison with the four-parameter logistic. Anal Biochem 2005;343:54–65. https://doi.org/10.1016/J.AB.2005.04.035.

[77] Joven R, Tavakol B, Rodriguez A, Guzman M, Minaie B. Characterization of shear stress at the tool-part interface during autoclave processing of prepreg composites. J Appl Polym Sci 2013;129:2017–28. https://doi.org/10.1002/APP.38909.

[78] Schoenholz C, Moomaw J, Zobeiry N. Investigating the Effects of Cure Pressure on Tool-Part Interaction and Process-Induced Deformations in Composites. PROCEEDINGS OF THE AMERICAN SOCIETY FOR COMPOSITES-THIRTY-SEVENTH TECHNICAL CONFERENCE, vol. 0, DEStech Publications Inc.; 2022. https://doi.org/10.12783/ASC37/36383.

[79] Schoenholz C, Slade D, Zappino E, Petrolo M, Zobeiry N. Representation, characterization and simulation of tool-part interaction and its effects on process-induced deformations in composites. 36th Technical Conference of the American Society for Composites 2021: Composites Ingenuity Taking on Challenges in Environment-Energy-Economy, ASC 2021, vol. 2, 2021.

[80] Martin CJ, Seferis JC, Wilhelm MA. Frictional resistance of thermoset prepregs and its influence on honeycomb composite processing. Compos Part A Appl Sci Manuf 1996;27:943–51. https://doi.org/10.1016/1359-835X(96)00037-1.

[81] Flanagan R. The dimensional stability of composite laminates and structures. Queen's University of Belfast, 1997.

[82] FlexiForce HT201 Sensor | Tekscan n.d. https://www.tekscan.com/products-solutions/force-sensors/ht201 (accessed December 28, 2022).

[83] Persson BNJ. Theory of rubber friction and contact mechanics. Journal of Chemical Physics 2001;115:3840–61. https://doi.org/10.1063/1.1388626.

[84] Otsuki M, Matsukawa H. Systematic Breakdown of Amontons' Law of Friction for an Elastic Object Locally Obeying Amontons' Law. Scientific Reports 2013 3:1 2013;3:1–6. https://doi.org/10.1038/srep01586.

[85] Rasmussen CE, Williams CKI. Gaussian Processes for Machine Learning. The MIT Press; 2006.

[86] Wang J. An Intuitive Tutorial to Gaussian Processes Regression. Kingston, Ontario: 2022.

[87] Schulz E, Speekenbrink M, Krause A. A tutorial on Gaussian process regression: Modelling, exploring, and exploiting functions. J Math Psychol 2018;85:1–16. https://doi.org/10.1016/J.JMP.2018.03.001.

[88] Schulz E, Speekenbrink M, Krause A. A tutorial on Gaussian process regression: Modelling, exploring, and exploiting functions. J Math Psychol 2018;85:1–16. https://doi.org/10.1016/J.JMP.2018.03.001.

[89] Freed Y, Salviato M, Zobeiry N. Implementation of a probabilistic machine learning strategy for failure predictions of adhesively bonded joints using cohesive zone modeling. Int J Adhes Adhes 2022;118:103226. https://doi.org/10.1016/J.IJADHADH.2022.103226.

[90] Wynn M, Zobeiry N. Investigating the Effect of Temperature History on Crystal Morphology of Thermoplastic Composites Using In Situ Polarized Light Microscopy and Probabilistic Machine Learning. Polymers (Basel) 2022;15:18. https://doi.org/10.3390/POLYM15010018.

[91] Schoenholz C, Zobeiry N. An Accelerated Process Optimization Method to Minimize Deformations in Composites Using Theory-guided Probabilistic Machine Learning. Compos Part A Appl Sci Manuf 2024;176:107842. https://doi.org/10.1016/J.COMPOSITESA.2023.107842.

[92] Van Rossum G, Drake Jr F. Python. Version 3.10. 2021.

[93] Pedregosa F, Varoquaux G, Gramfort A, Michel V, Thirion B, Grisel O, et al. Scikit-learn: Machine Learning in Python. Journal of Machine Learning Research 2011;12:2825–30.

[94] Daniel IM, Ishai Ori. Engineering mechanics of composite materials. Oxford University Press; 2006.

[95] Agarwal B, Broutman L, Chandrashenkhara K. Analysis and Performance of Fiber Composites. Third. Hoboken, New Jersey: John Wiley & Sons, Inc.; 2006.

[96] Chen C, Poursartip A, Fernlund G. Cure-dependent microstructures and their effect on elastic properties of interlayer toughened thermoset composites. Compos Sci Technol 2020;197:108241. https://doi.org/10.1016/J.COMPSCITECH.2020.108241.

[97] Bogetti TA, Gillespie JW. Process-Induced Stress and Deformation in Thick-Section Thermoset Composite Laminates. J Compos Mater 1992;26.

[98] Zappino E, Schoenholz C, Masia R, Zobeiry N, Petrolo M. OPTIMAL LAY-UPS TO MINIMIZE PROCESS-INDUCED DEFORMATIONS IN L-SHAPED CFRP PARTS VIA LAYER-WISE MODELS. International SAMPE Technical Conference, vol. 2023- April, Soc. for the Advancement of Material and Process Engineering; 2023. https://doi.org/10.33599/NASAMPE/S.23.0143.

[99] Zappino E, Zobeiry N, Petrolo M. An efficient numerical approach to evaluate process-induced free-edge stresses in laminated composites. PROCEEDINGS OF THE

AMERICAN SOCIETY FOR COMPOSITES-THIRTY-SEVENTH TECHNICAL CONFERENCE, ASC; 2022.

[100] Zobeiry N, Poursartip A. Theory-Guided Machine Learning for Process Simulation of Advanced Composites 2021.

[101] Arafath ARA, Vaziri R, Poursartip A. Closed-form solution for process-induced stresses and deformation of a composite part cured on a solid tool: Part I – Flat geometries. Compos Part A Appl Sci Manuf 2008;39:1106–17. https://doi.org/10.1016/J.COMPOSITESA.2008.04.009.

[102] Li D, Li X, Dai J. Process modelling of curing process-induced internal stress and deformation of composite laminate structure with elastic and viscoelastic models. Applied Composite Materials 2017;25:527–44. https://doi.org/10.1007/S10443-017-9633-5/FIGURES/14.

[103] Johnston AA, Vaziri R, Profile S, Poursartip A. A Plane Strain Model for Process-Induced Deformation of Laminated Composite Structures. J Compos Mater 2001;35:1435–69. https://doi.org/10.1106/YXEA-5MH9-76J5-BACK.

[104] Zappino E, Zobeiry N, Petrolo M, Vaziri R, Carrera E, Poursartip A. Analysis of process-induced deformations and residual stresses in curved composite parts considering transverse shear stress and thickness stretching. Compos Struct 2020;241:112057. https://doi.org/10.1016/J.COMPSTRUCT.2020.112057.

[105] Carrera E, Cinefra M, Zappino E, Petrolo M. Finite Element Analysis of Structures through Unified Formulation. vol. 9781119941217. Wiley Blackwell; 2014. https://doi.org/10.1002/9781118536643.

[106] Chen C, Poursartip A, Fernlund G. A novel method to measure laminate shear modulus development of interlayer toughened composite laminates during the curing process. Proceedings of the American Society for Composites - 34th Technical Conference, ASC 2019 2019. https://doi.org/10.12783/ASC34/31316.

[107] Zobeiry N, Reiner J, Vaziri R. Theory-guided machine learning for damage characterization of composites. Compos Struct 2020;246:112407. https://doi.org/10.1016/J.COMPSTRUCT.2020.112407.

[108] Wagner N, Rondinelli JM. Theory-guided machine learning in materials science. Front Mater 2016;3:203425. https://doi.org/10.3389/FMATS.2016.00028/BIBTEX.

[109] Zobeiry N, Profile S, Poursartip A. Theory-Guided Machine Learning Composites Processing Modelling for Manufacturability Assessment in Preliminary Design, Quebec City, Canada: NAFEMS 17th World Congress; 2019.

[110] Zobeiry N, Petrolo M, Zappino E, Schoenholz C, Masia R. An Optimization Strategy Based on Machine Learning and Layer-Wise Models to Minimize Process-Induced Deformations in CFRP Parts. Proceedings of ASME 2023 Aerospace Structures, Structural Dynamics, and

Materials Conference, SSDM 2023, American Society of Mechanical Engineers Digital Collection; 2023. https://doi.org/10.1115/SSDM2023-106945.

[111] Kassapoglou C. 3. Review of Classical Laminated Plate Theory. Design and Analysis of Composite Structures: With Applications to Aerospace Structures. Second Edition, West Sussex, United Kingdom: John Wiley & Sons, Ltd.; 2013, p. 33–53. https://doi.org/https://doi.org/10.1002/9781118536933.ch3.

[112] Schwarz G. Estimating the Dimension of a Model. The Annals of Statistics 1978;6:461–4.

[113] Claeskens G, Hjort NL. Model selection and model averaging. Cambridge University Press; 2008. https://doi.org/10.1017/CBO9780511790485.

[114] Karpatne A, Atluri G, Faghmous JH, Steinbach M, Banerjee A, Ganguly A, et al. Theory-guided data science: A new paradigm for scientific discovery from data. IEEE Trans Knowl Data Eng 2017;29:2318–31. https://doi.org/10.1109/TKDE.2017.2720168.

[115] Liao Z, Qiu C, Yang J, Yang J, Yang L. Accelerating the Layup Sequences Design of Composite Laminates via Theory-Guided Machine Learning Models. Polymers 2022, Vol 14, Page 3229 2022;14:3229. https://doi.org/10.3390/POLYM14153229.

[116] Schoenholz C, Zobeiry N. A Theory-Guided Probabilistic Machine Learning Method to Minimize Process-Induced Deformations in Composite Structures. ASME 2023 Aerospace Structures, Structural Dynamics, and Materials Conference, American Society of Mechanical Engineers Digital Collection; 2023. https://doi.org/10.1115/SSDM2023-106753.

[117] Tipping ME. Bayesian Inference: An Introduction to Principles and Practice in Machine Learning. In: Bousquet O, von Luxburg U, Rätsch G, editors. Lecture Notes in Artificial Intelligence Subseries of Lecture Notes in Computer Science, 2003, p. 41–62.

[118] Lindfield G, Penny J. Linear Equations and Eigensystems. Numerical Methods 2019:73–156. https://doi.org/10.1016/B978-0-12-812256-3.00011-7.

[119] White SR, Hahn HT. Cure Cycle Optimization for the Reduction of Processing-Induced Residual Stresses in Composite Materials. J Compos Mater 1993;27:1352–78. https://doi.org/10.1177/002199839302701402.

[120] Wang B, Fan S, Chen J, Yang W, Liu W, Li Y. A review on prediction and control of curing process-induced deformation of continuous fiber-reinforced thermosetting composite structures. Compos Part A Appl Sci Manuf 2023;165:107321. https://doi.org/10.1016/J.COMPOSITESA.2022.107321.

VITA

Caleb S. Schoenholz was born in Green Bay, Wisconsin, on November 19, 1997. He completed his high school education at Green Bay Preble High School, graduating in June 2016. He then attended Winona State University and attained a Bachelor of Science (B.S.) degree in Composite Materials Engineering with a minor in Mathematics in May 2020. Later that year, he joined the University of Washington Composites Group, led by Dr. Navid Zobeiry. He then obtained a Master of Science (M.S.) degree in June 2022, followed by a Doctor of Philosophy (Ph.D.) degree in Materials Science & Engineering in June 2024.